國立交通大學

材料科學與工程研究所

博士論文

沉積在金屬氧化物載體上之鉑金屬奈米粒對甲醇氧化反應之電催化特性研究

Electrocatalytic activity of Pt nanoparticles supported on metal oxides toward methanol oxidation

研 究 生：陳重守

指導教授：潘扶民 教授

中 華 民 國 一 百 年 七 月

沉積在金屬氧化物載體上之鉑金屬奈米粒對甲醇氧化反應之電催化特性研究

Electrocatalytic activity of Pt nanoparticles supported on metal oxides toward methanol oxidation

研 究 生:陳重守　　　　　　　　　　　　　Student: Chung-Shou Chen

指導教授:潘扶民 教授　　　　　　　　　　　Advisor: Fu-Ming Pan

國立交通大學

材料科學與工程研究所

博士論文

A Thesis
Submitted to Department of Materials Science and Engineering
College of Engineering
National Chiao Tung University
In partial Fulfillment of the Requirements
for the Degree of Doctor of Philosophy
In Materials Science and Engineering

July 2011
Hsinchu, Taiwan, Republic of China

中 華 民 國 一 百 年 七 月

沉積在金屬氧化物載體上之鉑金屬奈米粒對甲醇氧化反應之電催化特性研究

研究生:陳重守　　　　　　　　　　　　　　　　　指導教授:潘扶民 教授

國立交通大學

材料科學與工程學系博士班

摘要

　　本研究製備多孔性二氧化鈦、氧化鈀奈米薄片及類卡斯特形貌之氧化鎳薄膜做為鉑金屬奈米粒之載體,並探討鉑奈米粒對甲醇氧化反應之電催化特性,此三種氧化物薄膜具有高表面積可提供較多的表面沉積鉑奈米粒子,進而使鉑催化劑有較高的電化學活性表面積(ESA),循環伏安及一氧化碳脫附實驗指出此三種氧化物載體有效提升鉑奈米粒對甲醇氧化反應之催化活性及抗一氧化碳毒化的能力。

　　我們利用水熱法製備多孔性二氧化鈦作為鉑金屬奈米粒載體探討甲醇氧化反應之電催化研究,5-7 奈米大小的鉑金屬粒以脈衝電鍍法均勻地電鍍在經由 600°C 真空退火之多孔性二氧化鈦載體,鉑/二氧化鈦電極在循環伏安及一氧化碳脫附實驗中展現對甲醇氧化優異的電催化特性及抗一氧化碳毒化能力,我們歸因此優異的電催化活性為鉑奈米粒與氧化物之間的協同效應所造成,鉑金屬與二氧化鈦載體間電荷交互作用將改變鉑表面的一氧化碳吸附性質,並經由雙官能基機制進而加速吸附在鉑表面的一氧化碳之氧化,並增加鉑催化甲醇氧化的能力。

　　氧化鈀奈米薄片經由反應性濺鍍沉積在碳布上,接著以脈衝電鍍法沉積鉑奈米粒製備鉑/氧化鈀電極,我們發現在酸性環境中之循環伏安量測,氧化鈀奈米薄片之電化學行為與金屬鈀相似,這是氧化鈀表面在循環伏安量測過程中還原成金屬鈀薄膜之故,因此金屬鈀/氧化鈀的氧化還原行為將影響氧化鈀在循環伏安量測中對甲醇氧化的電

催化特性，我們提出一組化學反應機制流程圖用以解釋氧化鈀在酸性溶液中對甲醇氧化反應之現象。此外因為鈀金屬容易溶解於酸性電解液中，因此氧化鈀之奈米薄片形貌在酸性溶液中將會嚴重崩解，但我們發現，將鉑奈米粒沉積於氧化鈀表面將有效減緩氧化鈀之奈米薄片形貌崩解於酸性電解液中。

粗糙表面的鎳薄膜擁有類卡斯特之形貌，可提供高表面積經由脈衝電鍍法讓鉑奈米粒沉積，在鹼性環境下，鉑/鎳電極在循環伏安中在展現優異的甲醇氧化反應及抗一氧化碳毒化特性，循環伏安過程中氧化鎳載體可在表面形成氫氧化鎳，這將有助於鉑金屬經由雙官能基機制提升抗一氧化碳的能力，Langmuir-Hishelwood 及 Eley-Rideal 機制分別用來解釋氫氧基吸附於氧化鎳載體及氫氧離子在鹼性溶液中如何增加鉑金屬抗毒化能力，XPS 分析指出鉑奈米粒與鎳載體間的電荷轉移，此電荷交互作用將改變鉑表面的一氧化碳吸附性質，有助於一氧化碳被氫氧基氧化之反應，此氫氧基由鎳載體或鹼性電解液中獲得並吸附在鉑奈米粒周圍。

鉑/二氧化鈦，鉑/氧化鈀，鉑/鎳此三種電極有優異的甲醇氧化之電催化特性，我們將此優異之電催化效率歸因於優異的一氧化碳容忍度及高電化學活性表面積，發生在鉑奈米粒與三種金屬氧化物之間的電荷交互作用與雙官能基機制發揮了協同效應，顯著提升鉑奈米粒抗一氧化碳毒化能力，進而增進對甲醇氧化反應之電催化活性。

關鍵詞：直接甲醇燃料電池；甲醇氧化反應；抗一氧化碳毒化；鉑奈米粒；雙官能基機制；電荷效應；孔洞性二氧化鈦；氧化鈀；鎳

Electrocatalytic activity of Pt nanoparticles supported on metal oxides reactions toward methanol oxidation

Student: Chung-Shou Chen   **Adviser: Fu-Ming Pan**

Departement of Materials Science and Engineering

National Chiao Tung University

Abstract

Pt nanoparticles were prepared on nanostructured metal oxides as the electrocatalyst for methanol oxidation reaction (MOR) in this study. Pt nanoparticles were pulse-electrodeposited on the metal oxides, which included nanoporous TiO_2 thin film, PdO nanoflake thin film and karst-like NiO thin film. Because of the large loading area on these support and the well-dispersed Pt nanoparticles, these Pt-metal oxide electrodes had a large electrochemical active surface area (ESA). Cyclic voltammetry (CV) and CO stripping measurements showed that the Pt/TiO_2, Pt/PdO and Pt/karst-Ni electrode had a high electrocatalytic activity toward methanol oxidation and an excellent CO tolerance compared with the blanket Pt electrode.

Porous TiO_2 thin films were prepared on the Si substrate by hydrothermal method, and used as the Pt electrocatalyst support for methanol oxidation study. Well-dispersed Pt nanoparticles with a size of 5-7 nm were pulse-electrodepotied on the porous TiO_2 support, which was mainly composed of the anatase phase after an annealing at $600^{\circ}C$ in vacuum. Cyclic voltammetry (CV) and CO stripping measurements showed that the Pt/TiO_2 electrode had a high electrocatalytic activity toward methanol oxidation and an excellent CO tolerance. The excellent electrocatalytic performance of the electrode is ascribed to the synergistic effect of Pt nanoparticles and the porous TiO_2 support on CO oxidation.

The strong electronic interaction between Pt and the TiO_2 support may modify CO chemisorption properties on Pt nanoparticles, thereby facilitating CO oxidation on Pt nanoparticles via the bi-functional mechanism and thus improving the electrocatalytic activity of the Pt catalyst toward methanol oxidation.

PdO nanoflake thin films on carbon cloths were prepared by reactive sputtering deposition, and pulse-electrodeposited Pt nanoparticles on the PdO thin films. In acidic electrolytes, the PdO nanoflake thin film has a cyclic voltamperometric (CV) behavior similar to a metallic Pd electrode because of the formation of a metallic Pd surface layer on the PdO thin film under the CV experimental condition. The methanol oxidation reaction (MOR) on the PdO thin film exhibits a CV feature that is closely related to the Pd/PdO redox reaction. We proposed a reaction mechanism scheme for the MOR on the PdO electrode in the acidic solution. The nanoflake morphology on the PdO electrode is seriously damaged during the CV test because of anodic dissolution of metal Pd in acid media. However, the nanoflake damage is greatly alleviated when Pt nanoparticles are electrodeposited on the PdO nanoflake thin film. Negative charges transfer from the PdO support to the Pt nanoparticles according to XPS analysis.

The rugged Ni thin films has a karst-like morphology, which provides a large surface area for electrodeposited Pt nanoparticles. Cyclic voltammetry measurements showed that the Pt/karst-Ni electrode had a high electrocatalytic activity toward MOR and CO tolerance in the KOH electrolyte. $Ni(OH)_2$ formed on the Ni support during the potential scan can enhance CO tolerance of Pt nanoparticles via the bi-functional mechanism. The Langmuir-Hishelwood and the Eley-Rideal mechanisms are used to elucidate the role of OH surface groups on the Ni support and OH^- ions in the electrolyte, respectively, in the enhancement of the CO tolerance. XPS analysis indicates that negative charges transfer from the Ni support to Pt nanoparticles. The electronic interaction may modify adsorption properties of CO adspecies on the Pt catalyst; the modification allows easy CO

electro-oxidation by OH species surrounding the Pt nanoparticles, either from the Ni support or from the alkaline solution.

The Pt/TiO$_2$, Pt/PdO and Pt/karst-Ni electrodes have a high electrocatalytic activity toward MOR, and the good electrocatalytic performance of the three electrodes are ascribed to the high CO tolerance and the large ESA. The synergistic effect of the bi-functional mechanism and the electronic interaction makes the Pt/TiO$_2$, Pt/PdO and Pt/karst-Ni electrodes a good catalytic electrode for MOR.

Keywords：DMFCs；Methanol oxidation reaction；CO tolerance；Pt nanoparticles；Bi-functional mechanism；Electronic effect；Porous TiO$_2$；PdO；Ni

Acknowledgement

Contents

Table Caption

Figure Caption

Chapter 1   Introduction

1.1 Introduction to fuel cells

Because of the expected shortage of fossil fuels and the urgent need of environment friendly energies, such as renewable energy resources, fuel cells receive extensive attention in recent decades.   The working principle behind fuel cells strongly relies on chemical interactions between the fuels and the electrodes, and shares some common characteristics with primary batteries.   Fuel cells are powerful energy sources combining numerous advantages of both conventional electricity generation engines and batteries, such as a long operation lifetime for the former and being clean and portable for the latter.   Therefore, they are thought to be promising renewable energy resources to reduce the demand of traditional petrochemical energies, which will be eventually exhausted and are a major cause resulting in environmental pollution and the greenhouse effect.

In a simple fuel cell, the fuel electrochemical reaction is split into two half reactions:

$$H_2 \rightleftharpoons 2H^+ + 2e^- \tag{1-1}$$

$$\frac{1}{2}O_2 + 2H^+ + 2e^- \rightleftharpoons H_2O \tag{1-2}$$

The electrons transferred from the fuel are forced to flow through an external circuit by spatially separating these reactions, thus constituting an electric current.   Spatial separation is performed by utilizing an electrolyte, which is a medium that allows ions to flow but not electrons.   A full fuel cell must have two electrodes separated by an electrolyte.   The two electrochemical half reactions tale place in the two electrodes, respectively.   In 1839, the first fuel cell, invented by William Grove, probably looked like an extremely simple H_2-O_2 fuel cell, as shown in fig. 1-1 [2].   This fuel cell consisted of two electrodes dipped into an aqueous acid electrolyte, such as H_2SO_4 or $HClO_4$.   At the anode electrode, bubbling hydrogen gas is split into H^+ and electrons following Equation
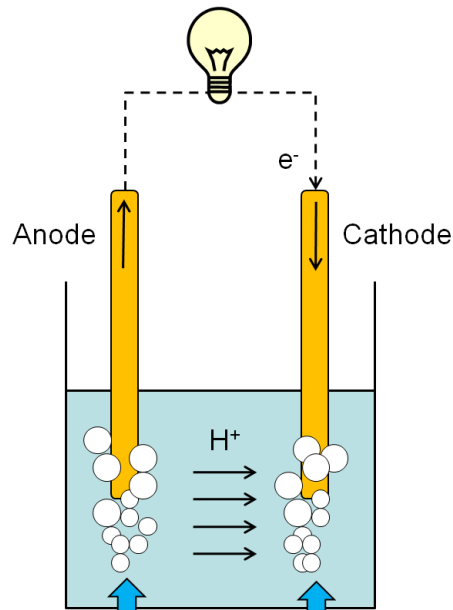
Figure 1-1 A simple H_2-O_2 fuel cell.

(1-1). The electrons flow from anode to cathode through external circulation that connects the two electrodes. Furthermore, the H^+ can flow through the electrolyte, but the electrons cannot. When the electrons reach the cathode electrode, they recombine with H^+ and bubbling oxygen gas to produce water following Equation (1-2). The flowing electrons will provide power to the load, such as a light bulb, and the simple fuel cell will produce electricity.

Fuel cells are classified into five major types which are based on the kinds of the electrolyte: Phosphoric acid fuel cells (PAFC); Polymer electrolyte membrane fuel cell (PEMFC); Alkaline fuel cell (AFC); Molten carbonate fuel cell (MCFC); Solid oxide fuel cell (SOFC). They all operate at different temperature regimens, incorporate different materials, and often differ in their fuel tolerance and performance characteristics, as shown in table 1-1 [2]. PEMFCs utilize a thin polymer membrane where protons can be saturated as the electrolyte and platinum-based materials are the prevailing catalysts for cathode and anode. Pure hydrogen and oxygen are used as the fuel in anode and cathode electrode, respectively. However, liquid fuels such as methanol, ethanol or formic acid are also considered because difficulties in the aspeck of storage and transportation is the extreme

weakness of hydrogen. In addition, direct methanol fuel cells (DMFCs) use methanol of high energy density as the fuel, and methanol has been extensively considered as renewable power source and is an attractive candidate for low-power portable fuel cell applications. The advantages of DMFCs comparing with several kinds of fuel cells are the operation at low temperatures, easy fuel storage, and the reduced volume and weight in equipment. Even if there are many advantages, DMFCs used Pt as the catalysts in the practical commercialization is also impeded by many difficulties such as methanol crossover, the high cost of the Pt catalyst, the inaction of the oxygen reduction reaction and the low efficiency of the electroactivity of MOR due to CO poison.

Table 1-1 Description of major fuel cell types [2]

	PEMFC	PAFC	AFC	MCFC	SOFC
Electrolyte	Polymer membrane	Liquid H_3PO_4 (immobilized)	Liquid KOH (immobilized)	Molten carbonate	Ceramic
Charge carrier	H^+	H^+	OH^-	CO_3^{2-}	O^{2-}
Operating temperature	80 ^{o}C	200 ^{o}C	60-220 ^{o}C	650 ^{o}C	600-1000 ^{o}C
Catalyst	Platinum	Platinum	Platinum	Nickel	Perovskites (ceramic)
Cell components	Carbon based	Carbon based	Carbon based	Stainless based	Ceramic based
Fuel compatibility	H_2, methanol	H_2	H_2	H_2, CH_4	H_2, CH_4, CO

1.2 Motivation

As far as MOR is concerned, the most widely studied subject is how to enhance the electrocatalytic activity of anode with a minimized Pt loading. Researchers try to reduce the size and optimize the distribution of Pt nanoparticles to minimize the use of the preious Pt catalyst and increase concurrently the electroactivity surface area (ESA) for methanol oxidation on the catalyst. Another major approach to improving the MOR electroactivity

3

is to increase the resistance of Pt catalysts against CO poisoning, which results from catalytic site blocking by carbonaceous byproducts due to incomplete methanol oxidation. On the other hand, to improve the CO tolerance, Pt-based binary or ternary alloys commonly used as catalyst in considerable studies, in particular Pt-Ru, are to enhance CO electro-oxidation via the bi-functional mechanism, which governs the electro-oxidation reaction of the carbonaceous byproducts with neighboring OH adspecies, and/or the so-called electronic effect [3-10]. A fast removal rate of the carbonaceous adspecies can continuously create free adsorption sites for methanol molecules, thus resulting in a high reaction rate of methanol electro-oxidation. The removal rate speedily of the carbonaceous adspecies can be continuously created the free adsorption sites for methanol molecule which results in the high reaction rate of methanol electro-oxidation. More transition metals and metal oxides as a promoter or the catalyst support are, more the CO tolerance of the Pt catalyst can be gained effectively which is based on a similar principle [3-22].

Figure 1-2 schematically illustrates the likely reaction steps of CO oxidation on the Pt nanoparticles via the bi-functional mechanism. Dissociative adsorption of water
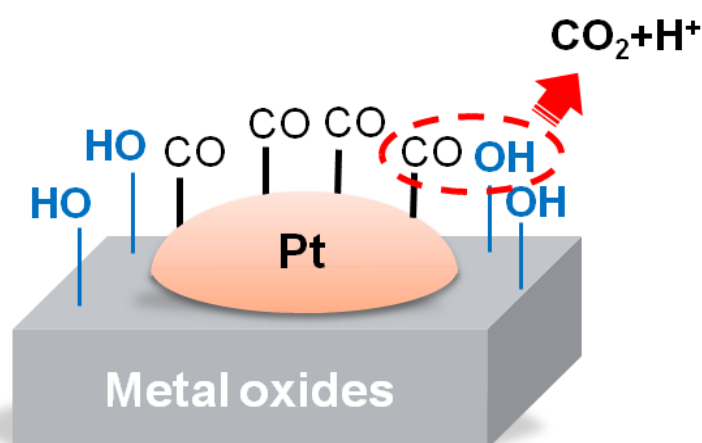
Figure 1-2 Schematic diagram illustrating the bi-functional mechanism of the Pt nanoparticle and the metal oxide support on CO oxidation.

4

molecules on the metal oxide support creates OH surface groups. The groups adjacent to Pt nanoparticles may readily oxidize CO groups bonded on the Pt surface. In the thesis, we used TiO_2, PdO and NiO nanostructured thin films as the support of Pt nanoparticles and studied the effect of the oxide supports on the enhancement of the electrocatalytic activity of the Pt catalyst toward MOR [20, 23]. We ascribed the observed electroactivity enhancement to the synergism of the electronic effect and the bi-functional mechanism, which was a result in electronic and chemical interactions between the hydrous oxides and the Pt nanoparticles.

Chapter 2   Literature Review

2.1 Direct methanol fuel cells (DMFCs)

Direct methanol fuel cells (DMFCs) are very attractive for the mobile power source application, such as automotive systems and portable electronics, in the past decade because they can be operated at low temperatures and have a high energy density and a long span-life.   They are lightweight with a simple system design based on PEMFC technology, utilizing hydrogen as fuel.   Nevertheless, while the DMFCs work, methanol is directly fed as fuel into the fuel cell systems without converting to hydrogen.   It mainly resolves the difficulty and the danger in the aspect of storing and transporting of hydrogen.   Besides, methanol can be produced easily in natural from solid (coal), liquid (crude oil) or gas (natural gas) and has a high energy density.

Although DMFCs possess many merits as a power source, practical commercialization still faces several fundamental materials challenges, such as degraded electroactivity of MOR due to CO poisoning, sluggish oxygen reduction reaction, methanol crossover and the high cost of the Pt catalyst.   As far as the methanol oxidation reaction (MOR) is concerned, major challenges receiving particular attention are a higher electrocatalytic activity with a minimized Pt catalyst loading and a better resistance against the CO poisoning effect.   The widely adopted method to improve the electrocatalytic mass activity of the precious Pt catalyst toward MOR is to reduced the size and optimize the distribution of Pt nanoparticles to minimize the use of the precious Pt catalyst and concurrently increase the electroactivity surface area (ESA) [11, 12, 24-28].

A schematic diagram of a DMFC is presented in Fig. 2.1.   At the anode, methanol and water react to produce carbon dioxide, protons and electrons by the catalyst layer in equation (1).   Platinum (Pt) or platinum alloy are usually utilized as catalytic material in
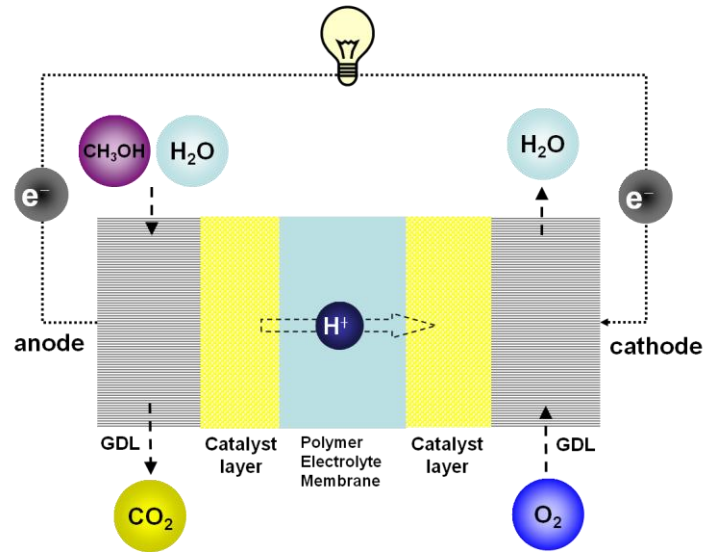
Figure 2-1 Schematic illustration of DMFCs is shown. The MOR and ORR occur at the anode and cathode, respectively. Electricity is made and utilized in the external circuit.

anode electrode. The protons produced at the anode will be through the polymer electrolyte membrane to the cathode and react with oxygen. Nafion$^{®}$ membranes by DuPont are the most investigated and employed as the polymer electrolyte membrane for PEMFCs or DMFCs. These membranes consist of a poly-tetrafluoroethylene (PTFE) based structure and have a high protons conductivity. At the cathode, Pt is also utilized as the catalyst; oxygen reacts on the electrodes with protons, which come from the anode, and form water as shown in equation (2). The oxygen reduction reaction (ORR) proceeds via certain steps in which molecular oxygen dissociates at the catalyst surface and recombines with protons (hydrogen ions) to form water [29]. The electrons, which is produced at the anode and receive at the cathode carry the free energy change of the oxidation and the reduction chemical reaction, and transport through the external circuit where the electricity is made and utilized [30]. A methanol/water liquid mixture diffusion takes place in the gas diffusion layer (GDL), which are usually carbon substrate (carbon paper or carbon cloth) and can uniformly disperse methanol in the anode and oxygen in the cathode. The MOR, ORR and overall reaction of DMFCs can be expressed by the following reactions: [29, 30]

$$CH_3OH + H_2O \ \rightarrow \ CO_2 + 6H^+ + 6e^- \quad \text{anode reaction} \tag{2-1}$$

$$\frac{3}{2}O_2 + 6H^+ + 6e^- \ \rightarrow \ 3H_2O \quad \text{cathode reaction} \tag{2-2}$$

$$CH_3OH + H_2O + \ \frac{3}{2}O_2 \ \rightarrow \ CO_2 + 3H_2O \quad \text{overall reaction} \tag{2-3}$$
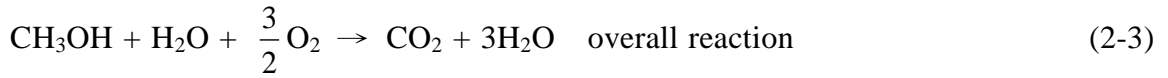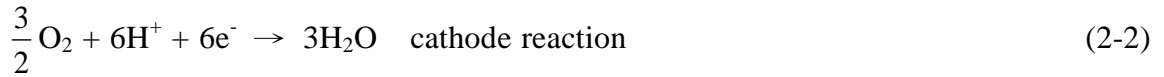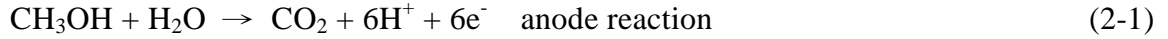
2.2 Direct methanol alkali fuel cells (DMAFCs)

Although extensive study on DMFCs has been being carried out for several decades, practical commercialization of DMFCs still faces many challenges associated with materials and technical shortcomings, including high cost of Pt-based electrocatalysts, low electroactivity of methanol oxidation reaction (MOR), poor kinetics of oxygen reduction reaction (ORR), and methanol crossover [29, 31]. Among various attempts to improve electrochemical performance of DMFCs, the study on the improvement in the electrocatalytic activity of Pt toward MOR receives the most attention. One major approach to improving the MOR electroactivity is to increase the resistance of Pt catalysts against CO poisoning, which results from catalytic site blocking by carbonaceous byproducts due to incomplete methanol oxidation [29, 30, 32].

Pt is known to have a higher CO tolerance in alkaline media than in acidic media, and thus exhibit better electrocatalytic performance for methanol oxidation in alkaline electrolytes [33, 34]. The better CO tolerance in alkaline media is generally ascribed to the abundance of OH$^-$ ions in the electrolyte, which can effectively oxidize carbonaceous adspecies on the Pt catalyst via the Eley-Rideal (E-R) mechanism [35, 36]. Because the electrocatalytic activity of Pt toward MOR can be readily improved by using alkaline electrolytes, direct methanol alkali fuel cells (DMAFCs), which is an alkali analogue of DMFCs, have recently received much interest. Besides, compared with DMFCs, DMAFCs have a faster oxygen reduction kinetics [29, 37] and less methanol crossover [38].
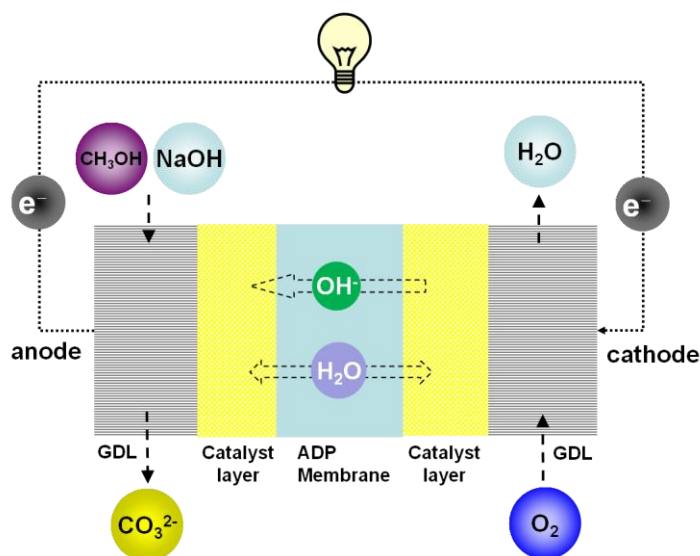
Figure 2-2 Schematic illustration of DMAFCs using alkaline system is shown. The MOR and ORR occur at the anode and cathode, respectively. Electricity is made and utilized in the external circuit.

DMAFCs operate using anion-exchange membranes, which provided a suitable ionic conductivity, as the electrolyte. A schematic of the electrochemical reaction and the process of transportation in the DMAFCs are shown in Fig 2-2. Because the process of the chemical reactions is in alkaline media, the MOR and ORR will be with slight differences in the alkaline media and acidic media. At the cathode, oxygen reacts with water and electrons, which are produced at the anode, and OH^- ions will be produced. The OH^- ions will migrate through the anion exchange membrane, such as Morgane® ADP hydroxide ion conducting membrane [38], from the cathode to the anode. At the anode, methanol reacts with OH^- ions, which received from the cathode electrode or offered by KOH or NaOH electrolyte, and produce carbonates, water and electrons. The same process as DMFCs, the electrons transport through the external circuit from the anode to cathode carrying the electricity. The MOR, ORR and overall reaction of DMAFCs in alkaline system can be expressed by the following reactions: [38]

$$CH_3OH + 8OH^- \rightarrow CO_3^{2-} + 6H_2O + 6e^- \quad \text{anode reaction} \tag{2-4}$$

9

$$\frac{3}{2}O_2 + 3H_2O + 6e^- \rightarrow 6OH^- \quad \text{cathode reaction} \tag{2-5}$$

$$CH_3OH + 2OH^- + \frac{3}{2}O_2 \rightarrow CO_3^{2-} + 3H_2O \quad \text{overall cell reaction} \tag{2-6}$$
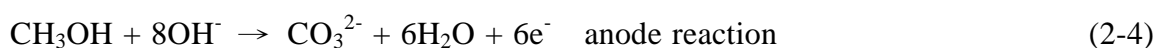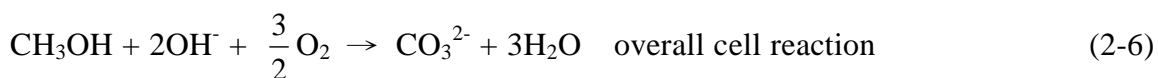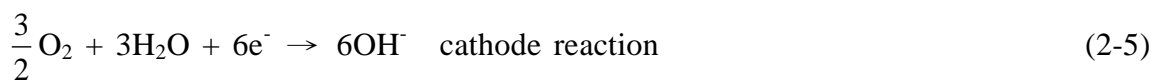
2.3 Electrocatalytic methanol oxidation reaction

Only a few materials, such as Pt and Pd, are found to be capable of adsorbing and oxidizing methanol.   Pt-based materials contribute a high enough activity and stability to be attractive as catalysts toward methanol electro-oxidation.   The overall reaction mechanism for the methanol oxidation reaction is shown in reaction (2-1).   The methanol oxidation reaction proceeds on Pt based catalysts followed by several steps of deprotonation.   Schematic diagrams of the adsorption/ deprotonation process on is shown in Figure 2-3 [29].

During the methanol oxidation, CO is formed on Pt surface.   The CO species can block the surface of the catalyst, such as Pt or Pd, and obstruct the MOR.   Therefore, to improve the CO tolerance, considerable studies used Pt-based binary or ternary alloys as the catalyst, in particular Pt-Ru to enhance CO electrro-oxidation.   To facilitate CO removal by oxidation to CO_2, it can be achieved by using oxygen containing species either from the water in solution or hydroxide ions [29].

Figure 2-4 shown a scheme of the possible reactions for MOR and their products [29]. The possible reaction pathways and products are shown in the scheme.   Each reaction step
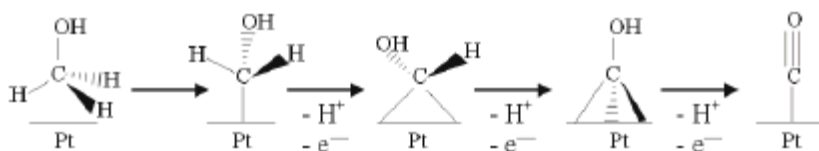
Figure 2-3 Schematic diagrams of the adsorption/ deprotonation process toward methanol electro-oxidation on Pt showing the consecutive stripping of hydrogen atoms.

$$CH_3OH \longrightarrow \underset{x}{C}H_2OH \longrightarrow \underset{xx}{C}HOH \longrightarrow \underset{xxx}{C}\text{-}OH$$

$$\downarrow \qquad \qquad \downarrow \qquad \qquad \downarrow$$

$$CH_2O \longrightarrow \underset{x}{C}HO \longrightarrow \underset{x}{C}O$$

$$\downarrow \qquad \qquad \downarrow$$

$$HCOOH \longrightarrow \underset{x}{C}OOH$$

$$\downarrow$$

$$CO_2$$
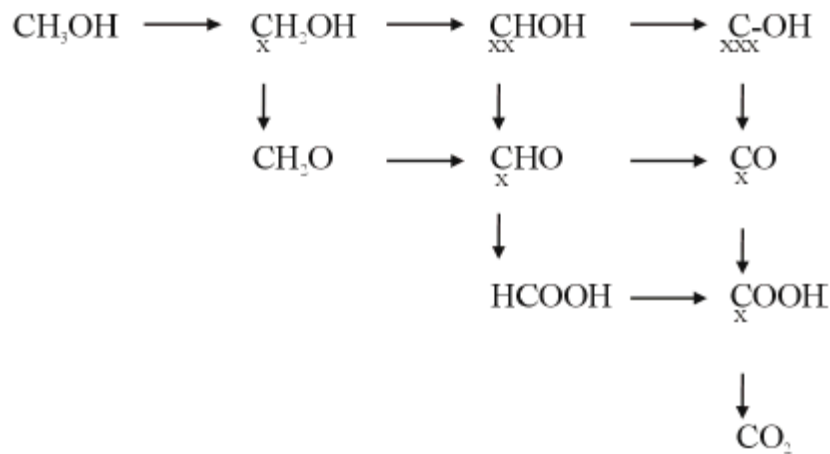
Figure 2-4 Reaction scheme for methanol oxidation showing all the possible reaction products and possible reaction paths.

denotes the transfer of one electron. Oxidation by adsorbed OH occurs in the perpendicular direction; stable compounds are located on the hypothenus; and dehydrogenation occurs in the direction from left to right. The schematic diagram illustrates that CO is an intermediate product during the methanol electro-oxidation.

2.4 Anode materials of DMFCs

Platinum has a superior electrocatalytic activity toward methanol oxidation reaction (MOR) and, therefore, Pt or Pt-based alloys are fundamentally the most preferred catalyst used in direct methanol fuel cells (DMFCs). On the other hand, to improve the CO tolerance, considerable studies used Pt based binary or ternary alloys, such as Pt-Ru, Pt-Ni and Pt-Pd, as the catalyst to enhance CO electro-oxidation via the bifunctional mechanism and/or the so called electronic effect [3-10]. Metal oxides, such as TiO_2, CeO_2, SnO_2 and RuO_2, can also effectively improve the CO tolerance of the Pt catalyst when they used as a promoter or the catalyst support based on a similar principle [13-15, 20-22, 39].

2.4.1 Pt-Ru nanoparticles on carbon nanotubes

Carbon nanotubes (CNTs) are attractive very much for electrochemical and catalytic applications because their uniform structure, electronic properties, electrochemical stability in both acidic and alkaline media. In the past few years, Pt or Pt-Ru nanoparticles decorated on CNTs are extensively utilized as electrode materials for the anode of DMFCs. Tsai et al. introduced ethylene glycol (EG) as a reducing agent for potentiostatic electrodeposition of Pt or Pt-Ru on CNTs, which were directly grown on carbon cloth by thermal CVD [9]. EG contributes the dechlorination of Pt or Ru precursor salts and promotes the formation of Pt or Pt-Ru nanoparticles. It is also used to prevent the particles from agglomeration. Figure 2-3 exhibits the TEM micrographs of (a) the Pt nanoparticles and (b) the Pt-Ru nanopaarticles decored on CNTs. The mean particle size of the Pt/CNTs and the Pt-Ru/CNTs are 9.5 nm and 4.8 nm, respectively. The addition of EG favorably reduced the particle size of Pt and Pt-Ru catalysts and prevented them from the serious agglomerations.

The Cyclic voltammograms of (A01) the Pt/CNTs and (A02) the Pt-Ru/CNTs at 20 mVs^{-1} in N_2 saturated 0.5 M H_2SO_4 + 1 M CH_3OH were shown in Figure 2-4. Pt-Ru/CNTs exhibited a relatively higher I_f/I_b ratio and mass activity than the Pt/CNTs.
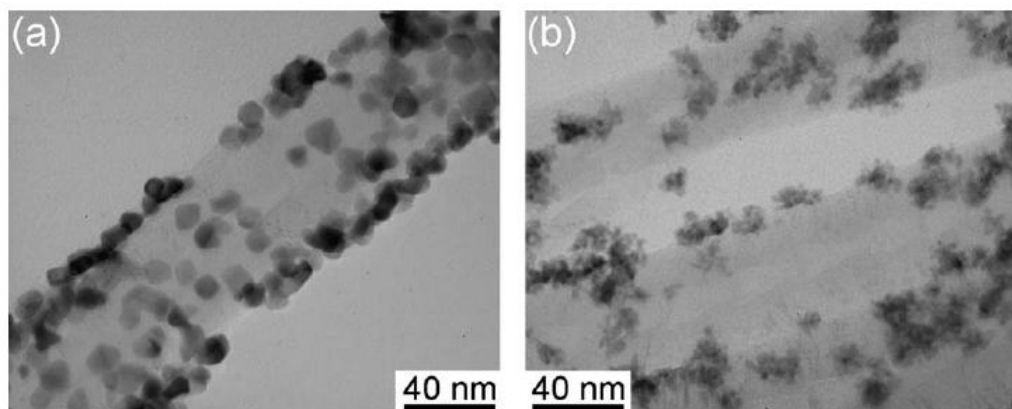
Figure 2-5 TEM images of (a) the Pt nanoparticles and (b) the Pt-Ru naoparticles decored on CNTs.

Figure 2-6 Cyclic Voltammograms of (A01) the Pt/CNTs electrode (A02) the Pt-Ru/CNTs electrode at 20 mVs^{-1} in N$_2$ saturated 0.5 M H$_2$SO$_4$ + 1 M CH$_3$OH aqueous solution.

For the Pt-Ru/CNTs electrode, the CO desorption peak current densities during the reverse scan (I$_b$) was lower than it of Pt/CNTs. It indicated that the presence of Ru indeed enhances the CO tolerance on the Pt surface and the methanol oxidation reaction of the electrode.

2.4.2 Pt-Ru nanowire array electrodes

Zhao et al. prepared Pt and Pt-Ru nanowire array electrodes by DC electrodeposition of Pt and Ru into the pores of an anodic aluminum oxide (AAO) template on a Ti/Si substrate [8]. AAO films were grown on a Ti/Si substrate and used as a template to synthesize a high surface area and ordered nanowire array electrode for MOR. The electrochemical measurements were performed in an 0.5 M CH$_3$OH + 0.5 M H$_2$SO$_4$ aqueous solution using the nanowire array as the working electrode. Figure 2-7 (a) shows a TEM image of the Pt-Ru nanowires and reveals that the nanowires obtained on the Ti/Si substrate are the regular size and the continuation. From SEM image (Figure 2.7 (b)), many clusters protrude from the Ti/Si substrate and provide a high surface area electrode. It also indicates that the nanowire array electrode has 10 cm^2 of Pt area per cm^2 of substrate electrode area, from the diameter and the length of the nanowires, and is higher than the

13
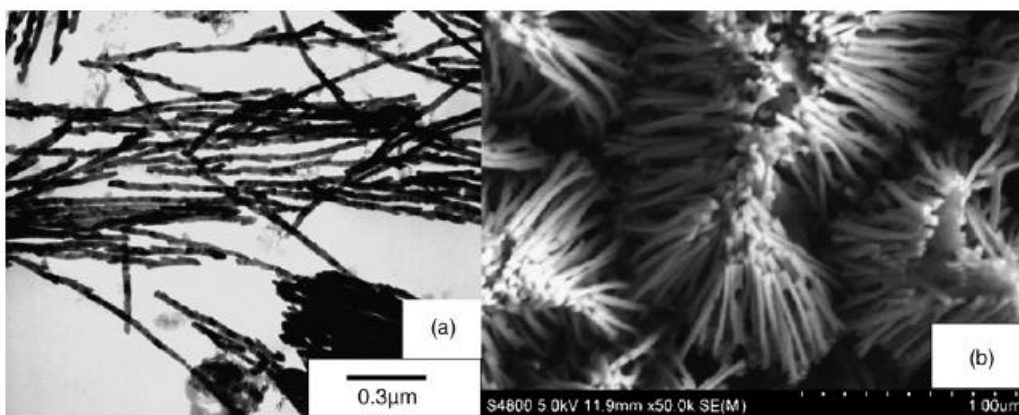
Figure 2-7 TEM (a) and SEM (b) images of the Pt-Ru nanowire array electrode.

Pt-Ru black (2.1 cm^2 Pt/ cm^2).

The CV curves of methanol oxidation for the Pt (a) and the Pt-Ru (b) nanowire array electrode surface in a solution of 0.5 M CH$_3$OH + 0.5 M H$_2$SO$_4$ were shown in figure 2-8. For the Pt-Ru nanowire array electrode surface, the peak potential for methanol oxidation shifted negatively by over 130 mV compared with the Pt nanowire array electrode. The I$_f$/I$_b$ ratio of 1.28 for Pt-Ru nanowire array electrode is also higher than that of Pt (1.08). The negative shift of peak potential and the higher I$_f$/I$_b$ ratio can be indicated the improved CO tolerance of the Pt-Ru nanowire array electrode. The Pt-Ru nanowire array electrode
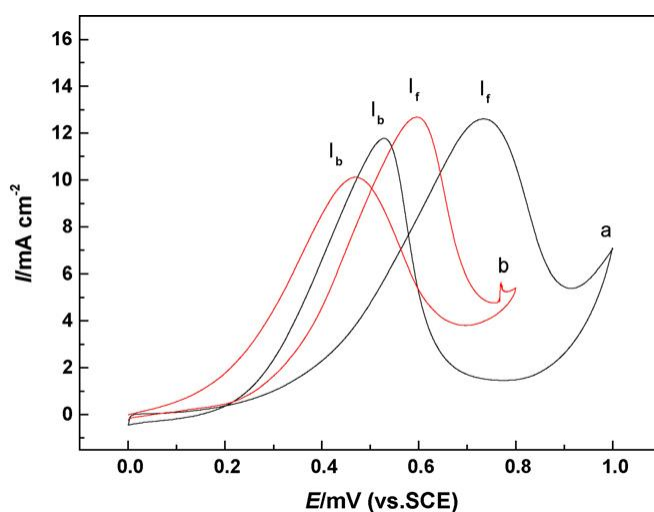
Figure 2-8 Cyclic voltammograms of methanol electro-oxidation for the Pt nanowire array eletrode (a) and Pt-Ru nanowire array electrode (b) in the 0.5 M CH$_3$OH + 0.5 M H$_2$SO$_4$ solution. The scan rate was 20 mVs^{-1}.

also has a higher current density after 500s in the chronoamperograms measurement. That can be ascribed by the bi-functional mechanism in which the reaction occurs between strongly bound Pt_3CO species and OH on the neighboring Ru sites.

2.4.3 Sulfated ZrO_2/MWCNT composited as supports of Pt catalysts

Sulfated zirconia supported on multi-walled carbon nanotubes as new supports of Pt catalyst (Pt-S-ZrO_2/ MWCNT) was synthesized, aiming at enhancing electron and proton conductivity and also catalytic activity of Pt electrocatalyst in terms of larger concentrations of ionizable OH groups on surfaces [40]. Pt-S-ZrO_2/MWCNT catalyst show higher catalytic activity for methanol electro-oxidation compared with Pt catalyst on nonsulfated ZrO_2/MWCNT support and commercial Pt/C (E-TEK). Sulfated ZrO_2 is superacid and good proton conductor, as support for Pt catalyst may increase the utilization of the Pt catalyst for methanol oxidation because of the proton conductivity shown as in Fig. 2-9. On the other hand, the oxidation of CO requires an adsorbed OH species adjacent to the adsorbed CO. The SO_4^{2-} group on ZrO_2 surface will increase the hydrophilic properties of ZrO_2 and the more dissociative hydroxyl of H_2O absorbed on the solid superacid than that non-sulfated ZrO_2, thus sulfated ZrO_2 can more easily transform CO_{ads} to CO_2 by the hydroxyl on its surface according to the bi-functional mechanism, releasing the active sites of Pt for further electrochemical reaction.
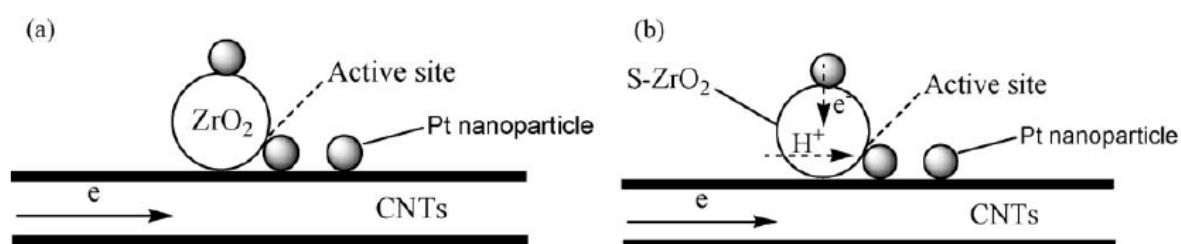
Figure 2-9 Schematic diagrams of the novel catalysts
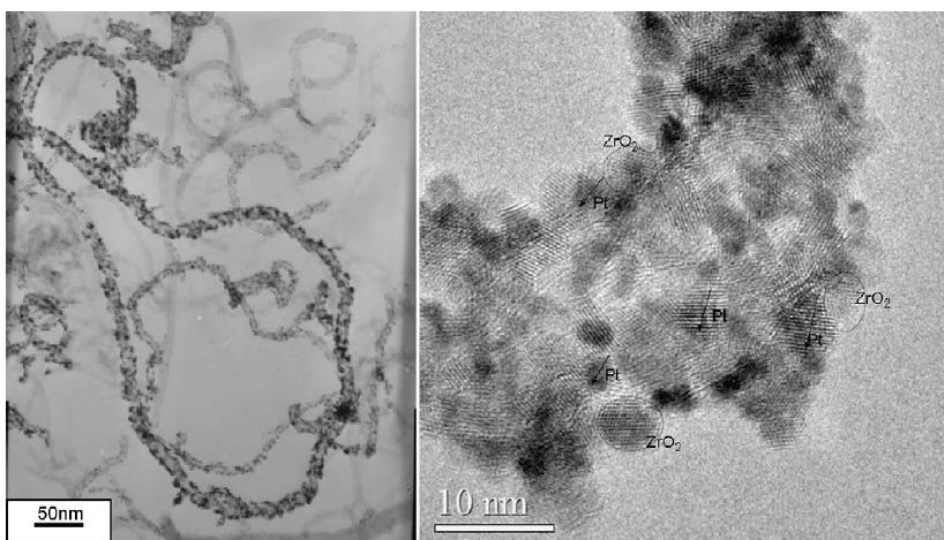
Figure 2-10 TEM and HRTEM images of Pt-S-ZrO$_2$/MWCNT composites.

Figure 2-10 shows the typical TEM and HRTEM images of the Pt-S-ZrO$_2$/ MWCNT composites. It can be seen that the Pt and S-ZrO$_2$ nanoparticles are relatively uniformly distributed on the sidewalls of the MWCNTs. The HRTEM micrograph reveals that both Pt and S-ZrO$_2$ nanoparticles attached on the sidewalls of the MWCNTs. Fig. 2-11 shows that the pattern of current decay was different for each catalyst. For both the catalysts, the current decayed continuously even after 1 h, supposedly because of catalyst poisoning by
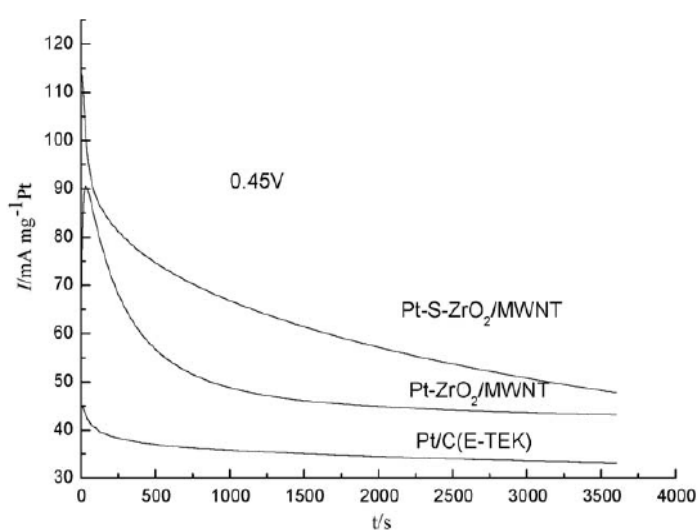
Figure 2-11 Chronoamperograms of various electrodes at 0.45 V in 1.0 M HClO$_4$ + 1.0 M CH$_3$OH aqueous solution.

16

the chemisorbed carbonaceous species and the depletion of OH sites which are responsible for oxidation of CO. The Pt-S-ZrO$_2$/ MWCNT was able to maintain the highest current density throughout all the ranges up to 3600 s among all the catalysts. The catalytic activity of Pt-S-ZrO$_2$/MWCNT catalysts was much higher than that of Pt-ZrO$_2$/MWCNT and Pt/C. This would be due to the strengthening of both the bi-functional mechanism and higher electron and proton conductivity of S-ZrO$_2$/ MWCNT composites.

2.4.4 Preparation of Pt/CeO$_2$-CNT through spontaneous adsorbing Pt nanoparticles onto CNTs

Through a two-step strategy, Pt/CeO$_2$-CNTs and Pt/CNTs were prepared by first microwave heating H$_2$PtCl$_6$ in NaOH ethylene glycol solution and then depositing Pt nanoparticles onto CeO$_2$–CNTs and CNTs, respectively [41]. Figure 2-12 shown the HRTEM of Pt/CeO$_2$-CNTs. In Fig. 2-12 (a) three Pt nanoparticles were found to be surrounded by CeO$_2$ nanoparticles, which can be clearly distinguished from the lattice distance (~ 0.305 nm for CeO$_2$ (111), ~ 0.225 nm for Pt (111). From Fig. 2-12 (b) we can
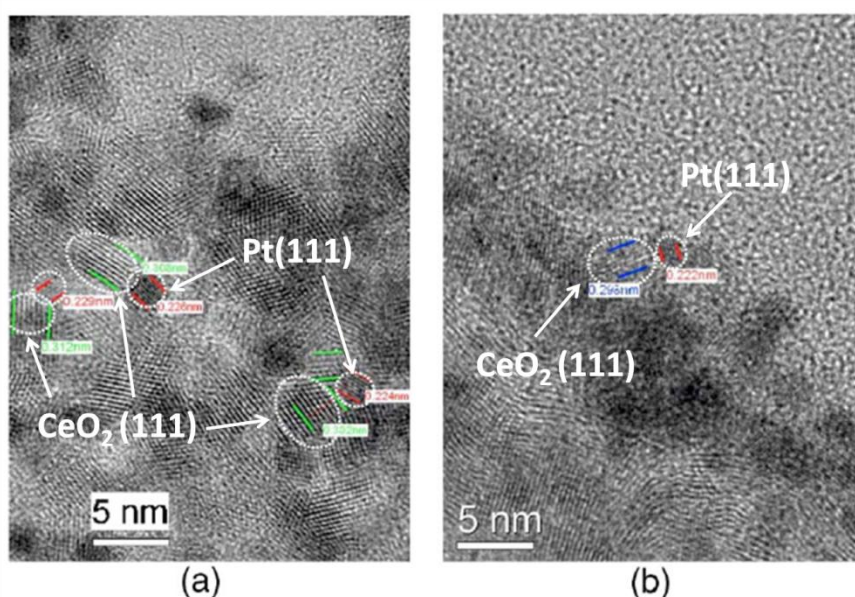
Figure 2-12 HRTEM image of CNT–CeO$_2$/Pt catalyst.
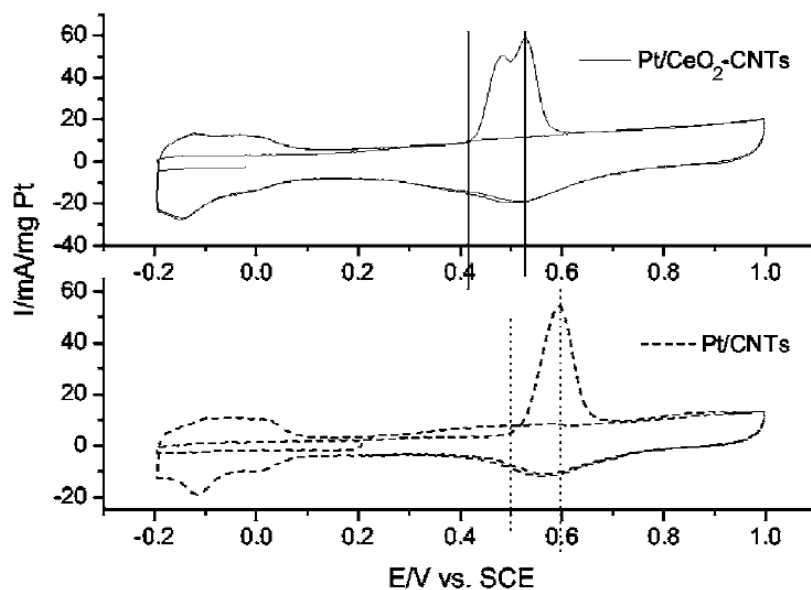
Figure 2-13 CO stripping curves on Pt/CNTs and Pt/CeO$_2$–CNTs recorded in 1 M HClO$_4$.

clearly see the Pt nanoparticles on sidewall of CeO$_2$-CNTs adjacent to CeO$_2$ particles.

Because CO electro-oxidation is viewed as a rate-determining step during methanol electro-oxidation, CeO$_2$ would promote methanol electro-oxidation on Pt-based catalysts according to the bi-functional mechanism. To verify the role of CeO$_2$ in Pt/CeO$_2$-CNTs, Wang et al. performed the potentiodynamic and potentiostatic electro-oxidation of CO adlayer on Pt, as shown in Fig. 2-13 [41]. The CO stripping on Pt/CeO$_2$-CNTs starts at 0.41 V, 0.08 V lower than 0.49 V on Pt/CNTs. In addition, the peak potential of CO stripping lies at 0.52 V on Pt/CeO$_2$-CNTs while lying at 0.6 V on Pt/CNTs. Such results indicate that CO can be electro-oxidized more easily on Pt/CeO$_2$-CNTs than on Pt/CNTs. In Fig. 2-13, two peaks on Pt/CeO$_2$–CNTs, possibly because that there are different contact states between Pt and CeO$_2$. The results in Fig. 2-13 indicate that CO can be electro-oxidized on Pt/CeO$_2$-CNTs more easily than on Pt/CNTs. This is possibly because CeO$_2$ can provide oxygen-containing group to electro-oxidize CO, the major intermediate during methanol electro-oxidation. Therefore, CeO$_2$ can be viewed as promising cocatalyst for methanol electro-oxidation on Pt-based catalysts.

2.3.5 Pt nanoparticles on SnO$_2$ nanowire-based electrodes

Because carbon nanotubes (CNTs) and nanofibers (CNFs) have unique properties, such as high surface area, good electronic conductivity, strong mechanical properties, and chemical stability, they have attracted great attention as promising catalyst supports. A number of research groups have demonstrated the advantages of using CNTs or CNFs as supports to better disperse Pt and its alloys for oxygen reduction and methanol oxidation reaction. In particular, the nanotube-based 3D electrode structure has shown very promising implications. Unlike CNTs, nanowires (NWs) can be made of various
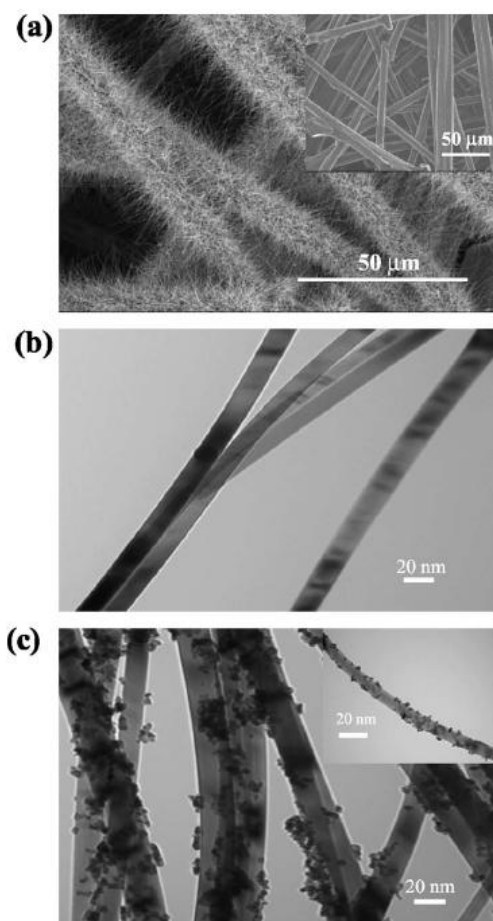
Figure 2-14 SEM and TEM micrographs of SnO$_2$ NWs grown on carbon fibers of carbon paper by thermal evaporation method. (a) SEM image showing full coverage of SnO$_2$ NWs on fibers of carbon paper. (Inset) Fibers of bare carbon paper. (b) TEM image showing individual SnO$_2$ NWs. (c) TEM images showing Pt nanoparticles electrochemically deposited onto SnO$_2$ NWs (Inset) Pt nanoparticles deposited onto a single SnO$_2$ NW

compositions of materials and they have solid cores.   NWs have demonstrated superior electrical, optical, mechanical, and thermal properties.   Metal oxide NWs have unique advantages as supports for dispersing noble metal nanoparticles such as Pt for practical applications.

Saha et al. prepared the composite electrodes by electrochemical deposition of Pt nanoparticles onto the surface of SnO_2 nanowires directly grown on the carbon fibers of a carbon paper [22].   In the comparison to a standard Pt/C electrode, the nanowire-based electrode exhibited higher electrocatalytic activity both for oxygen reduction reaction and methanol oxidation reaction.   Figure 2-14 shows the SEM and TEM images of the SnO_2 NWs grown on a commercially available carbon paper backing used in fuel cell applications.   As shown in fig. 2-14 (a), a thin layer of high-density SnO_2 NWs completely cover the surface of the carbon fibers in the carbon paper.   Figure 2-14 (b) shows that the NWs have a straight-line morphology.   Figure 2-14 (c) presents the TEM image of the Pt nanoparticles electrochemically deposited on the SnO_2 NWs.   The successful deposition of
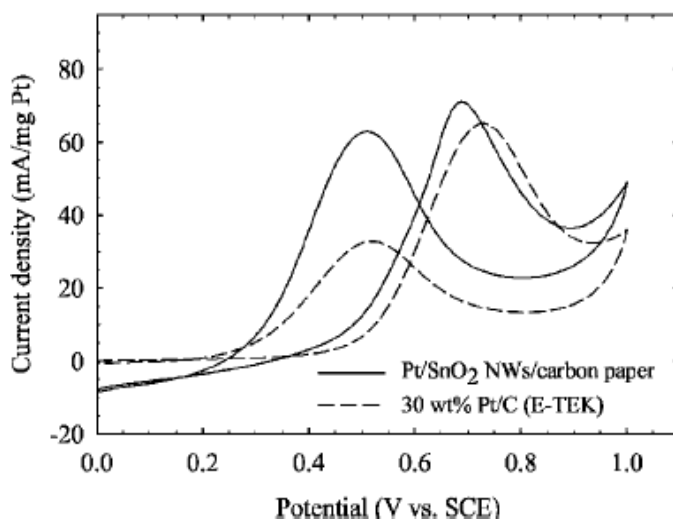
Figure 2-15 CVs for methanol oxidation reaction in 1 M H_2SO_4 aqueous solution with 2 M MeOH at Pt/SnO_2 NW. carbon paper with 0.12 mg/cm^2 Pt loading and standard 30 wt % Pt/C electrode with 0.1 mg/cm^2 Pt loading.   Potential scan rate 50 mV/s.   The current normailized on the basis of Pt loading.

Pt nanoparticles indicates a good electrical contact between the SnO_2 NWs and the carbon fibers. Furthermore, the electrochemical performance of the Pt/SnO2 NW/carbon paper electrode for methanol oxidation was also examined and the corresponding results are shown in Fig. 2-15. Compared with the Pt/C electrode, the oxidation peak current for the Pt/SnO_2 NW/ carbon paper electrode is about 71.5 mA/mg$_{Pt}$, which is higher than that of the Pt/C electrode, suggesting a higher utilization of Pt for methanol oxidation reaction. The significant improvement in catalytic activites of the Pt/SnO_2 NW/carbon paper composite electrode may be attributed to the following: (1) the unique 3D structure and electronic properties of SnO_2 NWs, (2) strong interaction between Pt catalyst particles and the SnO_2 NW surface, (3) synergies resulting from the combined properties of Pt nanoparticles and SnO2 NW supports, and (4) low impurities of SnO_2 NW compared to Vulcan carbon XC-72 which contains a significant amount of organosulfur impurities, which can poison the Pt metal.
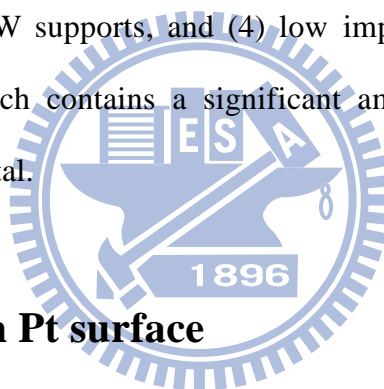
2.5 Adsorbed CO on Pt surface

CO adlayers of different coverages were produced by a dosing preocedure and their electrooxidative removal was studied by Koponen et al [42]. Figure 2-16 shown that the CO stripping voltammetry for pure catalyst ink electrode in 0.5 M H_2SO_4 for submono and saturation adlayers which is created by dosing of CO containing electrolyte for various periods of time. CO-oxidation processes present at 0.79 and 0.85-0.88 V. For CO on Pt(111), two main oxidation peaks are found, one minor and stationary at intermediate coverages, and one that shifts to the higher potential as a function of increasing CO coverage. The potential values of the stationary are 0.75 V and 0.83 - 0.88 V for the shifting peak. The stationary peak takes place at saturation coverage for the Pt(111) electrode. The stationary low potential peak may be contributed by (110) sites on the
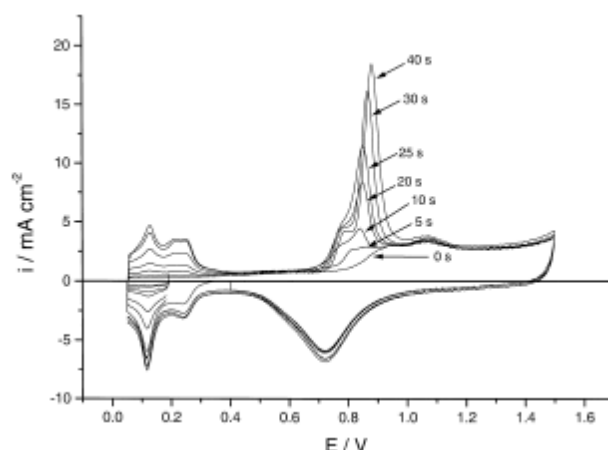
Figure 2-16 CO stripping voltammetry for Pt catalyst ink electrode in 0.5 M H₂SO₄ for submono and saturation adlayers created by dosing of CO containing electrolyte for various periods of time. CO was dosed at 0.2 V and the scan rate was 50 mVs⁻¹.

crystallite; for saturated adlayers of CO on Pt(110) a single oxidation peak at 0.75 V is found. Another possibility may result from the oxidation of CO on edge sites on Pt (111) planes of the crystallite. The behavior of CO adsorbed on edge sites is similar to the CO present in loosely packed submonolayers on Pt(111) electrodes and this results oxidized at a lower potential.

2.6 Electrochemical behavior of Palladium electrode

Palladium presents high catalytic activity towards several electrochemical processes, such as the methanol oxidation reaction (MOR), hydrogen absorption and adsorption and the hydrogen evolution reaction (HER). The crucial difference characteristic between Pd and Pt is the capability of adsorbing the hydrogen [43]. The hydrogen absorption into Pd takes place in the potential range of the under potential deposition of hydrogen (UPD H). However, desorption of hydrogen occurs at potentials higher that the onset potential of HER. On the other hand, the potential range of hydrogen absorption and adsorption is depended on the different metallic alloys and should be carried out by CV measurement.

22
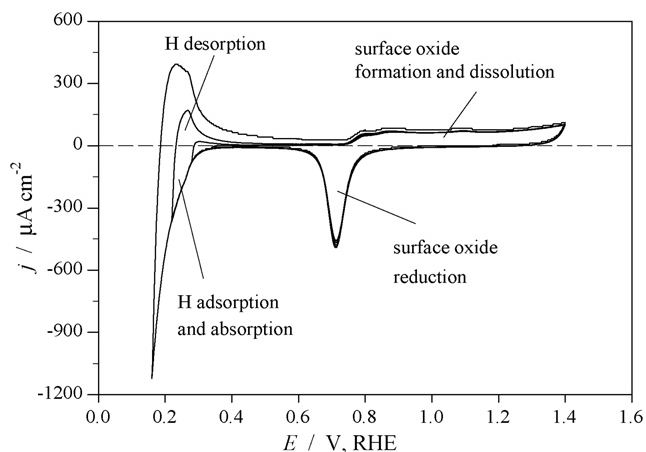
Figure 2-17 Cyclic voltammograms for Pd(poly) is in 0.5 M aqueous H_2SO_4 solution. The temperature was at 298 K and the scan rate is 50 mVs^{-1}. The CV profiles exhibit the oxidation of Pd begins at 0.65 V vs. RHE and graduate onset of hydrogen absorption upon decrease of the potential limit from 0.4 to 0.16 V, with the process commencing at 0.3 V.

Hydrogen adsorptions also one of the factors influencing the shape of CV profiles. Grden et al. exhibited a typical CV profile of Pd(poly) electrode in aqueous H_2SO_4 [43]. Figure 2-17 reveals that the hydrogen absorption and adsorption take place at the same potential range and commence at ca. 0.3 V vs. RHE. It also exhibits that the oxidation of Pd occurs at ca. 0.65 V vs. RHE and the reduction of Pd oxide starts at ca. 0.85 V vs. RHE. In the case of Pd metal, the potential region of the metal oxidation and the oxide reduction is not the same, as shown in figure 2-17. The electrochemical behavior is the nature of the surface compound formed and then reduced. Its chemical composition and structure depend on the oxidation conditions. Palladium oxides are prevailing materials and act as catalysts in various electrochemical studies but sometimes also as inhibitors in some processes, such as oxygen reduction reaction (ORR). The electro-oxidation of Pd and reduction of Pd oxide lead to changes in the surface morphology because soluble Pd compounds or oxide may generate during the electro-dissolution of Pd.

2.7 Bi-functional mechanism

2.7.1 Langmuir-Hinshelwood mechanism and Eley-Rideal mechanism

In the bi-functional mechanism model, hydroxyl surface groups can oxidize adjacent CO adspecies on the Pt catalyst, thereby avoiding CO poisoning. The reaction mechanism can be described by the Langmuir-Hinshelwood mechanism. In an Eley-Rideal surface reaction, the reaction product is formed by direct collision of a reactant species from the solution phase with an adspecies. In the case of CO electro-oxidation in the KOH solution, the carbonaceous adspecies on the Pt surface can be readily oxidized by the abundant OH^- ions in the electrolyte [23]. The CO electro-oxidation reaction does not only lie in the surface concentration of OH_{ad} species and CO_{ad} (L-H mechanism), but is strongly affected between the CO_{ad} and OH^- ions from the electrolytes (E-R mechanism).

Poisoning of the Pt surface by CO-like species produced during methanol oxidation is the major reason for the low rate of reaction. In order to solve the problem, Pt-based alloys or Pt/metal oxide composites are employed as a catalyst to increase the MOR activity and CO tolerance of electrode, based on a bi-functional mechanism. Song et al.
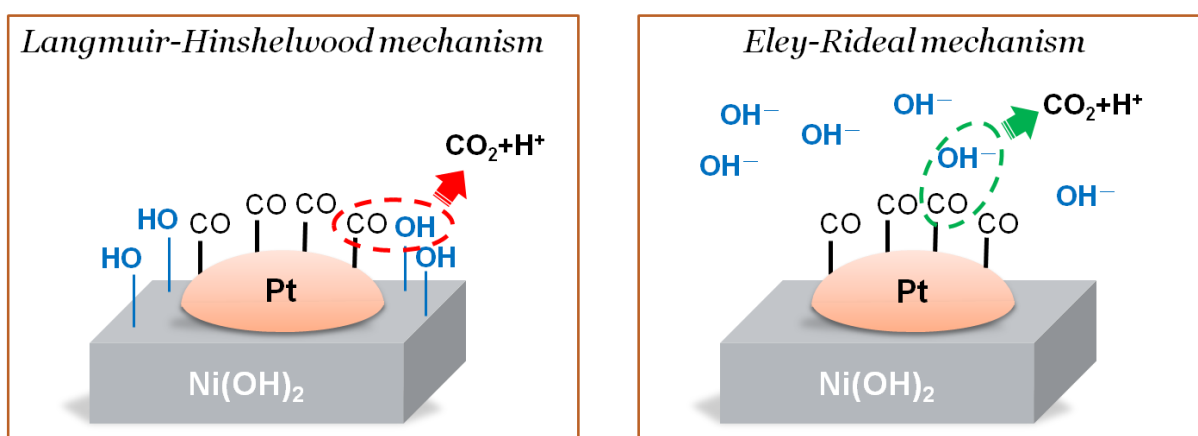
Figure 2-18 Schematic diagram illustrating the Langmuir-Hinshelwood mechanism and the Eley-Rideal mechanism.
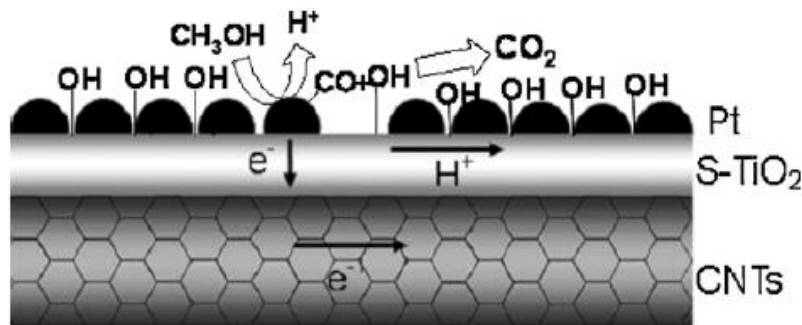
Figure 2-19 Schematic diagram of the structure of the novel catalyst Pt-S-TiO$_2$/CNT.

synthesized a new carbon nanotube-supported sulfated TiO$_2$ and Pt (Pt-S-TiO$_2$/CNT) by improved sol-gel and ethylene glycol reduction methods [44].   Careful structural design allowed the Pt nanoparticles to homogeneously disperse on a sulfated TiO$_2$ layer, which means that all of the Pt nanoparticles could be in direct contact with sulfated TiO$_2$.   This special catalyst structure, as shown in Fig. 2-19, and the high proton conductivity of sulfated TiO$_2$ increased the catalytic activity and CO tolerance of Pt for methanol electro-oxidation.   The CO stripping voltammograms showed that addition of sulfated TiO$_2$ is more beneficial for CO electro-oxidation. This can be attributed to the presence of more absorbed OH (OH$_{ad}$) on the S-TiO$_2$/CNT electrode and the carefully designed structure of Pt-S-TiO$_2$/CNT electrode.   These two factors are favorable for a bi-functional mechanism (L-H mechanism).

2.7.2 Surface electrochemistry of CO on Pt

Although the nature and adsorption site occupancy of CO$_{ad}$ are strongly dependent on the applied potential, the mechanism for CO$_{ad}$ oxidation on Pt (111) is independent of electrode potential; e.g., CO$_{ad}$ reacts with oxygen containing species through either a non-competitive or competitive Langmuir-Hinshelwood type reaction to form CO$_2$.   The physical state of oxygen-containing species is still uncertain (bulk H$_2$O, adsorbed H$_2$O or adsorbed OH).   Markovic et al. have proposed that CO$_{ad}$ is oxidized by OH$_{ad}$, the latter

species resulting from oxidative water decomposition in acid solution or from OH^- discharge in alkaline solution [45]:

$$CO_{ad} + OH_{ad} = CO_2 + H^+ + e^- \qquad\qquad (2\text{-}7)$$

Nevertheless, regardless of the true nature of the oxygen-containing species it was suggested that the kinetics of reaction do not depend only on the surface concentration of CO_{ad} and OH_{ad} species, but are strongly affected by a delicate balance between the coverage of and anions from electrolytes.

Recall that although the nature of CO_{ad} changes with electrode potential, the mechanism for CO_{ad} oxidation on Pt (hkl) follows the L-H reaction mechanism in the entire potential range [45]. Bergelin et al. suggested that in the preignition potential region CO_{ad} oxidation in CO free solution cannot proceed through the L-H mechanism, but rather through an Eley-Rideal mechanism, i.e. reaction between CO_{ad} and "activated" water molecules in the electrical double-layer [46]. Markovic et al. proposed that CO oxidation on Pt(111) will be considered to proceed through the L-H mechanism, in which the kinetics are strongly dependent on the delicate balance between the surface coverage of CO_{ad}, OH_{ad} and anions from supporting electrolytes [35].

2.8 Charge transfer between Pt particles and metal oxide support

Croy et al. presented the decomposition of methanol over Pt nanoparticles supported on a series of oxide powder [47]. The samples tested may be roughly grouped in two categories consisting of large and small Pt particles deposited on reducible (CeO_2, TiO_2) and non-reducible (SiO_2, ZrO_2, Al_2O_3) support. Figure 2-20 shows XPS spectra of Pt deposited on the different oxide powder supports measured after annealing at 500^oC. In fig. 2-13 (a), the solid lines indicate the positions of the main core-level peaks of metallic Pt at 71.1 eV ($4f_{7/2}$) and 74.3 eV ($4f_{5/2}$), the dashed lines Pt^{2+} in PtO (73.3 and 76.6 eV), and
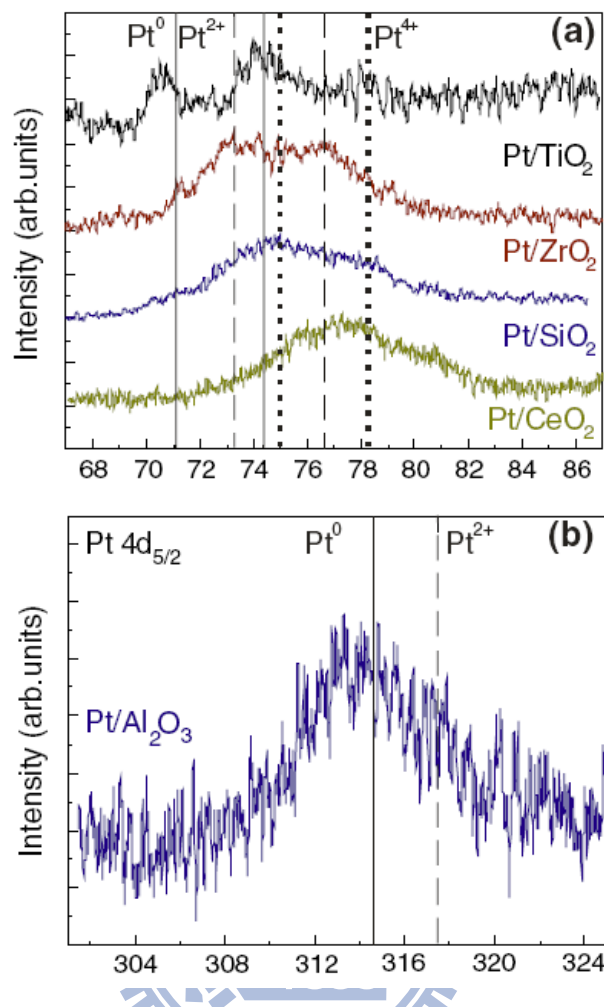
Figure 2-20 (a) Pt-4f core level XPS spectra of Pt nanoparticles supported on: (from top to bottom) TiO_2, ZrO_2, SiO_2, CeO_2. (b) Pt $4d_{5/2}$ from Pt/Al_2O_3. All spectra were measured after removal of the encapsulating polymer by annealing in air at 500 ^{o}C

the dotted lines Pt^{4+} in PtO_2 (75.0 and 78.8 eV). For the Pt/TiO_2 sample, it is predominantly metallic with the $4f_{7/2}$ appearing at ~ 70.5 eV. This corresponds to a negative binding energy shift of ~ 0.6 eV with respect to the bulk value of 71.1 eV. Such negative energy shifts can be explained by charge transfer to the particle from the support due to delocalized electron distributions arising from oxygen vacancies, or small particles with a large number of surface atoms having reduced coordination number. The Pt/CeO_2 sample appears highly oxidized (mainly Pt^{4+}) and the higher binding energies indicate a string interaction between the CeO_2 support and the Pt particles. The possible formation

of Pt-Ce alloys might explain the anomalously large binding energies observed in the XPS data of these samples.

The XPS data indicate that for similarly sized particles that state of oxidation of Pt depends on the support.   Because all samples underwent identical thermal treatments, the stability of $Pt^{\delta+}$ species can be affected by the choice of support.   This suggest that for MeOH decomposition, or perhaps in general, for reactions not involving the dissociation of O_2, the reducibility of the support plays a secondary role to the more important parameters of particle size and oxidation state of Pt.   The role of the support is that of a stabilizer, a provider of preferential/additional sites of interaction, and a mediator among the different oxides of Pt.

Chapter 3   Experimantal

3.1 Experimental flowchart

Figure 3-1 illustrates the experimental flowchart for the fabrications and analyses of the Pt/porous TiO_2, Pt/karst-Ni and Pt/PdO electrodes.   The porous TiO_2 and the karst-Ni electrodes were fabricated on p-type Si wafer; the PdO nanoflakes electrode was fabricated on graphite carbon cloth.   Pt nanoparticles were electro-deposited on the three electrodes by different galvanostatic pulse plating condition, respectively, for the study on methanol oxidation reaction (MOR).   Measurements of electrocatalytic activity of the Pt/porous TiO_2 and the Pt/PdO electrodes were in acidic system, and it of the Pt/karst-Ni electrode was in alkaline system.   The cyclic voltammetry (CV) measurement and CO stripping
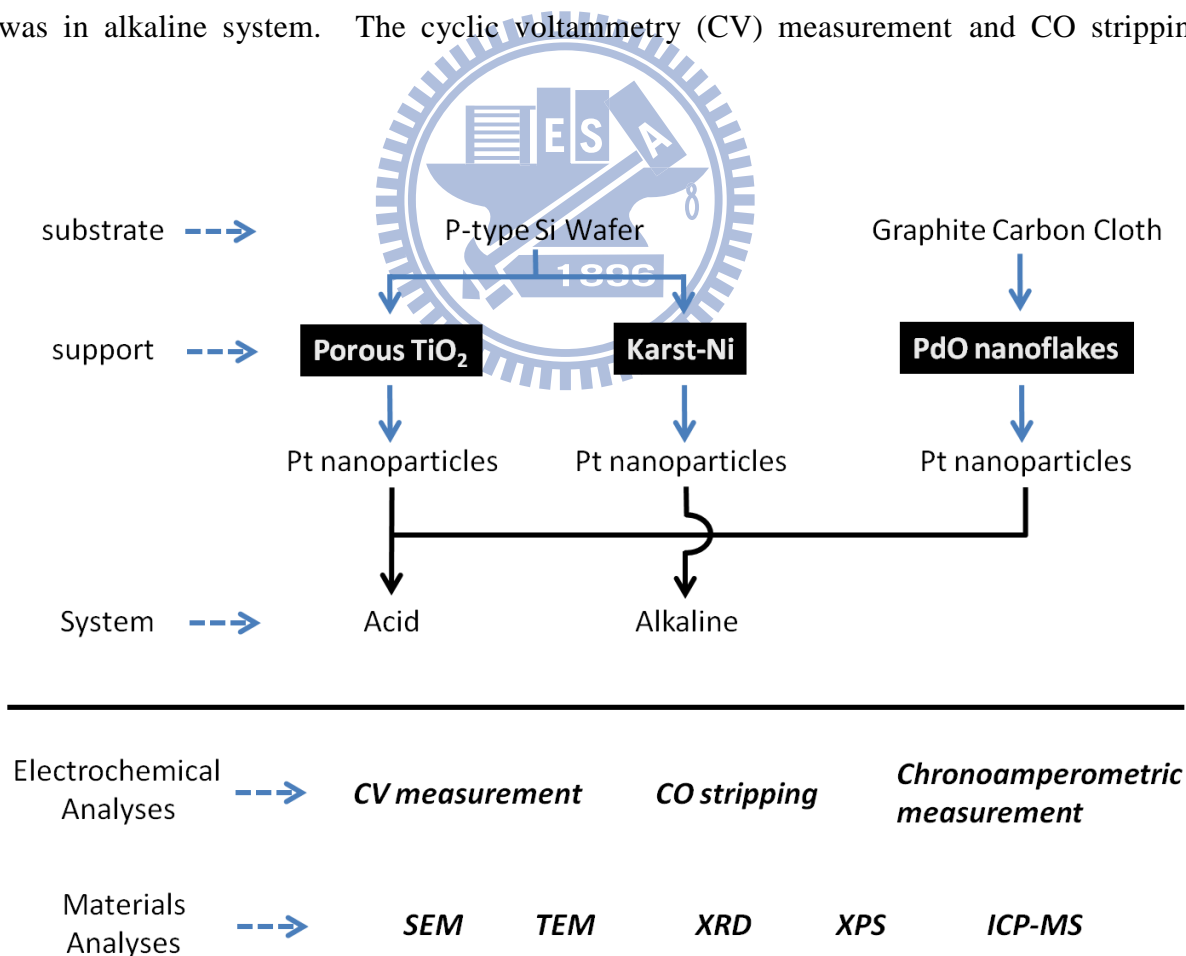
Figure 3-1 Experimental flowchart for the fabrications and analyses of the Pt/porous TiO_2, Pt/karst-Ni and Pt/PdO electrodes.

measurement were used to study the ability toward methanol electro-oxidation and CO tolerance, respectively, of electrodes. The chronoamperometry measurement was utilized to estimate the electro-activity stability of the electrode in the MOR electro-activity with long time. The surface morphology was examined by scanning electron microscopy (SEM). The crystallinity and the chemical composition of electrodes were studied by x-ray diffractomery (XRD) and x-ray photoelectron spectroscopy (XPS), respectively. The microstructure and particle size distribution of Pt nanoparticles were analyzed by transmission electron microscopy (TEM).

3.2 Preparation of Pt nanoparticles deposited on porous TiO$_2$ support
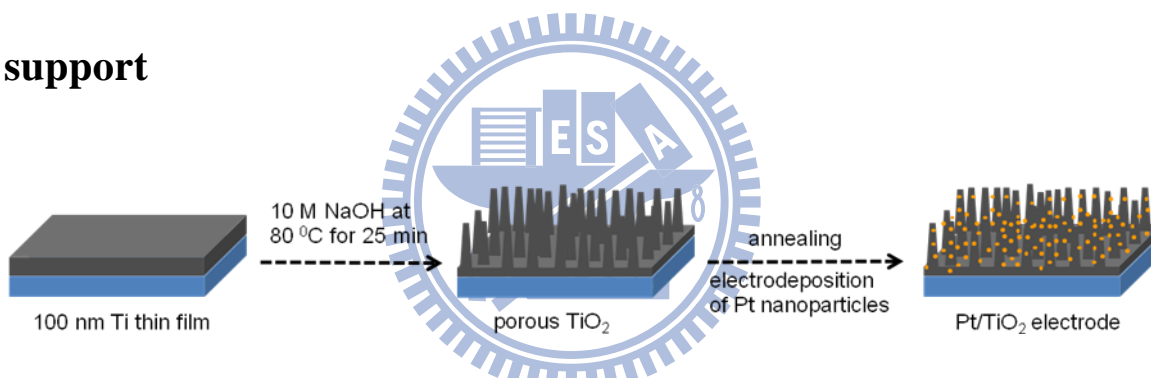
Figure 3-2 Experimental flowchart for the fabrications the Pt/TiO$_2$ electrode.

3.2.1 Preparation of the porous TiO$_2$ support

To prepared the porous titania support, a Ti thin film 100 nm thick was first deposited on a p-type 6-inch Si wafer of low resistivity (0.002 Ω-cm) by electron beam evaporation (e-beam) deposition. The Ti thin film coated silicon wafer was then immersed in the aqueous solution of 10 M NaOH at 80°C for 25 minute, followed by a rinse with 0.1 M HNO$_3$. Before the Pt nanoparticle deposition on the porous TiO$_2$ support, the as-synthesized thin film was annealed in vacuum (10^{-7} torr) at various temperatures to improve the electrical conductivity of the porous support.

3.2.2 Pulse electrodeposition of Pt nanoparticles on the TiO$_2$ support

Pt nanoparticles were electrodeposited on the TiO$_2$ support in the aqueous solution of 0.001 M H$_2$PtCl$_6$ (200 ml)/ 0.33 M HCl (2 ml) at room temperature by galvanostatic pulse plating in a three electrode cell system with a saturated calomel reference electrode (SCE). The vacuum annealed porous TiO$_2$ support was used as the working electrode and a Pt plate as the counter electrode. The particle size and dispersion of Pt nanoparticles can be controlled by tuning the pulse height of the applied current and the pulse duration. The time durations for the high current pulse (4 mA) and the low current pulse (-20 mA) were 2 and 1 ms, respectively. A total of 3000 pulse cycles was performed to deposit Pt nanoparticles on the porous TiO$_2$ support. For comparison, Pt particles of larger size were also electrodeposited on a blanket TiO$_2$ surface, which was prepared by annealing a Ti thin film 10 nm thick on the Si substrate in oxygen ambient at 600°C for 5 min., followed by vacuum anneal at 600°C for 1 h. A Pt island film and a blanket Pt thin film of 5 nm thickness were also deposited by pulse electrodeposition and e-beam deposition, respectively, on a metallic Ti thin film, which was e-beam deposited on the Si wafer. The mass loading of the Pt catalyst on the support was determined by inductively coupled plasma mass spectroscopy (Thermo X Series II).

3.3 Preparation of Pt nanoparticles deposited on PdO nanoflake support
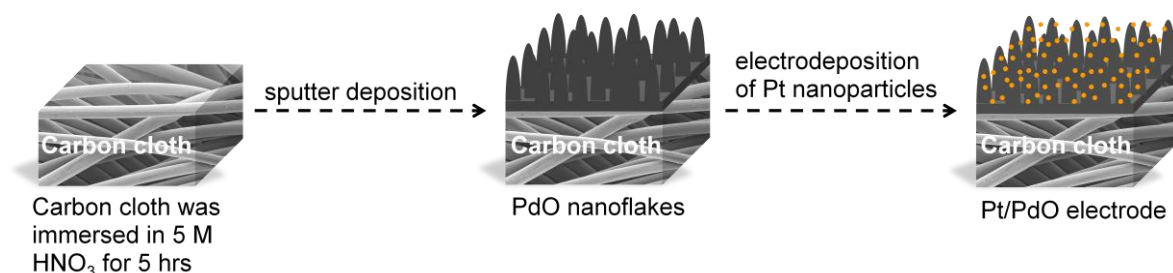
Figure 3-3 Experimental flowchart for the fabrications the Pt/PdO electrode.

3.3.1 Preparation of the PdO nanoflake support

PdO nanoflakes were deposited on carbon cloths at room temperatures by reactive sputter deposition (RSD) in a radio frequency magnetron sputter deposition system. The RSD condition for the PdO nanoflake thin film has been described in detail previously [48]. The palladium target was 2 in. in diameter with a purity of 99.99 %. The RSD was performed with a gas mixture of Ar (20 sccm) and O_2 (20 sccm) at the working pressure of 9×10^{-3} torr and an RF power of 50 W. Before the PdO deposition, the carbon cloth was immersed in the aqueous solution of 5 M HNO_3 at 25 ^{o}C for 5 hours, followed by a rinse with deionized (DI) water.

3.3.2 Pulse electrodeposition of Pt nanoparticles on the PdO support

Pt nanoparticles were electrodeposited on the PdO nanoflake support in a mixed aqueous solution of 0.001 M H_2PtCl_6 at room temperature by galvanostatic pulse plating in a two-electrode cell system. The PdO nanoflake support was used as the working electrode and a Pt disk (1.5 cm in diameter) as the counter electrode. During the pulse electrodeposition, the time durations for the positive current pulse (5 mA) and the negative current pulse (-10 mA) were 1 and 2 ms, respectively. A total of 400 pulse cycles were performed to deposit Pt nanoparticles on the PdO nanoflake support. For comparison, we also pulse-electrodeposited Pt particles on the carbon cloth support (denoted by Pt/C), and prepared a 10 nm thick Pt thin film on the carbon cloth by e-beam deposition (denoted by blanket-Pt). For the preparation of the Pt/C electrode, following Pt electrodeposition conditions were used: the DC pulse current: -1.0 mA, the pulse duration: 100 ms, the cycle period: 200 ms, and the total number of pulse cycles: 200. The Pt loading of the electrodes was determined by inductively coupled plasma mass spectrometer. Under the sample preparation conditions described above, the Pt/PdO, the Pt/C and the blanket-Pt electrodes had a Pt loading of 0.076, 0.031 and 0.081 mg/cm^2, respectively.

3.4 Preparation of Pt nanoparticles deposited on a karst-like Ni thin film
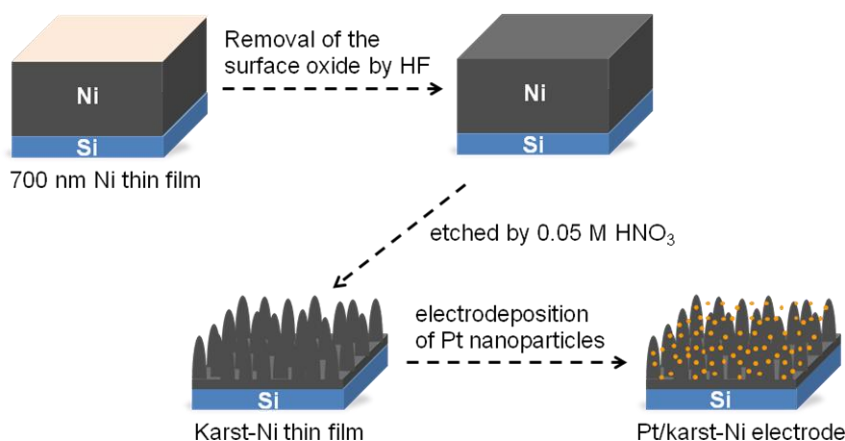
Figure 3-4 Experimental flowchart for the fabrications the Pt/karst-Ni electrode.

3.4.1 Preparation of the karst-Ni support

To prepare the karst-Ni support, a 10 nm thick Ti thin film and a 700 nm thick Ni thin film were sequentially deposited on a 6-inch p-type Si(100) wafer of low resistivity (0.002Ω-cm) by electron beam evaporation (e-beam) deposition.   The Ti thin film was used as the adhesion layer for the Ni thin film.   The Ni/Ti film was immersed in an aqueous solution of 8% hydrofluoric acid at 30°C for 3 min to remove the surface nickel oxide, followed by a rinse with deionized (DI) water.   The wet-cleaned thin film was then etched by an aqueous solution of 0.05 M HNO_3 to produce a rugged surface on the Ni thin film.   Before the pulse electrodeposition of Pt nanoparticles, the rugged Ni thin film received sequentially a rinse of DI water and a N_2 purge.

3.4.2 Pulse electrodeposition of Pt nanoparticles on the Ni support

Pt nanoparticles were electrodeposited on the karst-Ni support in a mixed aqueous solution of 0.001 M H_2PtCl_6 and 0.06 M HCl at room temperature by galvanostatic pulse plating in a two-electrode cell system.   The karst-Ni support was used as the working

electrode and a Pt disk (1.5 cm in diameter) as the counter electrode. During the pulse electrodeposition, the square wave pulsed current was switched between -1.0 mA and 0 mA, and both the anodic and cathodic pulse durations were 1 ms. A total of 800 pulse cycles were performed to deposit Pt nanoparticles on the karst-Ni support. For comparison, we also pulse-electrodeposited Pt particles on a blanket Ni thin film without the HNO_3 wet etch (denoted as Pt/Ni thereafter), and prepared a 5 nm thick Pt thin film on the Ti thin film capped Si wafer by e-beam deposition. For the preparation of the Pt/Ni electrode, following Pt electrodeposition conditions were used: the pulse current: -1.0 - 0 mA, the anodic and cathodic pulse durations: 100 ms, and the pulse cycle number: 200. The Pt mass loadings of the Pt/karst-Ni, the Pt/Ni and the Pt thin film electrodes discussed in the work are 0.064, 0.034 and 0.031 mg/cm^2, respectively.

3.5 Electrochemical measurements

3.5.1 Cyclic voltammetry (CV) measurement

Electrochemical measurements were conducted at room temperatures in the same electrochemical cells as that used for the Pt electrodeposition. The Pt/TiO$_2$, Pt/PdO or Pt/karst/Ni electrode were used as the working electrode and a Pt disk as the counter electrode. All aqueous solutions were prepared with low resistance DI water (~18 MΩ) produced by an ultrapure water purification system. The cyclic voltammetry (CV) measurement of methanol electro-oxidation was carried out in the mixture solution of 1 M H_2SO_4 + 1 M CH_3OH within the potential range of -0.2 to 0.9 V (vs. SCE) with a scan rate of 20 mVs^{-1}. In alkaline solution, the CV measurement was conducted in 1 M KOH + 1 M CH_3OH within the potential range from -1.04 to 0.4 V with a scan rate of 20 mVs^{-1}. Prior to the CV measurement, the electrolyte was purged with pure N_2 gas for 20 min to remove excess dissolved oxygen.

3.5.2 CO stripping measurement

The CO stripping measurement was conducted in a 0.5 M H_2SO_4 solution within the potential range of -0.2 to 0.9 V with a scan rate of 20 mVs^{-1}. The CO adsorption on the Pt catalyst was performed by flowing a 10% CO/N_2 gas mixture in the 0.5 M H_2SO_4 aqueous solution at 100 mV for 30 min. Before the CO stripping measurement, the solution was purged with pure N_2 gas for 10 min to remove CO remaining in the solution. In alkaline solution, the CO stripping measurement was carried out in a 1 M KOH solution within the potential range from -1.04 to 0.4 V with a scan rate of 20 mVs^{-1}. A monolayer of CO was adsorbed on the Pt/Ni catalyst by flowing a 10% CO/N_2 gas mixture in the 1 M KOH aqueous solution at -1.04 V for 30 min.

3.5.3 Chronoamperometric measurement

The chronoamperometric measurement for CH_3OH oxidation was carried out in the solution of 1 M H_2SO_4 + 1 M CH_3OH at 0.5 V for 3600 s and, in alkaline solution, 1 M KOH + 1 M CH_3OH at -0.3 V for 3600 s.

3.6 Materials Characterizations

3.6.1 Scanning electron microscopy (SEM)

Surface morphology of the samples was examined by scanning electron microscopy (SEM, JEOL JSM-6500F and JSM-6700F).

3.6.2 Transmission electron microscopy (TEM)

For the Pt-TiO_2 electrode, the microstructure and particle size distribution of Pt nanoparticles were analyzed by transmission electron microscopy (TEM, JEOL JEM-3000F). The TEM specimens were prepared by scratching off the Pt/TiO_2 layer from

the Si substrate with a pair of dissecting forceps in the presence of a small drop of ethanol, and then put onto a holly-copper grid and dried in air at the room temperature (~25 ^{o}C). For the Pt/PdO electrode, TEM specimens were prepared by mechanical separating nanoflakes from the carbon cloth using ultrasonic agitation in ethanol. For the Pt/karst electrode, the microstructure of the karst-Ni thin film and Pt nanopraticles was studied by Philips tacnai 20. To protect the rugged surface of the karst-Ni thin film from being damaged during TEM specimen preparation, a 400 nm thick SiO_2 overlayer was deposited on the film surface by high density plasma chemical vapor deposition.

3.6.3 X-ray diffractometry (XRD)

X-ray diffractometry (XRD, PANalytical X'Pert Pro) with the Cu Kα source was used to study crystallinity of the porous TiO_2 support vacuum-annealed at various temperatures and the karst-Ni thin film.

3.6.4 X-ray photoelectron spectroscopy (XPS)

The chemical composition of electrode samples were examined by x-ray photoelectron spectroscopy (XPS, Thermo VG 350). To calibrate the binding energy of photoelectrons emitted from bare nickel oxide samples, we deposited an Pt film on the sample surface by e-beam evaporation and used the Pt $4f_{7/2}$ peak as the reference. For the binding energy calibration for Pt loaded samples, an ultrathin Au film was deposited on the sample by thermal evaporation and the Au $4f_{7/2}$ peak was used as the reference.

3.6.5 Inductively coupled plasma mass spectroscopy (ICP-MS)

The mass loading of the Pt electrocatalyst on the support was determined by inductively coupled plasma mass spectroscopy (ICP-MS, Thermo X Series Ⅱ), and was used to calculate the electrochemical surface active area (ESA) and the mass activity of the

Pt catalyst.

Chapter 4　Electrocatalytic activity of Pt nanoparticles deposited on porous TiO$_2$ supports toward methanol oxidation

4.1 Introduction

TiO$_2$ is one of the most important transition metal oxides with a wide range of industrial applications.　TiO$_2$ has intriguing photocatalytic properties and excellent chemical stability in both acidic and alkaline solutions, and has long been used as a catalyst or support in photo-electrochemical systems.　Many recent studies on titania for DMFC applications prepared titania supports of high surface area for the Pt catalyst loading and found that the oxide supports could significantly enhance the electrocatalytic activity and the CO-tolerance of the Pt catalyst [49-54].　The better electrocatalytic properties of Pt/TiO$_2$ electrodes are usually attributed to the bi-functional mechanism and a strong metal-support interaction between the TiO$_2$ and the Pt catalyst [47, 55].　In the study, we used hydrothermal method to prepare porous TiO$_2$ thin film as a catalyt support and pulse-electrodeposited Pt nanoparticles on the porous thin film vacuum-annealed at 600°C. Electrochemical study shows that the annealed porous TiO$_2$ support can greatly improve the CO tolerance of the Pt catalyst, thus leading to a better electrocatalytic activity toward MOR.

4.2 Material characterizations

Figures 4-1(a) and (b) show the plane-view SEM images of the as-prepared hydrothermally synthesized TiO$_2$ thin film and the porous film annealed at 600°C for 3 hr (thereafter denoted as TiO$_2$-3h), respectively.　The thin film had a carpet-like morphology with collapsed thin sheets on the surface.　According to the cross-sectional SEM image
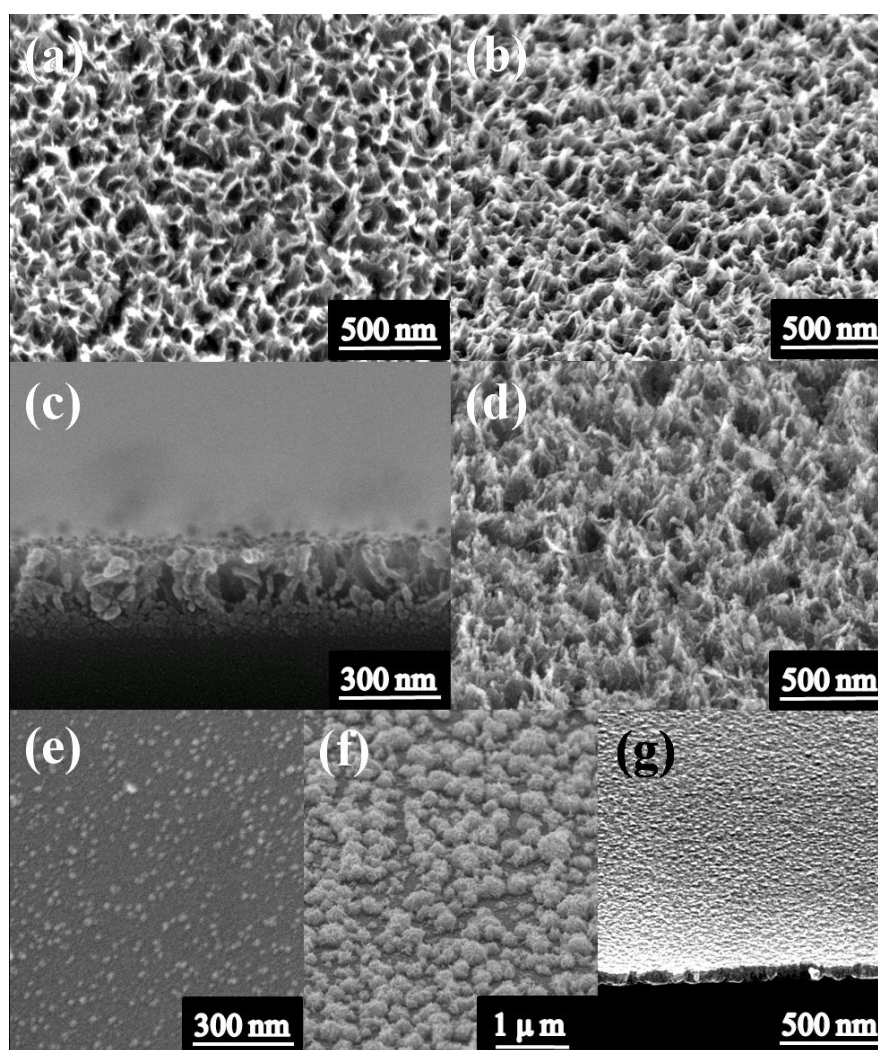
Figure 4-1 SEM images for (a) the as prepared porous TiO$_2$ thin film, (b) porous TiO$_2$-3h thin film, (c) cross-section of the porous TiO$_2$-3h thin film, (d) Pt nanoparticles deposited on the porous TiO$_2$-3h thin film, (e) Pt particles deposited on the blanket TiO$_2$ thin film, (f) Pt islands on the Ti substrate, and (g) blanket Pt thin film on the Ti substrate.

shown in Fig. 4-1(c), the hydrothermalized thin film had a two-layer structure with the carpet-like layer on the top and an ill-compacted granular layer on the bottom. The top and bottom layers were ~260 nm and ~65 nm thick, respectively. It is not clear to us at the present time why the two different microstructure layers were formed during the one step hydrothermal treatment. The top layer was virtually of a porous structure, which was constructed by mutually overlaying collapsed sheets. A careful examination from the cross-sectional SEM image of Fig. 4-1(c) reveals that the pore walls were composed of

nanosized grains connecting with one another, and with a wall thickness roughly the diameter of a grain, which was ~15-25 nm.   Compared to the blanket Ti thin film before hydrothermalization, the porous morphology of the hydrothermal TiO_2 thin film provided a much larger surface area for the Pt catalyst loading.   Figure 4-1(d) shows the plane-view SEM image of the TiO_2-3h thin film after the pulse electrodeposition of Pt catalyst (thereafter denoted as Pt/TiO_2-3h).   Because the electrodeposited Pt nanoparticles were very small in size and well dispersed on the TiO_2 pore structure as will be shown by TEM images, they are hardly observed in the SEM image.   Also shown in Fig. 4-1 are the SEM images of electrodeposited Pt particles on the blanket TiO_2 surface (Fig. 4-1 (e), Pt islands on the Ti thin film (Fig. 4-1(f) and the e-beam deposited Pt thin film (Fig. 4-1(g). Pt particles on the blanket TiO_2 thin film (thereafter denoted as Pt/TiO_2-tf) had a relatively uniform size distribution around ~15-20 nm and well dispersed on the surface.   For Pt islands deposited on the Ti surface (denoted as Pt/Ti), islands with sizes mostly larger than 300 nm covered nearly the whole Ti substrate surface.   On the other hand, the e-beam deposited Pt thin film completely capped the Ti substrate and will be denoted as the blanket-Pt electrode.   These three samples will be used for comparison when we discuss later about the electrocatalytic activity of the Pt/TiO_2-3h electrode.

TiO_2 is an n-type semiconductor, and the electrical conductivity of TiO_2 increases with the concentration of donor-like oxygen vacancies [56].   The conductivity may increase by more than 4 orders of magnitude when the oxygen/Ti stoichiometry ratio varies from 2.0 to 1.7 [57].   The electrical conductivity of a TiO_2 film can be greatly improved by a reducing treatment, e.g. thermal anneal under vacuum conditions [58].   Because the as-synthesized porous TiO_2 thin film had a relatively high electrical resistivity, Pt electrodeposition on the porous TiO_2 support was barely possible.   To increase the conductivity of the TiO_2 support, the as-prepared porous thin film was thermally annealed in a vacuum of 1×10^{-7} torr. Figure 4-2 shows XRD spectra of the TiO_2 thin film annealed at various temperatures.   For
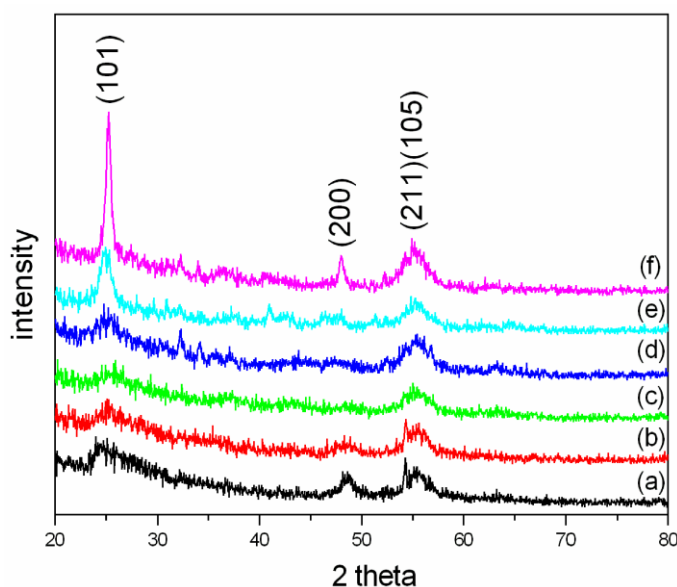
Figure 4-2 X-ray diffraction spectra of the porous TiO_2 thin film annealed at various temperatures for one hour: (a) as-prepared, (b) 300°C, (c) 400°C (d) 500°C (e) 600°C and (f) 600°C for three hours.

the as-prepared TiO_2 thin film (curve a), the two diffraction peaks situated at 25.4° and 48° are due to the anatase (101) and (200) lattice planes, respectively.   The peak at 55.5° may result from the overlap of the two adjacent peaks due to the anatase (211) and (105) lattice planes.   The three diffraction peaks were weak and broad, indicating poor crystallinity and/or finite size effect.   At temperatures below 500°C, the intensity of the three peaks decreased with the annealing temperature.   This was more apparent for the (200) plane, which was nearly undetectable at 400°C.   As the annealing temperature reached 500°C, the three peaks showed a reverse trend in the intensity variation, i.e. the peak intensity increased with the temperature.   For the sample annealed at 600°C for one hour, the anatase (101) peak became narrower with an obvious increase in the peak height.   When the annealing time increased to three hours, the anatase (101) peak grew much shaper and stronger, and the anatase (200) peak became clearly detectable with a narrow width.   The XRD analysis suggested that the thermal annealing at 600°C in vacuum improved the crystallinity of the anatase phase and made the porous TiO_2 thin film preferentially (101)
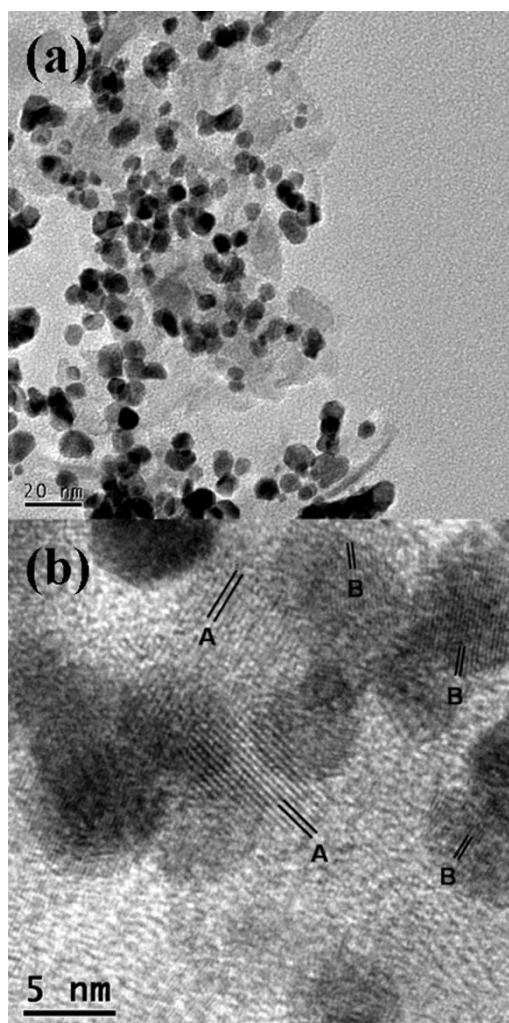
Figure 4-3 (a) TEM and (b) HRTEM images of Pt nanoparticles on the TiO$_2$-3h support. The lattice fringes labeled by A and B are due to the anatase (101) and the Pt(111) lattice planes, respectively.

oriented.   The better crystallinity of the anatase phase seemed to play an important role in improving the electrical conductivity of the porous TiO$_2$ thin film.   Pt nanoparticles could be easily electrodeposited on the TiO$_2$ thin film annealed at temperatures at 600°C, and electrochemical measurements could be performed without difficulty.   On the contrary, no electrochemical operation could be effectively conducted for samples annealed at temperatures below 500°C.

Figure 4-3(a) shows the bright-field TEM image of electrodeposited Pt nanoparticles on the Pt/TiO$_2$-3h electrode.   Nanoparticles with a dark contrast are the electrodeposited Pt catalyst, as revealed by the lattice fringe of the Pt(111) plane (~0.23 nm) in the high

resolution TEM (HRTEM) image shown in Fig. 4-3(b).   Also indexed in Fig. 4-3(b) is the

TiO_2 anatase (101) plane (~0.35 nm).   According to the TEM image, Pt nanoparticles with

a size distribution ranging from 4 to 7 nm adhered over the TiO_2 grain cluster.   The small

size and well dispersion of the Pt nanoparticles on the porous TiO_2 support can create a

large Pt surface, thereby resulting in a large electrochemically active surface area (ESA).

4.3 Electrochemical measurement

The ESA of the Pt catalyst was evaluated by the CO stripping CV measurement.

Figure 4-4 shows the CO stripping CV curves of the Pt/TiO_2-3h, Pt/TiO_2-tf, Pt/Ti and

blanket-Pt electrodes.   The ESA was determined by the following equation:

$$ESA = \frac{Q_{CO}}{[Pt] \times 0.484} \qquad\qquad (4\text{-}1)$$

where Q_{CO} ($mCcm^{-2}$) is the total charge involved in the electro-oxidation reaction of CO

adspecies, [Pt] is the mass loading per unit area of the Pt catalyst on the electrode and 0.484

represents the oxidation charge for a monolayer of CO adsorbed on a smooth Pt surface.

Q_{CO} was calculated by integrating the area of the CO oxidation peak in the first CO

stripping cycle.   The measured Pt loadings of the Pt/TiO_2-3h, Pt/TiO_2-tf, Pt/Ti and

blanket-Pt electrodes are 0.01697, 0.01095, 0.03774 and 0.06279 mg/cm^2, respectively.

The ESA of the Pt/TiO_2-3h electrode was thereby calculated to be 172.9 m^2g^{-1}, which was

much higher than that of Pt/TiO_2-tf, Pt/Ti and blanket-Pt electrodes (114.6, 26.3 and 57.1

m^2g^{-1}, respectively).   The much larger ESA of the Pt/TiO_2-3h electrode can significantly

improve electrocatalytic activity toward MOR compared to the other three electrodes.

Fig. 4-5 shows the MOR CV curves of the Pt/TiO_2-3h, Pt/TiO_2-tf, Pt/Ti and blanket-Pt

electrodes in the aqueous solution of 1 M CH_3OH and 1 M H_2SO_4.   Because of the larger

ESA, the Pt/TiO_x-3h electrode has a much higher MOR current density than the other three
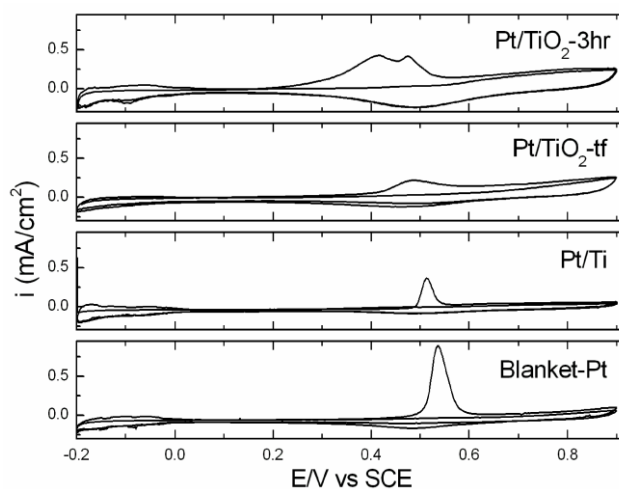
Figure 4-4 CO stripping cyclic voltammograms of the Pt/TiO$_2$-3h, Pt/TiO$_2$-tf, Pt/Ti and blanket-Pt electrodes in a CO saturated 0.5 M H$_2$SO$_4$ solution. The scan rate was 20 mV s^{-1}.

electrodes.   The methanol electro-oxidation peak of the Pt/TiO$_2$-3h electrode had the maximum around 0.58V with the onset potential at ~0.28 V, which is herein defined as the MOR potential at which the current density reaches 0.1 mA/cm^2.   For the Pt/TiO$_2$-tf, Pt/Ti and blanket-Pt electrodes, the CV curves had the anodic peak potential at 0.59 V, 0.62 V and 0.65 V with the onset potential at 0.40 V, 0.41 V and 0.48 V, respectively.   For MOR on the Pt catalyst in an acidic electrolyte, the anodic peaks in the forward scan and in the reverse scan of a CV measurement are associated with methanol oxidation and the removal of incompletely oxidized carbonaceous species, respectively.   During the reverse scan, residual linear Pt=C=O adspecies can be oxidized by Pt-OH$_{ads}$ in the acidic electrolyte within the potential range where the reverse anodic peak develops [34].   Therefore, the ratio of the anodic peak current density in the forward scan (I$_f$) to that in the reverse scan (I$_b$), (I$_f$/I$_b$), is a useful index for evaluating the CO tolerance of a MOR catalyst [59].   The I$_f$/I$_b$ ratios of the Pt/TiO$_2$-3h, Pt/TiO$_2$-tf, Pt/Ti and blanket-Pt electrodes were about 1.44, 1.21, 1.06 and 1.1, respectively.   The larger I$_f$/I$_b$ ratio of the Pt/TiO$_2$-3h electrode suggests that the electrode had a higher resistance against CO poisoning in MOR.   The improved CO tolerance of the Pt/TiO$_2$-3h electrode can play a key role in reducing the MOR
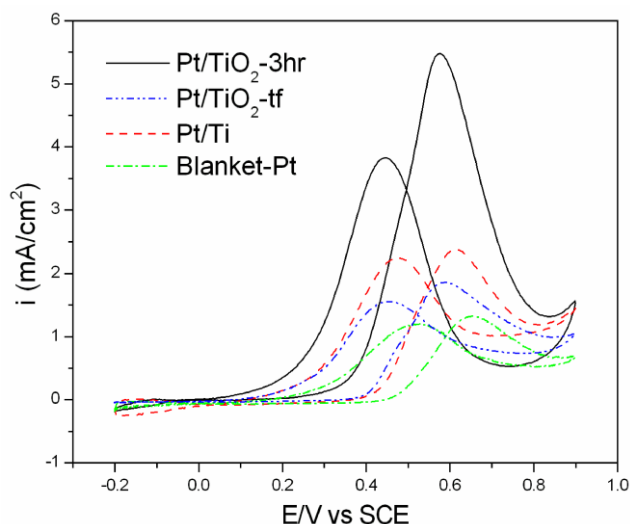
Figure 4-5 Cyclic voltammograms of the Pt/TiO$_2$-3h, Pt/TiO$_2$-tf, Pt/Ti and blanket-Pt electrodes in the 1 M CH$_3$OH + 1 M H$_2$SO$_4$ solution. The scan rate was 20 mV s^{-1}.

overpotential leading to the smaller onset and peak potentials observed in the CV measurement.

The CO stripping CV curves shown in Fig. 4-4 provide the direct evidence that the Pt/TiO$_2$-3h electrode had a much better CO tolerance in the acidic solution compared to the Pt/TiO$_2$-tf, Pt-Ti and blanket-Pt electrodes. The CV curve for CO stripping at the Pt/TiO$_2$-3hr electrode exhibited two distinct peaks at 0.42 V and 0.47 V vs. SCE with a gradual rising feature within the potential range between 0.2 and 0.4 V. For CO adspecies on Pt, two electro-oxidation peaks are usually detected within the potential range between 0.7 and 1.0 V vs. RHE [42, 46, 60]. The low potential peak was ascribed to CO electro-oxidation on the (110) plane or edge sites on the (111) plane, and the high potential peak was due to CO electro-oxidation on the (111) plane [42]. Thus the doublet peak measured in the study may be assigned to CO electro-oxidation on such surface sites as well. According to the TEM image of Fig. 4-3(a), many of Pt nanoparticles on the anatase support clearly show various polyhedron shapes. Nanocrystals with a polyhedral shape are usually enclosed mainly by {100} and {111} facets [61]. Therefore the (100) surface plane must also take part in the electrocatalytic reaction of CO oxidation. The

electrocatalytic activity of Pt toward CO oxidation varies with the Pt surface orientation, increasing in the order Pt(111) <Pt(110) <Pt(100) [62]. As a result, CO electro-oxidation on the Pt(100) surface will take place at a lower potential than on the (111) and (110) surfaces. It is likely that the CV signal due to CO electro-oxidation on (100) surface sites contributes to the rising feature on the low potential side of the doublet peak. Compared with the Pt/TiO$_2$-3h electrode, the Pt/TiO$_2$-tf electrode shows a featureless broad peak with the peak maximum at 0.49 V. Because both the Pt/TiO$_2$-tf and the Pt/TiO$_2$-3h electrodes have Pt catalysts electrodeposited on the TiO$_2$ surface, the difference in the CO electro-oxidation behavior between these two electrodes is very likely to result from differences in the particle size and shape of the Pt electrocatalysts and, possibly, the morphology of the TiO$_2$ supports. The Pt/Ti and the blanket-Pt film electrodes exhibit a single CO electro-oxidation peak at a much higher potential with the peak maximum at 0.52 V and 0.54 V, respectively. The single CO stripping peak indicates that the Pt catalyst on both electrodes had a surface crystallography greatly different from nanosized Pt particles on the porous TiO$_2$ support.

One other possible explanation for the slowly rising CV curve feature with the very low onset potential (~0.29V vs. SCE) is the repulsive interaction between CO adspecies on the Pt nanoparticles, which could weaken the bond strength of CO adspecies with the Pt lattice sites. The heat of adsorption of CO on Pt(hkl) surfaces is strongly coverage-dependent [63], and defects on nanoparticles have a significant impact on the local CO coverage [64]. As the coverage of the CO adspecies decreased due to the continuous CO oxidation process during the CV scan, the adsorption heat of CO adspecies on the Pt surface progressively increased because of the gradual decrease of the repulsive interaction. The CO oxidation potential thus shifted accordingly to the higher regime, leading to the appearance of the gradual rising feature within the potential range of 0.2 - 0.4 V.

The much better electrocatalytic performance of the Pt/TiO$_2$-3h electrode compared to the other three electrodes, such as the lower onset potential for both the CO electrooxidation and MOR, can be ascribed to the synergistic effect of the nanosized Pt catalyst and the TiO$_2$ support. There are two widely accepted models accounting for the enhancement of electrocatalytic activity of the supported Pt catalyst: the bifunctional mechanism [65-68] and the electronic effect (or ligand effect) [47, 55, 69-71]. TiO$_2$ can not only promote CO tolerance via the bifunctional mechanism, but may also modify the electronic structure of Pt nanoparticles in terms of the electronic effect. The bifunctional mechanism is widely used to describe how hydroxyl surface groups can oxidize and remove adjacent CO adspecies from the Pt catalyst surface, thus avoiding CO poisoning. For TiO$_2$ supported Pt nanoparticles, CO adspecies bound on the periphery of Pt nanoparticles can be readily oxidized via the bifunctional mechanism by neighboring Ti-OH groups, which may result from dissociative adsorption of water molecules on the TiO$_2$ surface. Theoretical studies have shown that spontaneous dissociative adsorption of water molecules effectively proceeds on the (001) surface of titania, whereas molecular adsorption prevails on the (101) surface [72-74]. Because the crystallite shape of anatase TiO$_2$ was a truncated bipyramid exposing both the (101) and (001) surfaces [74], it is likely that the porous TiO$_2$ support may provide a large quantity of (001) surface planes when the size of anatase grains on the support is close to the nanometer scale. Thus dissociative H$_2$O adsorption on the (001) anatase surface will create abundant Ti-OH surface groups on the TiO$_2$ support in the electrolyte, thereby promoting CO electro-oxidation on the Pt catalyst via the bifunctional mechanism. CO electro-oxidation via the bifunctional mechanism is likely more pronounced on the periphery of Pt nanoparticles due to the immediate contact of CO adspecies with Ti-OH groups surrounding the Pt nanoparticles.

An additional likely explanation for the better CO tolerance of the Pt/TiO$_2$-3h electrode is that chemisorption properties of noble metals can be significantly altered by

interactions with the TiO$_2$ surface [47, 55, 75]. The strong hypo–hyper-d-electron interaction between the TiO$_2$ support and Pt nanoparticles may greatly modify the electronic structure of Pt atoms at the interface. As a consequence, the catalytic activity of CO oxidation on Pt surface may be improved if modification of the adsorption strength of CO adspecies can accordingly reduce the activation barrier for the CO oxidation reaction. This is particularly true for Pt surface atoms situated in the peripheral region of Pt nanoparticles, which may be only a few atoms in width, because they directly bond to the TiO$_2$ support and act as the catalytic surface sites. The peripheral Pt atoms are more liable to the electronic effect than those surface atoms sitting apart from the periphery, and therefore should exhibit distinct electrocatalytic activity toward CO oxidation. As the size of Pt nanoparticles become smaller, the number of peripheral Pt sites will increase resulting in an electrocatalytic activity more characteristic for CO oxidation on the peripheral sites. On the other hand, Pt particles with a larger particle size have a lower electrocatalytic activity possibly due to the less effective electronic effect [76]. Moreover, diffusivity of adspecies on Pt particles subject to the strong electronic interaction with the support may be significantly modified. Hepel et al. recently reported that the CO surface diffusivity on the Pt nanoparticle can be improved due to the weakened CO adsorption strength on Pt nanoparticles supported on TiO$_2$ nanotubes [77]. Because of the nanoscaled size ($<$ 5 nm) of Pt catalyst particles on the porous TiO$_2$ support, CO and/or OH adspecies can readily diffuse over the Pt nanoparticle, thereby facilitating a better efficiency of CO oxidation via the Langmuir–Hinshelwood reaction mechanism, in which adsorbed reactants diffuse, collide and form products on the surface. The above discussion can explain the difference in the MOR electroactivity between the Pt/TiO$_2$-3h and the Pt/TiO$_2$-tf electrodes.

For better understanding of the above described synergistic effect of the Pt nanoparticles and the TiO$_2$ support, Fig. 4-6 schematically illustrates the likely reaction steps of CO oxidation on the Pt nanoparticle, which can be described by the following
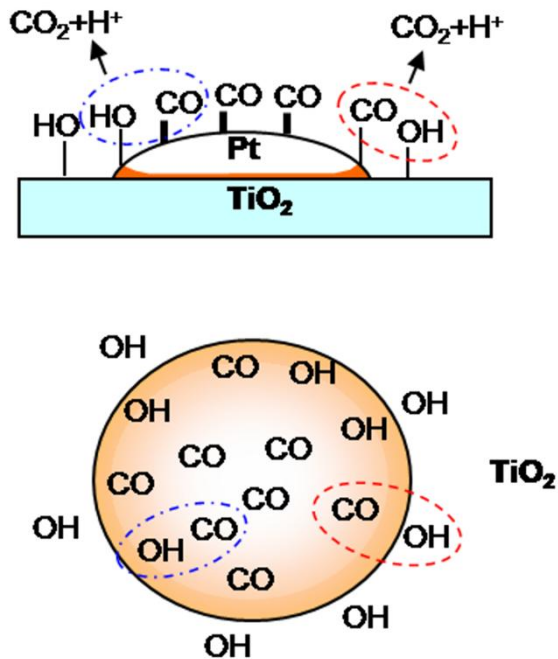
Figure 4-6 Schematic illustrating the synergistic effect of the Pt nanoparticle and the anatase TiO_2 support on CO oxidation on the Pt nanoparticle.

reaction equations:

$$TiO_2 + H_2O \rightarrow TiO_2\text{–}OH + H^+ + e^-, \tag{4-2}$$

$$TiO_2\text{–}OH + Pt\text{–}CO \rightarrow CO_2 + Pt + TiO_2 + H^+ + e^-, \tag{4-3}$$

$$Pt + H_2O \rightarrow Pt\text{–}OH + H^+ + e^-, \tag{4-4}$$

$$Pt\text{–}CO + Pt\text{–}OH \rightarrow 2Pt + CO_2 + H^+ + e^-. \tag{4-5}$$
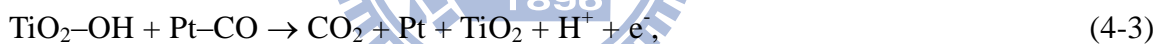
The Pt catalyst is illustrated in the figure as a hemispherical particle for clarity. The interface area in the Pt nanoparticle is shaded to indicate the strong electronic interaction between Pt and the TiO_2 support. Dissociative adsorption of water molecules on the TiO_2 support creates TiO_2–OH surface groups. TiO_2–OH groups adjacent to Pt nanoparticles may readily oxidize CO groups bonded on the peripheral Pt atoms, of which the electronic structure is greatly modified by the TiO_2 support. Once a free Pt site is created by the CO oxidation reaction, an OH surface group can then be adsorbed on the free Pt site by dissociative adsorption of an H_2O molecule or OH adspecies migration from other Pt sites or the TiO_2 surface. The OH surface group can then oxidize a CO group sitting on a
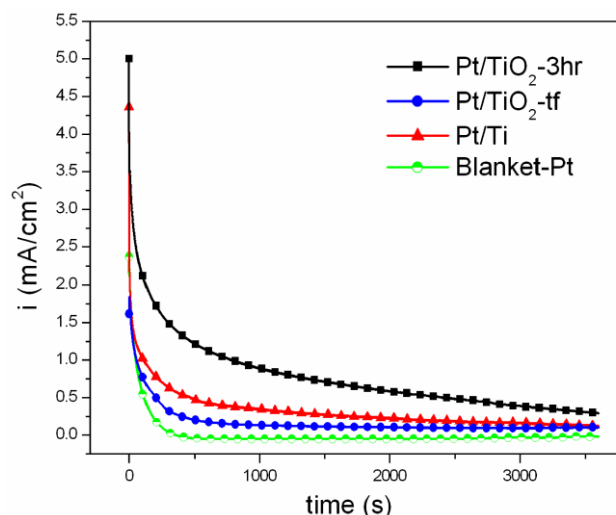
Figure 4-7 Chronoamperometry curves of the Pt/TiO$_2$-3h, Pt/TiO$_2$-tf, Pt/Ti and blanket-Pt electrodes in the solution of 1 M CH$_3$OH +1 M H$_2$SO$_4$ at room temperature (~25 ^{o}C) for one hour.   The oxidation potential was kept at 0.5 V vs. SCE.

neighboring Pt site, creating two free Pt sites, and the CO oxidation reaction will continue if any Pt-CO group is present on the reaction front.   Because the reaction rate increases with the density of available Pt sites, the electrocatalytic activity toward CO oxidation will become more and more thriving till the coverage of CO adspecies is significantly diminished.

Fig. 4-7 shows the chronoamperograms of the electroactivity of the Pt/TiO$_2$-3h, Pt/TiO$_2$-tf, Pt/Ti and blanket-Pt electrodes at the oxidation potential of 0.5 V in the 1 M CH$_3$OH/ 1 M H$_2$SO$_4$ aqueous solution at 25°C.   All the four electrodes showed a decay in the MOR electroactivity with time.   This is most obvious for the blanket-Pt, which had a rapid drop in the current density to 0.04 mA/cm^{-2} within the first 500 sec.   On the other hand, the Pt/TiO$_2$-3h electrode shows a moderate current density decay and has a much higher electrocatalytic activity as compared to the other three electrodes.   The Pt/TiO$_2$-3h electrode still keeps a current density of ~0.3 mA/cm^{-2} after one hour of methanol oxidation in the acidic solution.   The higher electroactivity stability of the Pt/TiO$_2$-3h electrode may be attributed to the large ESA and the enhanced CO tolerance.   CO adspecies could be

effectively oxidized and removed from the Pt catalyst nanoparticles so that the catalytic oxidation of methanol proceeded more efficiently on the Pt/TiO$_2$-3h electrode.

4.4 Summary

The study prepared porous TiO$_2$ thin film on the Si substrate by hydrothermal method for the use of the Pt catalyst support for MOR electroactivity study. The porous TiO$_2$ support was mainly composed of anatase phase after vacuum annealing at 600°C and showed an electrical conductivity good for Pt electroplating and electrochemical measurement. Because of the porous structure of the TiO$_2$ support and well dispersed Pt nanoparticles, the Pt/TiO$_2$-3h electrode had a much larger ESA compared to the Pt/TiO$_2$-tf, Pt/Ti and the blanket-Pt electrodes. MOR CV and CO stripping measurements indicated that the Pt/TiO$_2$-3h electrode had a high electrocatalytic activity toward MOR and a very good CO tolerance. We ascribe the good CO tolerance to the synergistic effect of Pt nanoparticles and the porous TiO$_2$ support. The nanosized scale of the Pt catalyst allows easy access of CO adspecies by hydroxyl surface groups on the TiO$_2$ surface, thereby CO electro-oxidation prevails around the peripheral area of Pt nanoparticles via bifunctional mechanism. Moreover, the strong electronic interaction between the Pt nanoparticle and the TiO$_2$ substrate might weaken the chemisorption strength of CO adspecies on the Pt catalyst, and thus enhance CO electro-oxidation activity.

Chapter 5 Electrocatalytic oxidation of methanol on Pt nanoparticles loaded on a PdO nanoflake thin film in acidic solution

5.1 Introduction

In this study, we prepared PdO nanostructured thin films by reactive sputter deposition as the Pt catalyst support, and investigated their influence on the electrocatalytic performance of Pt nanoparticles for MOR in acidic media.

Although study on electrochemical properties of PdO is rarely reported in the literature [78-79], the electrochemical behavior of metallic Pd has been extensively documented [80-89]. Electrochemical properties of PdO can be well interpreted in terms of the cyclic voltamperometry (CV) of metallic Pd because the Pd/PdO redox reaction is the primary electrochemical process in the CV test of Pd electrodes. Pd exhibits a high electrocatalytic activity toward MOR and, therefore, has been considered a possible catalyst replacement for Pt in MOR. However, the study on the electrocatalytic performance of Pd electrode toward MOR was mostly performed in alkaline solutions. This is because that Pd has a much higher dissolution rate than Pt in acidic electrolytes [90-91] . Anodic dissolution of the Pd electrode can occur in acidic media if repetitive Pd oxide formation and reduction take place on the anode during a CV test [43, 92-93]. As a consequence, only a very few reports on MOR catalyzed by Pd-based anodes in acidic media are available in the literature [80, 94-95]. The PdO thin film prepared in this study exhibits a CV behavior similar to the metallic Pd electrode in acidic solution, and the electrochemical response of the PdO electrode is predominantly determined by the metallic Pd layer. We also pulse-electrodeposited Pt nanoparticles on the PdO electrode (denoted by Pt/PdO), and found that the PdO support could enhance the electrocatalytic activity of the Pd

nanoparticles toward MOR in the acidic solution.

5.2 Electrochemical study of the PdO nanoflake thin film

Figure 5-1(a) shows the SEM image of as-deposited PdO nanoflakes on a carbon fiber selected from the carbon cloth shown in the inset. The uniform PdO thin film sputter-deposited on the carbon cloth is composed of continuously interconnected flake-like nanostructures as shown by the magnified SEM image in Fig. 5-1(b). The PdO nanoflakes are very thin with a thickness of ~15-20 nm according to the SEM image, and XRD analysis (not shown) indicates that the room-temperature deposited PdO thin film is amorphous. The nanoflake-like morphology of the as-deposited PdO thin film results in a large surface area, providing enormous electrochemical active sites. Since PdO is a p-type semiconductor and has a low electric resistivity, the PdO nanoflake thin film imposes little
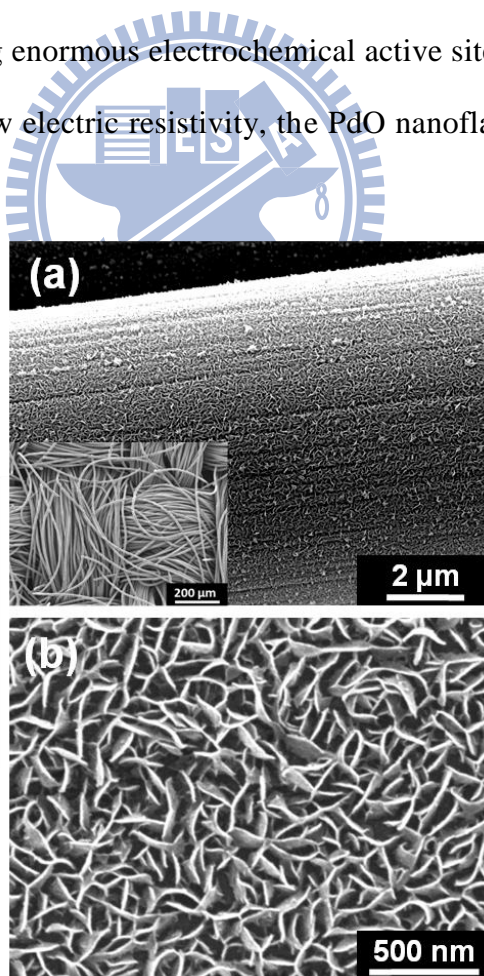
Figure 5-1 SEM images of (a) the as-deposited PdO nanoflakes on a carbon fiber selected from the carbon cloth shown in the inset; (b) a magnified SEM image of PdO nanoflakes deposited on the carbon fiber.
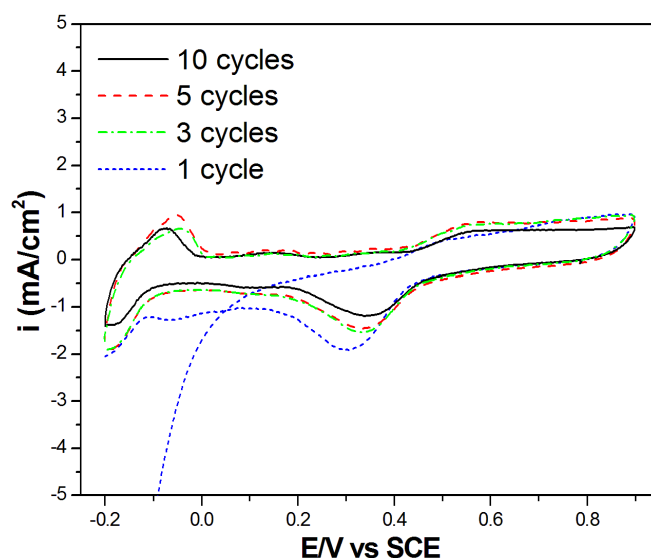
Figure 5-2 The Cyclic voltammogram of the PdO nanoflake thin film in the aqueous solution of 0.5 M H_2SO_4. The scan rate was 20 mV s^{-1}.

difficulty in the electrochemical measurement and the electrodeposition of Pt nanoparticles.

To study the electrocatalytic activity of the PdO nanoflake thin film toward MOR in acidic media, we first performed CV measurements for the thin film in an aqueous solution of 0.5 M H_2SO_4, and the CV result is presented in Fig. 5-2.   The CV measurement has a scan potential range between -0.2 − 0.9 V vs. SCE with the scan rate at 20 mV s^{-1}.   The cyclic voltammogram shows that, after the first cycle scan, the PdO thin film exhibits a CV behavior characteristic for metallic Pd.   To examine if metallic Pd was electrochemically formed on the PdO nanoflake thin film in the acidic solution, we studied chemical states present on the PdO thin film by XPS.   Figure 5-3 shows Pd 3d XPS spectra of the PdO thin film before and after the CV measurement.   The dashed lines in the figure mark the binding energies of the Pd(0), Pd(II) and Pd(IV) states, which are referred to the literature [96-98].   The as-deposited nanoflake thin film has the Pd $3d_{5/2}$ peak maximum at 336.5 eV, suggesting that the PdO and/or Pd(OH)$_2$ is the primary chemical states on the film surface. Because the Pd 3d doublet has a very broad peak width, PdO_2 is likely also present in the as-deposited film.   When the PdO thin film is polarized at 0.1 V in the 0.5 M H_2SO_4

solution for 30 min, the film surface is reduced to the metallic Pd state as shown by the dramatic change in the shape of the Pd 3d peak profile, which has a clear signal component situated at 335.2 eV. After the first cycle of the CV scan, the Pd $3d_{3/2}$ peak is narrowed with the peak maximum at 335.2 eV, indicating that the PdO thin film is extensively reduced. The reduced thin film has the Pd 3d doublet peak intensity slightly higher on the high binding energy side than a metallic Pd thin film, which was sputter-deposited on the carbon cloth for comparison; this suggests that the PdO and $Pd(OH)_2$ states still contribute Pd 3d signal to the XPS spectrum of the reduced PdO electrode. Because of the detection of the Pd(II) state, the metallic Pd surface layer electrochemically formed on the PdO thin film has a thickness less than the probe depth of the Pd 3d photoelectron, which is about 5 nm when the Mg K_α line is used as the x-ray excitation source. As a consequence, the metallic Pd surface layer must decisively govern the CV behavior of the PdO nanoflake thin film after the first CV cycle.

Palladium has CV responses in acidic media similar to Pt [43, 80, 99]. In a cyclic voltammogram of metallic Pd in the H_2SO_4 solution, three pairs of CV peaks at potentials below 0.9 V are observed; the three peak pairs are associated with three redox reactions: hydrogen adsorption/desorption, hydrogen absorption/evolution and Pd oxidation/ PdO reduction. The anodic and cathodic peaks below 0 V vs. SCE are due to hydrogen desorption and adsorption reactions, respectively, on metallic Pd. Metallic Pd has a great hydrogen absorption capability; the cathodic and anodic peaks due to the hydrogen absorption/evolution reactions may span a large potential range (-0.1− 0.3 V vs. SCE) depending on the thickness of the metallic Pd layer, and overlap the peaks due to hydrogen adsorption/desorption reactions [100-102]. However, because the metallic Pd surface layer formed on the PdO nanoflake electrode is very thin as discussed above, the hydrogen absorption/evolution reactions must have a very small contribution to the CV peaks at potentials below 0.02 V. The anodic wave beginning around 0.45 V results from the
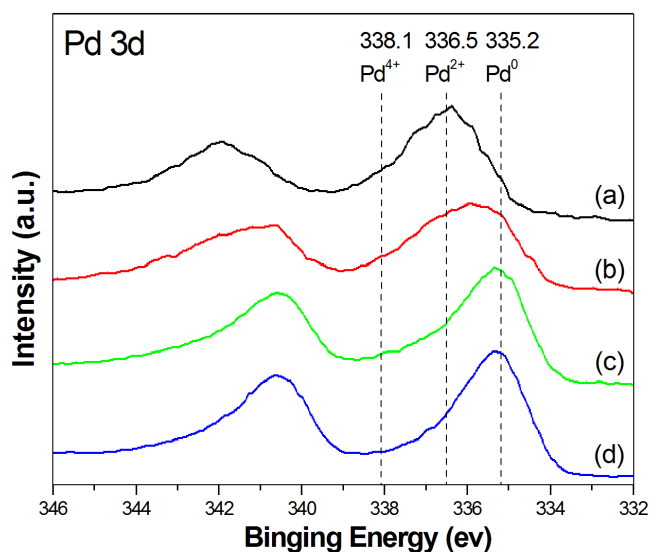
Figure 5-3 Pd (3d) XPS spectra of the PdO nanoflake thin film: (a) the as-deposited PdO thin film; (b) the PdO thin film polarized at 0.1 V for 30 min in the 0.5 M H₂SO₄ solution; (c) the PdO thin film after one CV scan cycle; and (d) a metallic Pd thin film deposited on the carbon cloth and cleaned with Ar sputtering for 400 sec. The dashed lines mark the binding energies of the Pd(0), Pd(II) and Pd(IV) states, which are referred to the literature.

oxidation of metallic Pd during the positive sweep. Since the CV scan limit (0.9 V vs. SCE) is far below the potential required for the formation of PdO_2 (1.4 V) [43, 93, 103], the Pd(II) state must be the primary oxidation state on the PdO thin film in the potential range between 0.45 and 0.9 V. Electro-oxidation of metal Pd in acidic media is proposed to proceed via the following reactions [43, 93, 98]:

$$Pd + H_2O \rightarrow PdO + 2H^+ + 2e^- \tag{5-1}$$

$$Pd + 2H_2O \rightarrow Pd(OH)_2 + 2H^+ + 2e^- \tag{5-2}$$

The cathodic peak between 0.15−0.45 V in the reverse sweep is due to the reduction of the surface oxide and hydroxide, which are electrochemically formed during the preceding positive sweep. As to be discussed later, the presence of the hydroxide adspecies is important to the enhancement in the electrocatalytic activity of Pt nanoparticles toward MOR, which were electrodeposited on the PdO thin film.
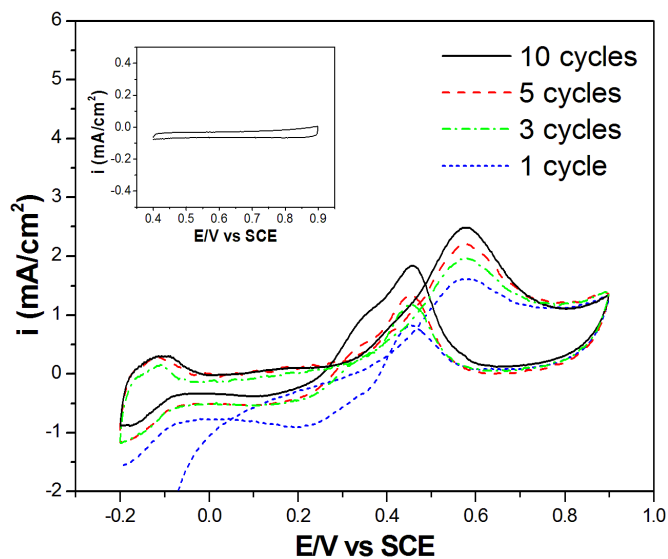
Figure 5-4 The cyclic voltammogram of the PdO thin film in the aqueous solution of 1 M CH$_3$OH + 0.5 M H$_2$SO$_4$. The inset shows a CV curve with a scan range of 0.4 – 0.9 V at the tenth scan cycle. The scan rate was 20 mV s^{-1}.

Previous study shows that Pd has an electrocatalytic behavior similar to Pt for electro-oxidation of methanol, ethanol and formic acid in acidic or alkaline media [104-106]. Figure 5-4 shows a cyclic voltammogram of the PdO thin film in an aqueous solution of 1 M CH$_3$OH + 0.5 M H$_2$SO$_4$. After the first scan cycle, the CV profile of the PdO thin film is similar to that of a Pt electrode. We have performed a CV measurement in the potential range between 0.4 – 0.9 V, where PdO reduction is unimportant, and the result shown in the inset of Fig. 5-4 indicates that PdO has little electrocatalytic activity toward MOR. Therefore the anodic peak situated at 0.58 V is due to MOR on the metallic Pd electrode only. Metal Pd sites are produced on the nanoflake thin film as a result of the PdO reduction during the potential sweep from -0.2 to 0.45 V. Methanol chemisorption may then take place on these metal Pd sites, and MOR starts around 0.33 V. The MOR current density increases with the CV cycle number, indicating that the repetitive PdO reduction and Pd oxidation during the CV scan increase Pd electrocatalytic sites on the PdO

57

thin film. The MOR current density increases by a factor of 1.54 after 10 cycles of the CV scan compared with the first CV cycle.
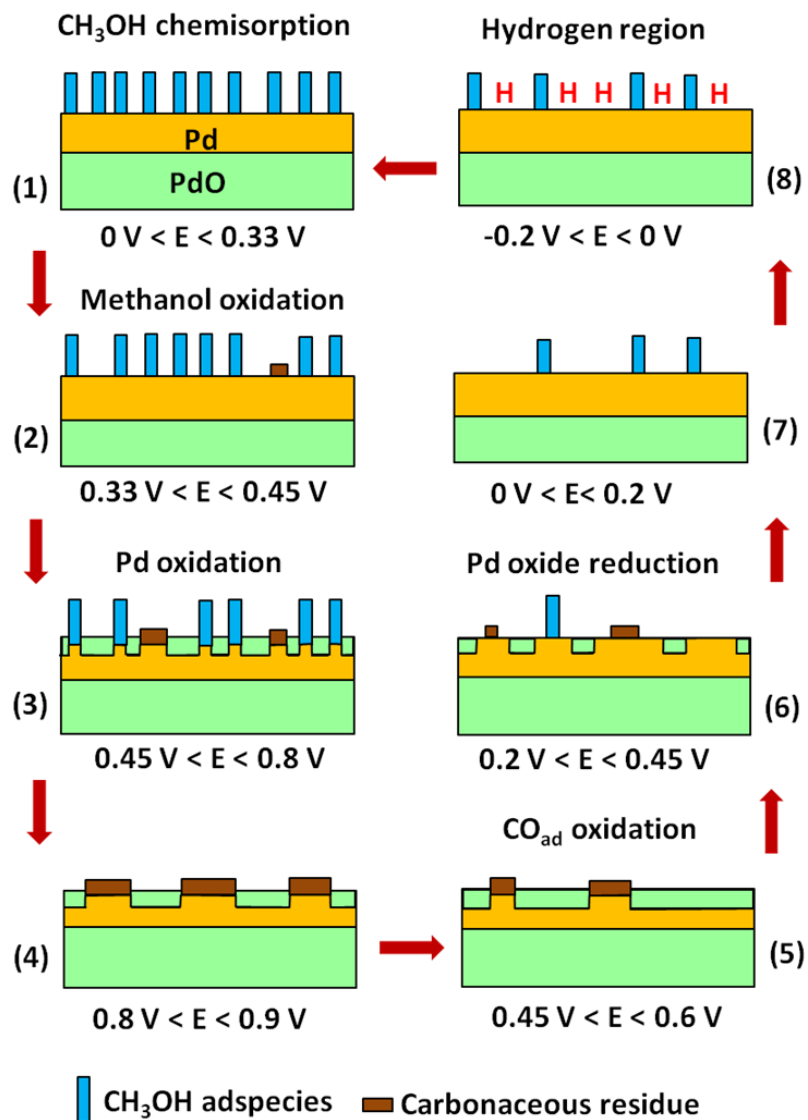
Figure 5-5 Schematic illustration of the electrochemical reaction steps for the PdO thin film in the aqueous solution of 1 M CH_3OH + 0.5 M H_2SO_4; (1) formation of a metallic Pd surface layer on the PdO thin film at potentials below 0.33 V; (2) electro-oxidation of chemisorbed methanol starts around 0.33V accompanied with carbonaceous residue formation; (3) free Pd sites are oxidized at potentials above 0.45 V; (4) the MOR on the PdO thin film is completed at 0.8 V; (5) the carbonaceous adspecies are oxidized at potentials below 0.6 V in the reverse CV sweep; (6) the PdO reduction begins at ~0.45 V; (7) more methanol molecules are chemisorbed on the electrode; (8) hydrogen adsorption and desorption take place at potentials below 0 V. The dimension of the block representing the carbon residue denotes the amount of the poisoned sites.

In the reverse sweep, an anodic peak starts at 0.65 V with the peak maximum at 0.46 V. For Pt electrodes, the anodic peak in the reverse sweep is generally ascribed to oxidation of carbonaceous adspecies, which are incompletely oxidized intermediates formed in the forward sweep [20, 34, 39, 107]. However, some previous studies proposed that the anodic peak in the reverse scan resulted from methanol oxidation on metal Pt sites, which were reactivated during the reverse sweep from the upper limit potential of the CV scan [88, 108-109]. Because the PdO electrode has little electrocatalytic activity toward MOR between 0.4 − 0.9 V as discussed above, the large anodic current density measured in the potential range of 0.4 − 0.65 V (in the reverse sweep) is unlikely due to methanol oxidation on reactivated metal Pd sites, which should be absent on the PdO electrode at potentials above 0.45 V in the acidic solution. Therefore, we believe that the anodic peak in the reverse CV sweep is a result of oxidation of carbonaceous adspecies on the PdO electrode. Accompanied with the anodic peak is a shoulder peak with an obvious peak maximum around 0.33 V, which is close to the peak potential of the PdO reduction (Fig. 5-2). Note that the MOR anodic peak has a shoulder feature as well; the shoulder peak is especially obvious for the tenth CV cycle. The MOR shoulder peak is situated around 0.45 V, which is around the onset potential of the Pd oxidation on the nanoflake thin film. Therefore the observation of the shoulder features for both the forward and the reverse anodic peaks is likely correlated with the Pd/ PdO redox reaction on the PdO electrode in the acidic solution.

For clarity, we schematically summarize in Fig.5-5 the electrochemical reaction steps for the PdO thin film in the aqueous solution of 1 M CH_3OH and 0.5 M H_2SO_4. First, a metallic Pd surface layer is formed on the nanoflake thin film after repetitive CV scans as a result of the PdO reduction at potentials below 0.45 V vs. SCE (step 1). The Pd surface layer has a thickness smaller than 5 nm. Like on a Pt catalyst, dissociative chemisorption of methanol may occur on the metallic Pd surface layer before the onset potential of MOR.

When the electro-oxidation of chemisorbed methanol starts around 0.33V, some metal Pd sites become free from methanol adspecies and some sites may be blocked by carbonaceous residues due to incompletely oxidized MOR intermediates (step 2). The carbonaceous residues are likely CO adspecies with the linear (i.e., atop) and bridge adsorption structures [110-112]. Free Pd sites are oxidized at potentials above 0.45 V (step 3), and the thus formed PdO and/or Pd(OH)$_2$ may modify the electronic and chemical structures of neighboring metal Pd sites that are still occupied by methanol adspecies. The modifications may improve the electrocatalytic activity of Pd toward MOR via the electronic effect and the bi-functional mechanism [20, 23]. The change in the MOR activity is likely the cause resulting in the shoulder on the low potential side of the anodic MOR peak. The MOR on the nanoflake thin film is completed at 0.8 V, and metal Pd sites on the electrode surface are either oxidized or covered by carbonaceous residues (step 4), which can be oxidized at potentials below 0.6 V in the reverse CV sweep (step 5). Because the PdO reduction is suppressed on the nanoflake thin film at potentials above 0.45 V, free Pd sites created as a result of the oxidation of carbonaceous residues will be immediately oxidized in the potential range of 0.45 - 0.6 V. When PdO reduction begins at ~0.45 V, free metal Pd sites are produced (step 6). The chemical phase transition from PdO to metal Pd on the electrode surface may modify the chemical and electronic structure of the area surrounding carbonaceous adspecies, and thus alter the electro-oxidation rate of the carbonaceous adspecies. Moreover, free metal Pd sites can facilitate the transformation of a neighboring atop-CO adspecies to a bridge-CO adspecies, which has been proposed to be an important reaction step for the CO electro-oxidation on Pt electrodes [113], resulting in an improved CO removal rate on the PdO electrode. Therefore, the formation of free Pd sites due to the PdO reduction is a probable cause of the development of the shoulder near the reduction peak potential (0.33 V in Fig. 5-2). The free Pd sites also allow the dissociative chemisorption of methanol on the PdO electrode in

the potential range of step 6. More methanol molecules can be chemisorbed on the electrode in the potential range between 0 V and 0.2 V, in which surface oxides are completely removed (step 7). Hydrogen adsorption is activated on Pd sites that are unoccupied by methanol adspecies at potentials below 0 V (step 8), and hydrogen adatoms are desorbed when the CV scan is reversed to the forward direction.

5.3 Electrocatalytic activity of the Pt/PdO electrode toward MOR

Figure 5-6(a) shows the SEM image of the PdO thin film after the pulse-electrodeposition of Pt nanoparticles. The Pt nanoparticle-loaded PdO thin film has a flake shape less distinct than the as-deposited PdO thin film shown in Fig. 5-1 because of the accumulation of Pt nanoparticles on the ridge of the nanoflake. The XRD spectrum of
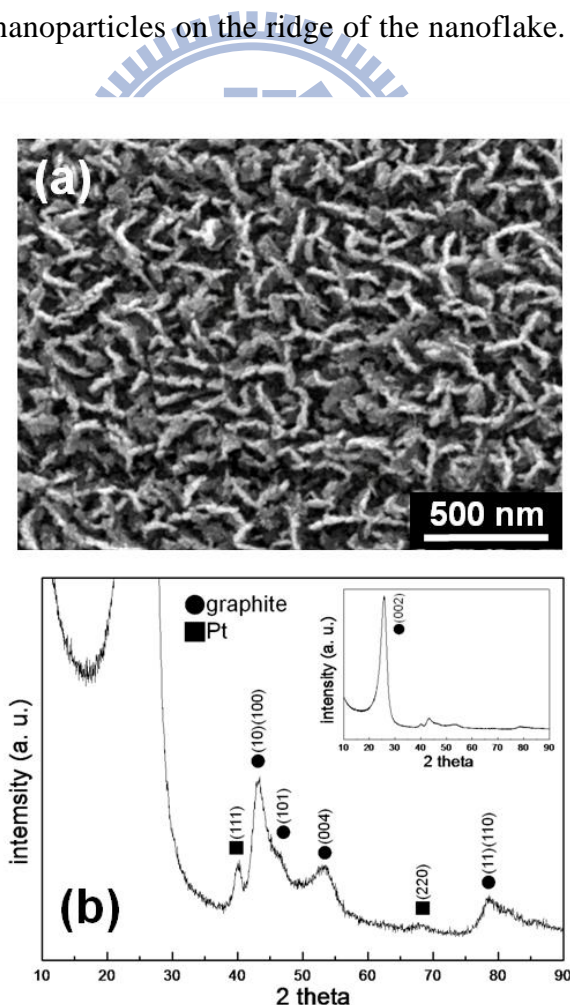
Figure 5-6 SEM image of the PdO thin film after the pulse-electrodeposition of Pt nanoparticles; (b) XRD spectrum of the Pt/PdO thin film shown in (a).
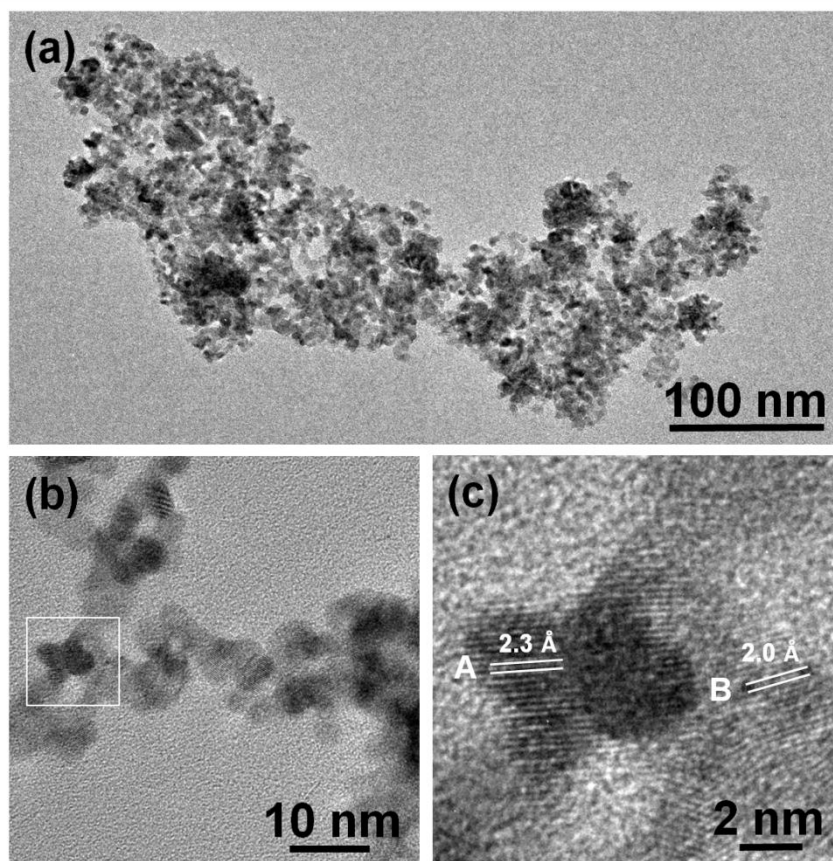
Figure 5-7 (a) The bright field TEM image of electrodeposited Pt nanoparticles on PdO nanoflakes separated from the Pt/PdO electrode; (b) and (c) HRTEM images of a selected area on the edge of a nanoflake.

the Pt/PdO thin film is shown in Fig. 5-6(b). The two diffraction peaks situated at 40.2°

and 68.3° correspond to the Pt (111) and the (220) lattice planes, respectively. The other

diffraction peaks shown in the XRD spectrum are due to the hexagonal lattice structure of

graphite [114]. The average particle size of Pt nanoparticles on the PdO nanoflakes thin

film is 5.5 nm according to the Debye-Scherrer calculation based on the peak width of the

Pt (111) diffraction peak [32, 105].

Figure 5-7(a) shows the bright field TEM image of electrodeposited Pt nanoparticles

on several PdO nanoflakes, which were separated from the Pt/PdO electrode by ultrasonic

agitation in the ethanol solution. The PdO nanoflakes are decorated with dense spots of

dark contrast. The high resolution TEM (HRTEM) images of a selected area on the edge
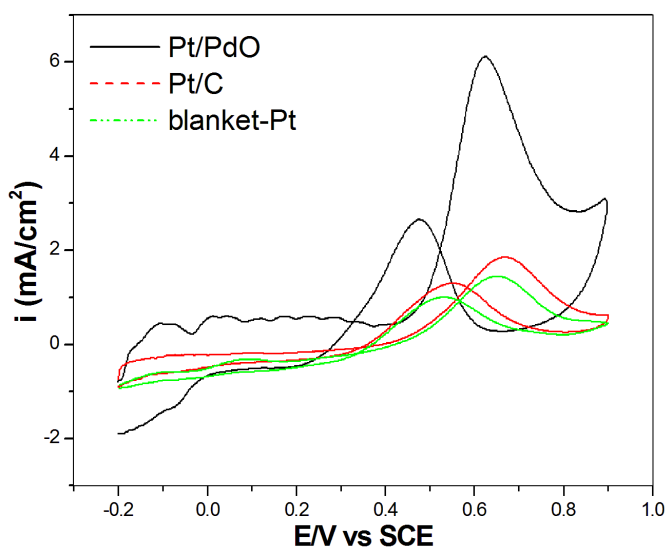
Figure 5-8 Cyclic voltammograms of the Pt/PdO, the Pt/C and the blanket-Pt electrodes in the aqueous solution of 1 M CH_3OH + 0.5 M H_2SO_4.   The CV curves shown in the figure are for the fourth CV cycle. The scan rate was 20 mV s^{-1}.

of a nanoflake (Figs. 5-7(b) and (c)) indicate that the dark spots are due to Pt nanocrystals; the two lattice spacings labelled by A and B correspond to the Pt (111) and (200) lattice planes, respectively.   The size of most Pt nanoparticles is in the range between 3.0 and 5.5 nm, which is reasonably in agreement with the average size derived from the XRD analysis. The Pt nanoparticles uniformly spread over the PdO nanoflake although particle aggregation occurs in some areas.   Because of the nanoscale size and the good dispersion of Pt nanoparticles on the PdO nanoflake, a large amount of surface Pt atoms must be located in the border area with the PdO substrate.   As a consequence, numerous Pt electrochemical active sites are subject to strong local chemical and electronic modifications induced by the PdO substrate.   These modifications may greatly influence the electrocatalytic activity of the Pt nanoparticles toward MOR.

The cyclic voltammogram of the Pt/PdO electrode in the aqueous solution of 1 M CH_3OH and 0.5 M H_2SO_4 is shown in Fig. 5-8.   For comparison, the figure also presents the CV curves of an electron-beam deposited Pt thin film and electrodeposited Pt particles;

Table 5-1 The onset and peak potentials of the CO electro-oxidation reaction on the Pt/PdO, the Pt/C, the blanket-Pt and the PdO electrodes.   The electrochemical active surface area (ESA) derived from the CO stripping cyclic voltammograms is also listed.

	Pt/PdO	Pt/C	Blanket-Pt	PdO nanoflakes
Onset potential (V)	0.49	0.52	0.52	0.59
Onset potential (V)	0.55	0.58	0.63	0.67
ESA (cm^2/mg)	189.6	82.2	52.2	

both types of the Pt electrocatalyst were deposited directly on the carbon cloth, and we will refer to the Pt thin film and the Pt particle electrodes as blanket-Pt and Pt/C, respectively. The MOR peak of the Pt/PdO electrode has the peak maximum around 0.62 V with the onset potential at 0.45 V.   The Pt/PdO electrode has both the MOR peak potential and the onset potential less positive than the Pt/C and the blanket-Pt electrodes, indicating that the Pt/PdO electrode has a lower overpotential for methanol electro-oxidation.   Moreover, the Pt/PdO electrode has a much larger intensity ratio of the MOR peak (denoted by I_f) to the anodic peak in the reverse scan (denoted by I_b) than the other two electrodes.   The I_f/I_b ratio of the Pt/PdO electrode is 1.87, and the ratio for the Pt/C and the blanket-Pt electrodes is 1.28 and 1.22, respectively.   We may use the I_f/I_b ratio as an index to describe the resistance of the electrocatalyst against the CO poisoning in MOR.   The large I_f/I_b ratio of the Pt/PdO electrode indicates that Pt nanoparticles on the PdO support have a higher CO tolerance.   The efficient removal of CO adspecies is crucial for improving the electrochemical performance in DMFCs.   To examine the CO tolerance of the Pt/PdO electrode, we performed the CO stripping measurement for the electrode and the result is presented in Fig. 5-9.   Also shown in the figure are the CO stripping CV voltammograms for the Pt/C, the blanket Pt and the PdO thin film electrodes.   The onset and the peak potentials of the CO stripping peak are listed in Table 1.   The Pt/PdO electrode has the CO oxidation peak potential smaller than the PdO nanoflake electrode by 0.12 V; this large
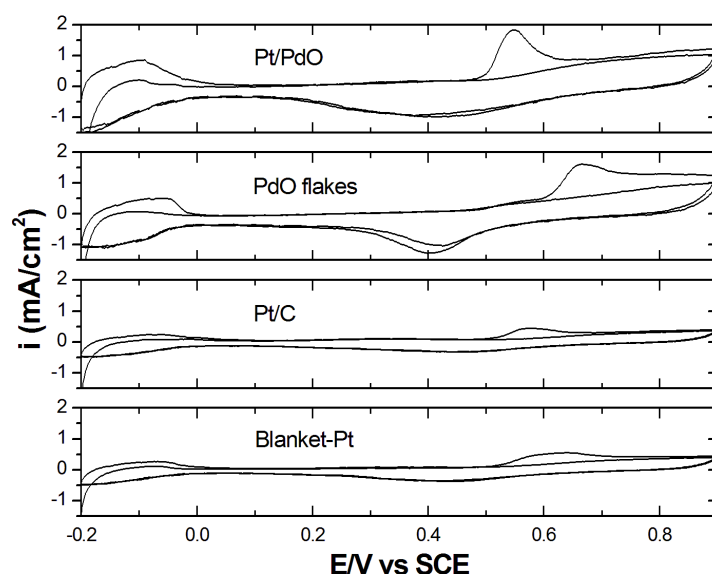
Figure 5-9 CO stripping CV curves for the Pt/PdO, the PdO thin film, the Pt/C and the blanket Pt electrodes. The scan rate was 20 mV s^{-1}.

potential difference suggests that the CO stripping peak of the Pt/PdO electrode has little contribution directly from the metal Pd sites, which are created on the PdO support at the polarization potential (0.1 V) for the CO adsorption treatment. The Pt/PdO electrode has the CO stripping peak potential and the onset potential smaller than the Pt/C and the blanket-Pt electrodes, indicating that CO adspecies on the Pt/PdO electrode are easier to be removed from Pt electrocatalytic sites.

The electrochemical surface area (ESA) of a Pt based catalyst is often determined by the total charge in the hydrogen adsorption (or desorption) region in a CV voltammogram. However, metal Pd has a great capacity of hydrogen absorption, the ESA of the Pt catalyst on the PdO support will be overestimated if the hydrogen region is used to calculate the ESA. We thus used the CO stripping peak to estimate the ESA of the Pt/PdO, the Pt/C and the blanket Pt electrodes by the following equation:

$$ESA = \frac{Q_{CO}}{0.484 \times M_{Pt}} \tag{5-3}$$

where Q_{CO} (in mC) is the total charge calculated from the CO stripping peak, and M_{Pt} represents the mass loading (mg) of the Pt catalyst on the electrode. The value, 0.484 (mC cm^{-2}), corresponds to the charge density required for the electro-oxidation of one monolayer of CO adspecies on the Pt surface [115]. The calculated ESA values of the three Pt-based electrodes are also listed in Table 1. The Pt/PdO electrode has an ESA of 189.6 cm^2/mg, which is much larger than the ESA of the other two electrodes. The large ESA of the Pt/PdO electrode is ascribed to the enormous surface area of the PdO nanoflake support and the good dispersion of Pt nanoparticles on the support. Because of the large ESA, the Pt/PdO electrode exhibits a very high electrocatalytic activity toward MOR as shown in the CV voltammogram of Fig. 5-8.

Compared with the two electrodes without the PdO support, the Pt/PdO electrode has a low overpotential for MOR and a high CO tolerance, suggesting that the PdO nanoflake must play an important role in the enhancement of the electrocatalytic performance of the Pt nanoparticles. In general, the enhancement in the electrocatalytic activity of Pt catalysts toward MOR is explained by the bi-functional mechanism and the electronic effect model [4, 5, 8, 10, 20, 23]. The bi-functional mechanism is widely used to describe how hydroxyl surface groups oxidize and remove CO adspecies from neighboring Pt adsorption sites, thus avoiding the CO poisoning. For the Pt/PdO electrode, Pt nanoparticles are surrounded by abundant Pd-OH surface groups, which are produced when metal Pd sites are oxidized in the acidic electrolyte via Eq. 5-2. CO adspecies in the rim of a Pt nanoparticle are readily oxidized by neighboring Pd-OH surface groups via the Langmuir-Hinshelwood reaction mechanism because of immediate interactions of the CO adspecies with Pd-OH groups surrounding the Pt nanoparticle [20, 23]. Pd-OH surface groups may also spill over a Pt nanoparticle and progressively interact with CO adspecies in the inner surface area of the nanoparticle, resulting in the recovery of Pt free sites, which allow further methanol adsorption and oxidation.
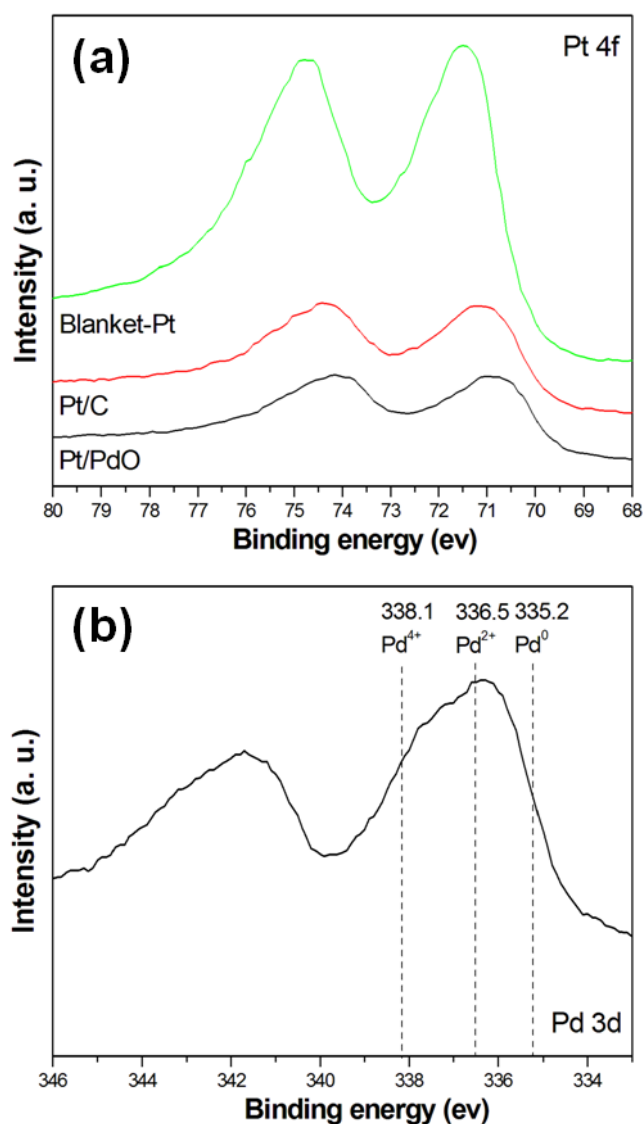
Figure 5-10 (a) Pt 4f spectra of the Pt/PdO, the Pt/C and the blanket-Pt electrodes before the electrochemical measurement; (b) the Pd 3d XPS spectrum of the as-prepared Pt/PdO electrode.

Besides the bi-functional mechanism, electronic interactions between Pt nanoparticles and the PdO support may also improve the electrocatalytic activity of the Pt catalyst toward MOR. The electronic interaction can modify the electronic structure of the Pt nanoparticle and thus alter the chemisorption behavior of CO adspecies on the nanoparticle [20, 23]. If the adsorption strength of CO adspecies becomes weaker as a result of the electronic structure modification on the Pt nanoparticle, the oxidation of CO adspecies may be kinetically favored, leading to a better catalytic activity of the Pt nanoparticle toward MOR.

Figure 5-10(a) shows Pt 4f spectra of the Pt/PdO, the Pt/C and the blanket-Pt electrodes before the electrochemical measurement. The Pt $4f_{7/2}$ peak of the Pt/PdO electrode is situated at 70.8 eV, which negatively shifts from that of the blanket Pt thin film (71.4 eV) by ~0.6 eV. Previous studies have shown that the binding energy of core level electrons of metal nanoparticles shifts from that of the bulk counterpart as a function of the particle size [116-118]. The binding energy shift due to the nanosize effect generally increases with decreasing the size of metal nanoparticles, and the size effect on the energy shift becomes unimportant when the particle size is larger than 3 nm [116]. Therefore, the large negative shift in the Pt $4f_{7/2}$ binding energy is unlikely to result from the nanosize effect but is caused by an electronic interaction between the Pt nanoparticle and the PdO support. The negative binding energy shift indicates that negative charge transfer from the PdO support to Pt nanoparticles must occur. Surface atoms of a smaller Pt nanoparticle should experience a larger electronic modification because of their close proximity to the interface between the Pt nanoparticle and the PdO support, at where the charge transfer takes place [20, 23]. The XPS analysis clearly shows the importance of the PdO substrate to the electronic effect, which may modify adsorption properties of methanol and CO adspecies on Pt nanoparticles and thus enhance the electrocatalytic activity of the Pt nanoparticles. The Pt/C electrode has the Pt 4f peak maximum at 71.2 eV; the less negative Pt 4f energy shift compared with the Pt/PdO electrode indicates that Pt particles on the Pt/C electrode are subject to a smaller electronic modification. Moreover, most Pt particles on the Pt/C electrode have a size in the order of a few tens of nanometers, and, as a result, the number of surface Pt atoms that experience the electronic modification is only a very small portion of the total Pt atoms on the particle. The electrochemical performance of the Pt/C electrode is consequently less efficient that of the Pt/PdO electrode.

Pd is liable to anodic dissolution in acidic electrolytes [43, 91, 93] and, therefore, is considered an unsuitable electrocatalyst in DMFCs. Since the PdO nanoflake has a CV
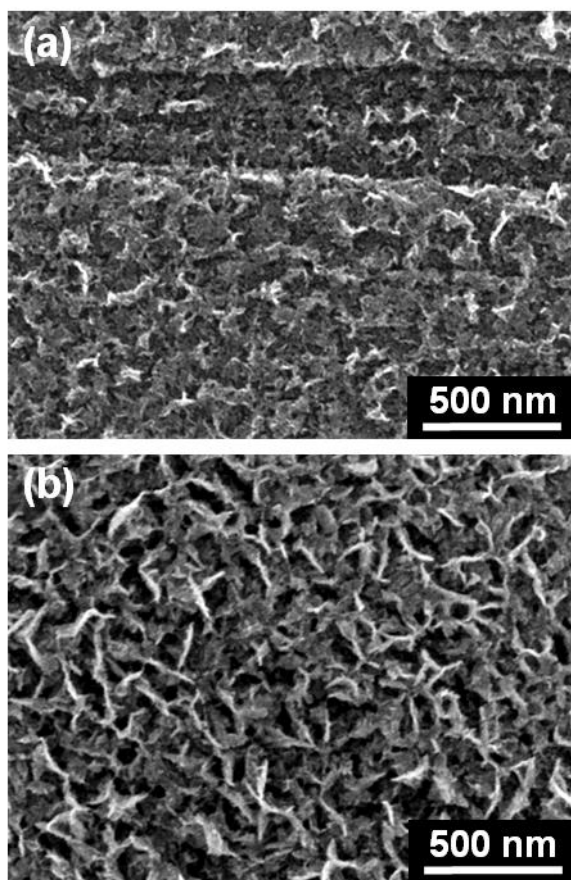
Figure 5-11 Images of (a) the PdO nanoflake electrode and (b) the Pt/PdO electrode after 10 CV cycles in the solution of 1M CH_3OH + 0.5 M H_2SO_4.

behavior similar to metallic Pd, the anodic dissolution is also expected to occur to the PdO nanoflake electrode. During a CV test in acidic solutions, anodic dissolution of Pd takes place when the surface PdO (or $Pd(OH)_2$), which is produced via the Pd oxidation in the forward sweep, is reduced in the reverse sweep, producing Pd^{2+} ions in the solution [43, 93]. Figure 5-11(a) shows the SEM image of a PdO nanoflake electrode after 10 CV cycles in the solution of 1M CH_3OH + 0.5 M H_2SO_4. The nanoflake morphology of the PdO/C electrode was nearly destroyed after 10 CV cycles, indicating severe anodic dissolution of Pd occurred. In contrast, the nanoflake feature was well preserved on the Pt/PdO electrode after 10 cycles of the CV measurement (Fig. 5-11(b)). This observation suggests that electrodeposited Pt nanoparticles can chemically stabilize the PdO support, and thus

69
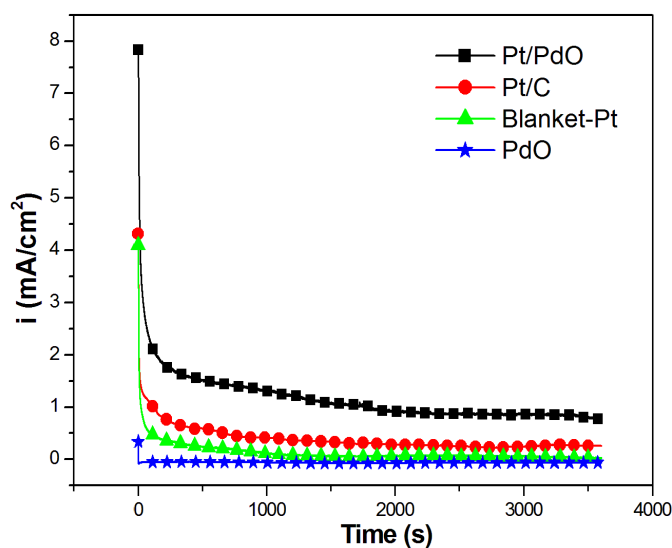
Figure 5-12 Chronoamperograms of the Pt/PdO electrode, the Pt/C, the blanket-Pt and the PdO electrodes in the aqueous solution of 1 M CH_3OH + 0.5 M H_2SO_4 at room temperature (~25 ^{o}C) for 1 h.   The oxidation potential was kept at 0.5 V vs. SCE.

suppress the anodic dissolution of the PdO nanoflake support.   It has been reported that the change in the surface chemical composition of Pd-containing alloys can affect the electrodissolution behavior of the alloys [43, 119, 120].   Figure 5-10(b) shows a Pd 3d XPS spectrum of the as-prepared Pt/PdO electrode.   After the Pt electrodeposition, the Pt/PdO electrode exhibits a broad Pd 3d peak, which comprises two component peaks or more; the Pd(II) and the Pd(IV) oxidation states can be easily assigned in the XPS spectrum. We do not know presently if the chemical phase with the Pd(IV) state is on the open area or covered by Pd nanoparticles, but the XPS analysis clearly demonstrates the dramatic change in the chemical composition on the surface of the PdO support after the Pt electrodeposition.   The distinct chemical change on the nanoflake surface may modify the electrochemical behavior of the PdO support and thus alleviate the anodic Pd dissolution during the CV measurement in acidic media.

To study the electrocatalytic stability of the Pt/PdO electrode in the solution of 1 M CH_3OH + 0.5 M H_2SO_4, we carried out chronoamperometric test at 0.5V.   The

70

chronoamperograms shown in Fig. 5-12 clearly demonstrates that the Pt/PdO electrode has a much better chronoamperometric performance than the Pt/C and the blanket-Pt electrodes. The Pt/PdO electrode has a gradual decrease in the current density within the first 30 min, and then its current density keeps steady at ~0.8 mA/cm^2. On the other hand, the Pt/C and the blanket-Pt electrodes show a low current density of 0.27 mA/cm^2 and 0.02 mA/cm^2, respectively, after one hour of the chronoamperometric test. For comparison, the chronoamperometric result of the PdO nanoflake electrode is also shown in Fig. 5-12; the electrode is completely inactive under the experimental condition. The much better chronoamperometric performance of the Pt/PdO electrode is ascribed to the large ESA and the better CO tolerance of Pt nanoparticles. Moreover, Pt nanoparticles can suppress the anodic dissolution of the PdO support and hence improve the electrochemical stability of the Pt/PdO electrode.

5.4 Summary

We prepared PdO nanoflake thin films on carbon cloths by reactive sputtering deposition, and pulse-electrodeposited Pt nanoparticles on the PdO thin films. The nanoflake morphology of the PdO support provides a large surface area for Pt nanoparticle loading, resulting in a large ESA. The electrocatalytic activity of the PdO thin film and the Pt/PdO electrode toward MOR was studied in acidic media. The PdO nanoflake thin film has a cyclic voltamperometric behavior similar to a metallic Pd electrode. According to the XPS analysis, a thin metallic Pd surface layer is produced on the PdO nanoflake thin film after the first cycle of the CV test in the aqueous H$_2$SO$_4$ solution. Because of the repetitive PdO reduction and Pd oxidation in the acidic solution, methanol electro-oxidation on the PdO nanoflake thin film exhibits a CV feature that is closely related to the Pd/PdO redox reaction. We proposed a reaction mechanism scheme to explain the observed CV

features for the methanol electro-oxidation on the PdO nanoflake electrode in the acidic solution. The nanoflake morphology on the PdO electrode is seriously damaged after 10 cycles of the CV test because of the anodic dissolution of metal Pd in acidic media. However, the anodic dissolution is greatly alleviated when Pt nanoparticles are electrodeposited on the PdO nanoflake thin film. The XPS study shows that negative charge transfer occurs from the PdO support to the Pt nanoparticles. The electronic interaction may modify adsorption properties of adspecies on the Pt nanoparticles, and thus affect electrochemical properties of the Pt/PdO electrode. The Pt/PdO electrode has a higher electrocatalytic activity toward MOR than the Pt/C and the blanket-Pt electrodes. We ascribe the much better electrocatalytic performance of the Pt/PdO electrode to a high CO tolerance and the large ESA. The high CO tolerance of the Pt-PdO electrode is a result of the synergism of the bi-functional mechanism and the electronic effect operating on the electrode.
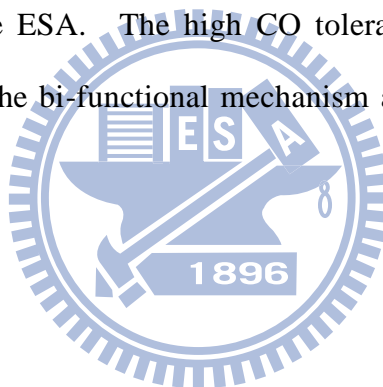
Chapter 6 Eletrocatalytic activity of Pt nanoparticles on a karst-like Ni Thin film toward methanol oxidation in alkaline solutions

6.1 Introduction

Transition metals are generally very corrosion resistant in alkaline solutions, and therefore they are good electrode materials for DMAFC applications. Because nickel hydroxides formed on Ni surfaces may act as chemical oxidizing agents for methanol oxidation in alkaline solutions [121, 122], the addition of Ni in Pt/Ru alloys can enhance the electrocatalytic activity of the electrode toward MOR [32]. Nickel has also been used as the Pt catalyst support for methanol electro-oxidation in alkaline solutions to enhance CO tolerance [29, 122]. In this study, we used HNO_3 wet-etch to prepare rugged Ni thin films, on which Pt nanoparticles were pulse-electrodeposited, for the study of electrocatalytic methanol oxidation in alkaline solutions. The rugged Ni thin film has a karst-like morphology, and is referred to as karst-Ni thin film thereafter. Pt nanoparticles on the karst-Ni thin film demonstrate a great improvement in the electrocatalytic performance for methanol oxidation in the alkaline electrolyte as compared with a blanket Pt thin film and Pt particles on a blanket Ni thin film.

6.2 Material characterizations

The e-beam deposited Ni thin film becomes very rugged after the HNO_3 wet etch, and has a surface morphology like a karst landform; we thus refer to the rugged Ni thin film as the karst-Ni thin film. The surface of the karst-Ni thin film is full of protruding structures of irregular shapes and cavities as shown in the cross-sectional SEM image of Fig. 6-1(b).

To illustrate the dramatic change in the surface morphology of the Ni thin film after the HNO$_3$ wet etch, the as-deposited Ni thin film is shown in Fig. 6-1(a).   The open and rugged surface of the karst-Ni thin film provides a large loading area for electrodeposited Pt nanoparticles.   Fig. 6-1(c) shows the side-view SEM image of the karst-Ni thin film after the Pt pulse-electrodeposition (thereafter referred to as Pt/karst-Ni).   The karst-Ni thin film retains its rugged morphology after the Pt electrodeposition, but the edge of the protruding structures becomes less sharp because of the accumulation of Pt nanoparticles. The size of the Pt nanoparticles is too small to be clearly observed in the SEM image. According to TEM analysis discussed later, the size of the Pt nanoparticles is about 5 nm in diameter.   We also prepared a blanket Ni thin film, on which Pt particles were subsequently electrodeposited (referred to as Pt/Ni), and a blanket Pt thin film for comparison with the Pt/karst-Ni thin film on the electrocatalytic activity toward MOR.
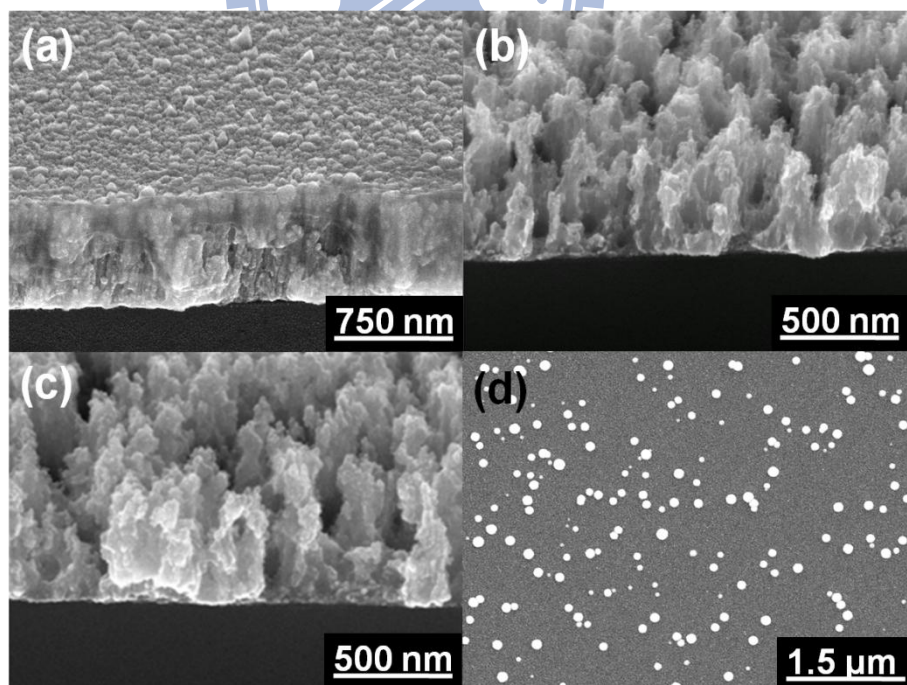
Figure 6-1 SEM images of (a) the as-deposited metallic nickel thin film, (b) the as-prepared karst-Ni thin film, (c) the karst-Ni thin film after the pulse-electrodeposition of Pt nanoparticles, and (d) the blanket-Ni thin film with pulse-electrodeposited Pt particles.

Fig. 6-1(d) shows an SEM image of the Pt/Ni thin film. Pt particles on the Pt/Ni thin film have a broad size distribution ranging from a few nm to hundreds of nanometers.

Figure 6-2(a) shows a cross-sectional TEM image of the Pt/karst-Ni thin film. The irregularly shaped Ni nanostructures are decorated by dark spots of nanometer scale, which randomly distribute over the karst-Ni thin film as shown in the enlarged TEM image of Figs. 6-2(b) and (c). The Ni nanostructures exhibit a slightly porous feature as indicated by some areas of bright contrast. Figure 6-2(d) shows a high resolution TEM image of two nanoparticles selected from the area marked by the square in the TEM image of Fig. 6-2(c). The lattice fringes clearly indicate that the nanoparticles are crystalline Pt grains with a diameter of ~5 nm. XRD analysis gives an average particle size slightly larger than 5 nm. Based on the peak width of the Pt(111) diffraction peak (not shown), the average particle
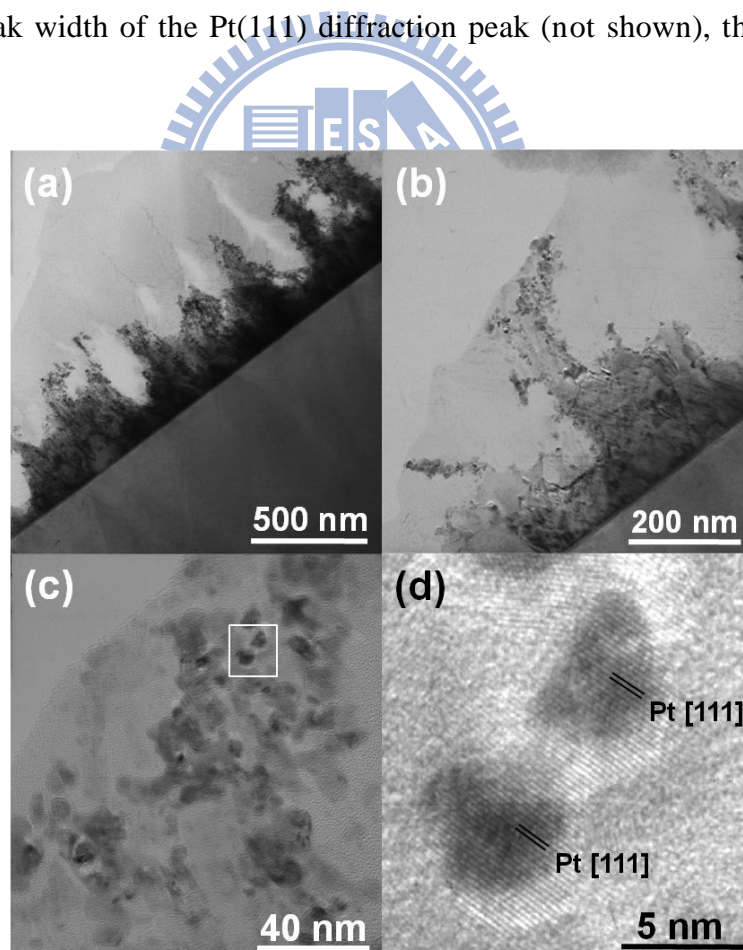
Figure 6-2 TEM images of the karst-Ni thin film with electrodeposited Pt nanoparticles in different magnifications (a), (b) and (c); HRTEM image of Pt nanoparticles on the karst-Ni support (d).

75
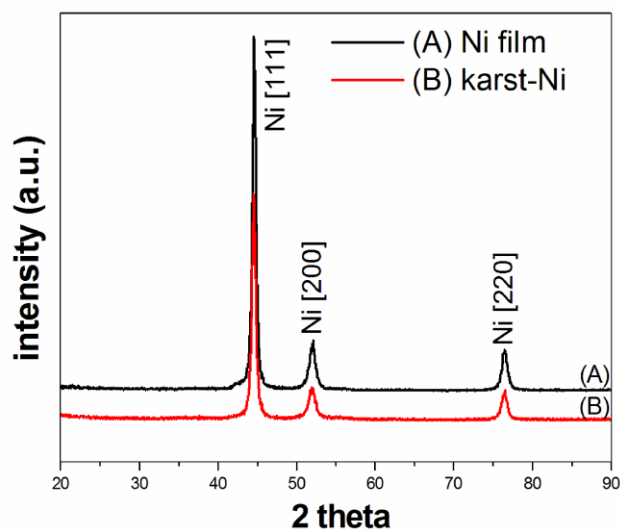
Figure 6-3 X-ray diffraction spectra of the as-deposited Ni thin film and the karst-Ni thin film

size of Pt nanoparticles on the karst-Ni support is about 5.6 nm according to the Scherrer equation.

Many studies have shown that transition metal oxide supports can greatly enhance the electrocatalytic activity of Pt toward methanol oxidation [15, 20]. The enhancement is generally ascribed to the bi-functional mechanism and/or the electronic effect, which are closely related to surface properties of the catalyst support [5, 106, 123]. To understand the surface property of the karst-Ni thin film, we used XRD and XPS to characterize chemical phases present on the HNO_3-etched Ni nanostructures. As shown in Fig. 6-3, the karst-Ni thin film has the same x-ray diffraction feature as the as-deposited blanket Ni thin film; the three diffraction peaks situated at 45°, 52° and 76° are due to the (111), (200) and (220) lattice planes, respectively, of the face centered cubic (FCC) lattice structure of metallic nickel. Although the XRD result suggests that the karst-Ni thin film is composed of metallic Ni, the XPS analysis shows that little metallic Ni is present on the surface of the karst-Ni thin film. The XPS spectra of the as-deposited Ni thin film and the karst-Ni thin film are shown in Fig. 6-4. The as-deposited blanket Ni thin film has a broad Ni $2p_{3/2}$ peak with the shoulder feature marked by the dashed line at 852.7 eV, which corresponds to
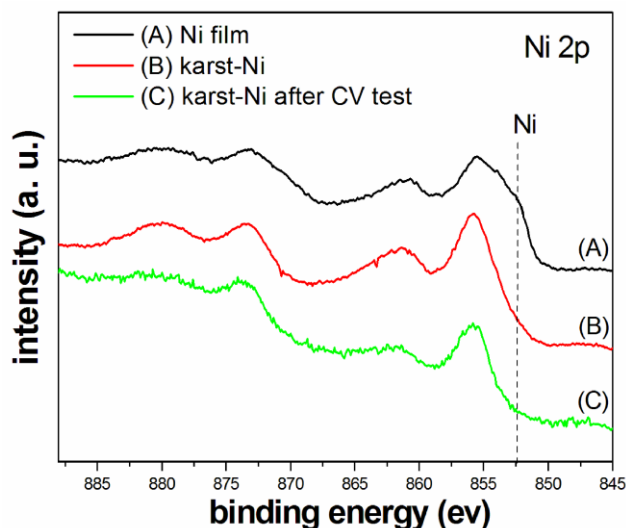
Figure 6-4 Ni(2p) XPS spectra of the as-deposited Ni thin film, the as-prepared karst-Ni thin film and a karst-Ni thin film after a 10-cycle CV scan in the aqueous solution of 1 M CH_3OH + 1 M KOH. The dashed line marks the Ni $2p_{3/2}$ binding energy of metallic Ni.

the $2p_{3/2}$ electron binding energy of metallic Ni. The rest of the broad Ni $2p_{3/2}$ peak at the higher binding energy side indicates the presence of an oxidized surface layer, which was formed during the shelf period waiting for the XPS analysis. For the as-prepared karst-Ni thin film and a karst-Ni thin film after 10 cycles of the CV scan (-0.9 to 0.2 V vs. SCE) in the aqueous solution of 1 M KOH + 1 M CH_3OH, the Ni $2p_{3/2}$ signal is primarily emitted from oxidized Ni species with little contribution from the metallic phase. As discussed later in more detail, the oxidized surface layer comprise various oxidized Ni species, such as NiO, Ni(OH)$_2$ and NiOOH. Combined with the XRD result, the XPS analysis suggests that the karst-Ni nanostructures has a metallic core, which is overlaid by a Ni oxide layer with a thickness larger than the escape depth of the Ni $2p_{3/2}$ photoelectron (~5 nm). The metallic Ni core is desirable for fast electrochemical kinetics for MOR in the alkaline solution because it has a good electrical conductivity.

6.3 Electrochemical measurements

Figure 6-5 shows cyclic voltammograms (CV) of methanol electro-oxidation in the aqueous solution of 1 M CH_3OH and 1 M KOH for the Pt/karst-Ni, the Pt/Ni and the blanket-Pt electrodes. The CVs were taken over the range between -0.9 and +0.2 V at a scan rate of 20 mVs^{-1}. Because methanol oxidation electrocatalyzed by Ni in alkaline solutions occurs in a higher potential range (0.36-0.45 V vs. SCE) [121], the anodic peak in the CV curve must represent the contribution entirely from the MOR electrocatalyzed by Pt. The Pt/karst-Ni electrode exhibits a very good electrocatalytic activity toward MOR in the alkaline solution as shown by the much higher anodic peak maximum in the forward scan compared with the other two electrodes. The large forward anodic current of the Pt/karst-Ni electrode can be ascribed to its large electrochemical surface active area (ESA). As determined from the CO stripping CV measurement in the 1 M KOH solution (discussed later in Fig. 6-6), the Pt/karst-Ni, the Pt/Ni and the blanket-Pt electrodes have an ESA of 511.2, 258.9 and 75.8 m^2/g, respectively, assuming an oxidation charge of 0.484 mC for a
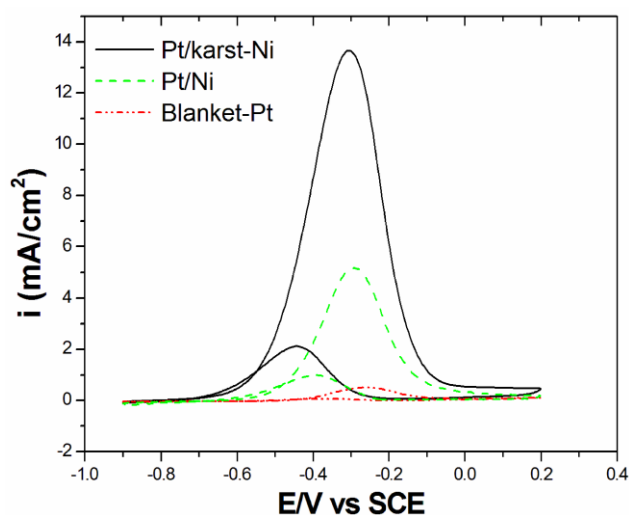
Figure 6-5 Cyclic voltammogarms of methanol electro-oxidation for the Pt/karst-Ni, the Pt/Ni and the blanket-Pt electrodes in the aqueous solution of 1 M CH_3OH + 1 M KOH. The scan rate was 20 mVs^{-1}. The current density is normalized to the sample surface area.

monolayer of CO molecules adsorbed on a smooth Pt surface [20]. The peak potential of MOR for the Pt/karst-Ni electrode is -0.31 V vs. SCE with the onset potential at -0.54 V, which is herein defined as the MOR potential at which the current density reaches 10% of the peak maximum. For the Pt/Ni electrode, the MOR peak potential and the onset potential are situated at -0.29 V and -0.49 V vs. SCE, respectively. The blanket-Pt electrode has the MOR peak potential (-0.25 V) and the onset potential (-0.45 V) less negative than the two Ni-supported electrodes, suggesting that the Ni supports can improve the electrocatalytic activity.

In addition to a large ESA, efficient removal of carbonaceous intermediates or residuals from the Pt catalyst surface during MOR is crucial to the electrocatalytic performance of an electrode. In CV measurements for methanol electro-oxidation in alkaline electrolytes, the anodic peaks in the forward scan is associated with chemisorption of methanol molecules and oxidation of intermediate organic species, and the anodic peak in the reverse scan is due to oxidation of weakly bonded CHO species, which are incompletely oxidized intermediates in the forward scan [34]. The ratio of the forward anodic current (I_f) to the reverse anodic current (I_b), I_f/I_b, is generally used as a simple index to signify the ability of the Pt catalyst to resist CO poisoning during MOR [20, 39, 124]. A small I_f/I_b value indicates that the methanol electro-oxidation reaction has a poor kinetics, leaving excessive carbonaceous adspecies on the Pt catalyst surface. From Fig. 6-5, the I_f/I_b ratios of the Pt/karst-Ni, the Pt/Ni and the blanket-Pt electrodes are 6.25, 5.67 and 4.92, respectively, indicating that electrodes using Ni as the Pt catalyst support have better CO tolerance in the KOH electrolyte than the blanket-Pt electrode. The CO stripping CV measurement discussed below provides direct evidences of better CO tolerance of the Ni supported Pt catalyst in the alkaline solution.
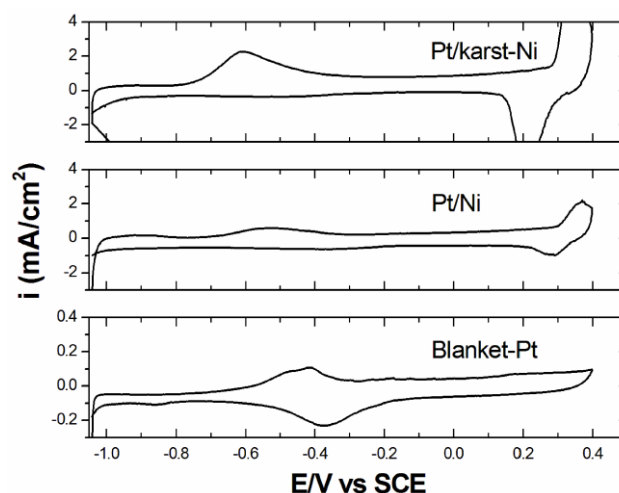
Figure 6-6 CO stripping cyclic voltammograms of the Pt/karst-Ni, the Pt/Ni and the blanket-Pt electrodes in the CO saturated 1 M KOH solution. The scan rate was 20 mVs^{-1}. The current density is normalized to the sample surface area.

The CO-stripping cyclic voltammograms of the three electrodes are shown in Fig. 6-6. For both the Ni supported Pt electrodes, a single broad peak is observed within the range between -0.8 and -0.1 V vs. SCE, while the blanket-Pt electrode has a doublet peak feature. In an acidic solution, CO adspecies on Pt usually exhibit two electro-oxidation peaks in CO stripping CVs [46, 60, 125], and the observation of the two potential peaks is ascribed to CO oxidation occurring on different lattice planes of the Pt electrocatalyst [125]. The doublet peak feature observed in the KOH solution may result from CO electro-oxidation at different lattice sites on the polycrystalline Pt thin film as well. The absence of the doublet peak feature for the two Ni-supported electrodes are likely due to that the electrodeposited Pt particles do not have a preferential distribution in the orientation planes that yield the characteristic doublet feature for CO electro-oxidation. The onset potential and the anodic peak potential are listed in pair for the Pt/karst-Ni, the Pt/Ni and the blanket-Pt electrodes, respectively, as follows: (-0.75 V, -0.62 V), (-0.72V, -0.52 V) and (-0.69, -0.42), where in the parenthesis the first value is the onset potential. The lower CO stripping onset potential indicates that the Pt/karst-Ni electrode has a smaller overpotential for the CO electro-oxidation. Combined with the high ESA, the lower onset and peak potentials of

CO electro-oxidation make the Pt/karst-Ni electrode much more electrocatalytically active toward MOR in the alkaline solution than the other two electrodes.

The improvement in the electro-oxidation activity of CO adspecies is generally ascribed to the bi-functional mechanism involved in the CO oxidation reaction and the electronic effect (ligand effect) due to charge transfer between the catalyst and the support [47, 126]. In the bi-functional mechanism model, oxygen containing adspecies, such as hydroxyl surface groups, can oxidize CO adspecies on the Pt catalyst, thereby avoiding CO poisoning. The CO electro-oxidation reaction via the bi-functional mechanism can be expressed by the following equation.

$$CO_{Pt} + 2OH^-_M \rightarrow CO_2(g) + H_2O + 2e^- \qquad (6\text{-}1)$$

where the subscript M represents Pt atoms or hydroxylated sites (e.g. Ni-OH) immediately adjacent to a CO-bonded Pt site. Chemical reaction processes on a surface are generally described by either the Langmuir-Hinshelwood (L-H) mechanism or the Eley-Rideal (E-R) mechanism. For methanol electro-oxidation in acidic electrolytes, the bifunctional mechanism can be best understood by the L-H mechanism, in which adsorbed reactants migrate on the surface and reactions take place by collision between adspecies. The CO electro-oxidation reaction via the L-H mechanism requires that OH adspecies be present on the Pt catalyst surface. Because of the deficiency in OH⁻ ions in an acidic solution, OH adspecies on a Pt catalyst particle are primarily produced by dissociative adsorption of water molecules or OH spillover from neighboring hydroxylated sites. The ease of the CO oxidation reaction via the L-H mechanism greatly depends on adsorption properties of CO and OH adspecies, such as the (CO)-Pt bond strength and the surface diffusivity of CO and OH adspecies. Opposite to acidic solutions, alkaline electrolytes contain abundant OH⁻ ions, and thus the E-R mechanism should also be considered an important reaction pathway leading to the CO electro-oxidation and removal. In an E-R surface reaction, the reaction product is formed by direct collision of a reactant species from the solution phase with a

reactant adspecies. According to the E-R mechanism model, CO adspecies on the Pt catalyst can be readily oxidized by OH^- ions diffusing from the bulk alkaline electrolyte. Because all the three electrodes of this study are immersed in the KOH solution of the same chemical ingredients, the collision rate per unit area of OH^- ions with CO adspecies on the three electrode must be the same. Under such condition, the E-R mechanism should be more prevailing on the electrode with CO adsorption structures allowing more effective CO oxidation and easier (CO)-Pt bond breaking. From the above discussion, for both the E-R and the L-H mechanisms, the electrochemical activity of the CO oxidation reaction is closely related to adsorption properties of the CO adspecies. Because CO adsorption properties are governed by surface properties of the Pt catalyst, which can be modified by the Ni support, the electronic interaction between the Pt catalyst and the Ni support can greatly influence the electrochemical activity of CO oxidation on the Ni-supported electrodes of this study. According to XPS analysis, the Pt/karst-Ni and the Pt/Ni electrodes have a large negative shift in the Pt $4f_{7/2}$ binding energy, indicating that charge transfer occurs between the Pt catalyst and the Ni support.

The Pt(4f) XPS spectrum of the Pt/karst-Ni thin film shown in Fig. 6-7 exhibits a doublet peak with the Pt $4f_{7/2}$ peak maximum at 70.7 eV, which negatively shifts from that of the blanket Pt thin film by ~0.7 eV. The negative binding energy shift of the Pt 4f doublet peak can be ascribed to either the nanometer-size effect of Pt nanoparticles or charge transfer between Pt nanoparticles and the Ni support, or a combination of the both effects. It has been widely reported that the binding energy of core level electrons of metal nanoparticles shifts from that of the bulk counterparts as a function of the particle size [116-118]. The binding energy shift generally increases with decreasing the size of metal nanoparticles; and the size effect on the energy shift becomes insignificant when the particle size is larger than 3 nm [116]. Because Pt nanoparticles on the Pt/karst-Ni electrode have a particle size around 5 nm, the large negative shift (-0.7 eV) in the Pt $4f_{7/2}$
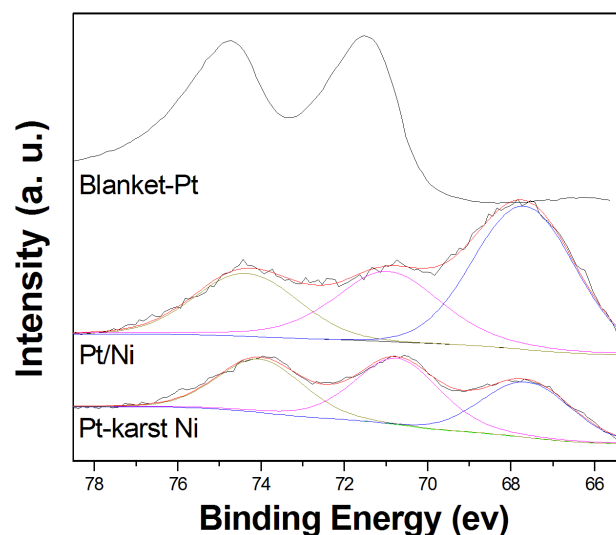
Figure 6-7 The Pt 4f XPS spectra of the Pt/karst-Ni, the Pt/Ni and the blanket-Pt electrodes.   In the spectra of the two Ni-supported electrodes, the peak situated around 67.6 eV is due to the Ni 3p signal emitted from the Ni support.   Curve fitting was carried out so that the Pt $4f_{7/2}$ binding energy for the two Ni-supported electrodes could be more accurately determined.

binding energy suggests that negative charge transfer from the karst-Ni support to Pt nanoparticles has occurred.   A theoretical study showed that, upon adsorption on the NiO(100) surface, Pt atoms sit on the oxygen-top site and form strong chemical bonds with the surface as a result of a change in the electronic configuration of Pt atoms [127].   It is likely that Pt atoms adsorbed on nickel hydroxides are also subject to a strong electronic modification.   Surface atoms of a smaller Pt nanoparticle should experience a larger electronic modification because of their close proximity to the interface between the nanoparticle and the Ni support, at where the charge transfer takes place.   For the Pt/Ni electrode, the curve-fitted Pt $4f_{7/2}$ peak has the maximum at 71.0 eV and has a slightly larger full-width-at-half-maximum (FWHM) than the Pt/karst-Ni electrode.   The less negative Pt 4f energy shift and the larger FWHM indicate that Pt particles on the Pt/Ni electrode have a smaller electronic modification with a wider distribution of the modification strength.   This is because the Pt particles on the Pt/Ni electrode have a wide size distribution ranging from a few to a few hundred nanometers, and, as a result, surface

atoms clearly experiencing the electronic modification are far fewer than atoms lacking the modification. Figure 6-8 schematically illustrates the progressive decrease in the electronic modification as a function of the distance from the interface between a Pt nanoparticle and the hydorxylated Ni support. The colored area indicates the region affected by the charge transfer between the Pt nanoparticle and the Ni support, and the gradually shaded color represents the degree of the induced electronic modification. A smaller nanoparticle is apparently has a larger portion of surface atoms that are subject to the electronic modification. Because of the greater electronic modification of Pt nanoparticles, the Pt/karst-Ni electrode must exhibit an electrocatalytic activity distinct from the Pt/Ni and the blanket-Pt electrodes. The better CO electro-oxidation performance for the Pt/karst-Ni electrode, as shown in Fig. 6-6, suggests that the electronic modification due to the charge transfer results in a (CO)-Pt adsorption structure that enhances the CO electro-oxidation activity in the alkaline solution. The Pt/Ni electrode also benefits from the electronic modification for better CO tolerance although the improvement is less significant than the Pt/karst-Ni electrode.

In a study of the mechanism of CO oxidation in NaOH solutions, Spendelow et al, found that CO electro-oxidation on the Pt(111) surface was primarily via the L-H mechanism [128]. In such case, OH adspecies must be present on the Pt catalyst surface so that the CO oxidation reaction can proceed, as shown by reaction 1 in Fig. 6-8. A previous study has shown that OH adsorption on the Pt(111) surface in alkaline solutions occurs in the potential range between 0.65 and 0.85 V vs. RHE (equivalent to -0.36 − -0.16 V vs. SCE) [129]. The potential range for OH adsorption on the Pt(111) surface is much less negative than the measured potential range (-0.8 − -0.4 V vs. SCE) for the CO electro-oxidation reaction occurring on the Pt/karst-Ni electrode. Although Pt nanoparticles on the Pt/karst-Ni electrode must comprise various surface lattice planes and defects, on which OH adsorption may take place at different potentials, the very negative
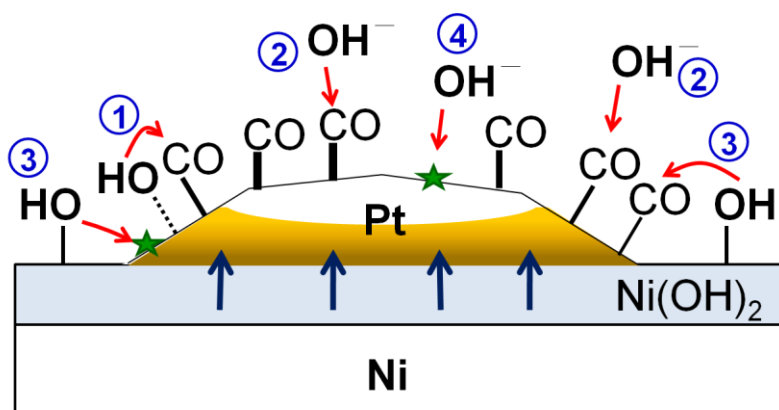
Figure 6-8 Schematic illustration of the synergistic effect of the bifunctional mechanism and the electronic effect for CO electro-oxidation on Pt nanoparticles adhered to the Ni support. The arrows represent negative charge transfer from the Ni(OH)$_2$ surface layer to the Pt nanoparticle. The gradually shaded color indicates the degree of the induced electronic modification on the Pt nanoparticle as a result of the charge transfer. The thickness of the lines connecting CO adspecies with Pt nanoparticle represents the magnitude of the bond strength, which depends on the degree of the electronic modification and exposed surface lattice planes of the Pt nanoparticle. The reactions numbered by 1 and 2 denote CO oxidation by an OH adspecies via the L-H mechanism and by an OH⁻ ion from the electrolyte via the E-R mechanism, respectively. The processes numbered by 3 represent that an OH surface group on the Ni(OH)$_2$ surface layer reacts with an neighboring CO adspecies on the Pt nanoparticle, or migrates to a free surface site (labeled by the star symbol) on the nanoparticle. The OH⁻ ion numbered by 4 denotes the diffusion of the OH⁻ ion toward a free surface site, which can be created by the removal of an oxidized CO adspecies.

CO stripping peak potential (~-0.6 V) suggests that OH adspecies produced on Pt nanoparticles during the CV scan are unimportant to the CO electro-oxidation reaction occurring on the Ni-supported electrode. Therefore, to facilitate CO electro-oxidation at the low potential region, OH spillover from the Ni support to Pt nanoparticles becomes a likely channel to supply OH adspecies needed for the CO electro-oxidation reaction via the L-H mechanism. Ni is readily oxidized in alkaline solutions, forming various hydroxides on the substrate surface [122, 130]. According to the Ni 2p XPS spectrum shown in Fig. 6-9, the surface of a karst-Ni thin film (before Pt electrodeposition) is rich in hydroxylated species after a 10-cycle CV scan in the aqueous solution of 1 M KOH + 1 M CH$_3$OH. The spectrum was curve-fitted assuming a Gaussian-Lorentzian peak shape and the binding

energies for the fitted peaks were determined by referring to literature data [131-134]. The XPS analysis shows that $Ni(OH)_2$ is the most abundant chemical phase on the surface of the Ni support, and a significant amount of NiOOH is also present on the surface. Nickel oxidation on a Ni electrode in alkaline media can be expressed by the following reactions: [122]

$$Ni + 2OH^- \rightleftharpoons Ni(OH)_2 + 2e^- \tag{6-2}$$

$$Ni(OH)_2 + OH^- \rightleftharpoons NiOOH + H_2O + e^- \tag{6-3}$$

$Ni(OH)_2$ is formed on the Ni surface in the potential range between -1.1 and -0.6V vs. SCE, and the transformation of α-$Ni(OH)_2$ to β-$Ni(OH)_2$ occurs in the range from -0.6 to 0.3 V vs. SCE [130]. Further oxidation of $Ni(OH)_2$ to NiOOH proceeds at a higher potential (~0.4 V vs. SCE) [130]. Because CO oxidation on the three electrodes of this study occurs at a potential much smaller than the formation potential of the NiOOH phase, OH adspecies involved in the CO electro-oxidation reaction via the L-H mechanism must be mainly provided by the $Ni(OH)_2$ phase. As discussed above, a Pt nanoparticle has a high CO
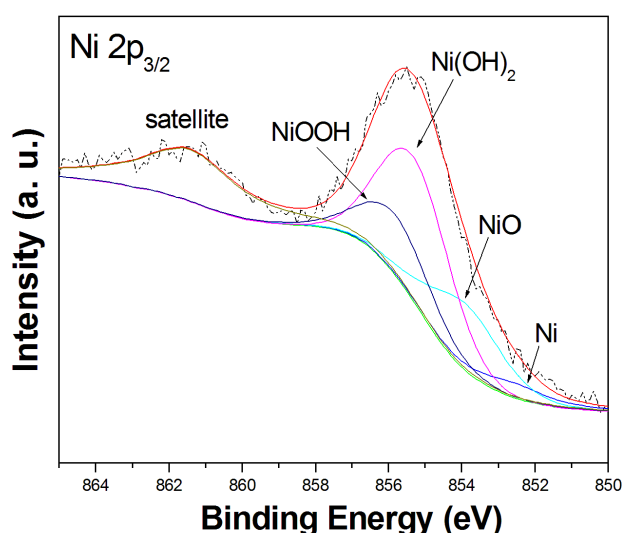
Figure 6-9 Ni $2p_{3/2}$ XPS spectrum of a karst-Ni thin film after a 10-cycle CV scan in the aqueous solution of 1 M CH_3OH + 1 M KOH. Curve fitting was carried out to resolve the component peaks of metallic Ni, NiO, $Ni(OH)_2$ and NiOOH.

electro-oxidation activity in the perimeter because of the strong electronic interaction between Pt atoms in the perimeter and the Ni support. OH surface groups stemming from the $Ni(OH)_2$ phase and surrounding a Pt nanoparticle can either migrate to empty surface sites in the perimeter of the Pt nanoparticle or react directly with neighboring CO adspecies on the Pt nanoparticle (as shown by reaction 3 in Fig. 6-8.) Therefore, CO electro-oxidation via the L-H mechanism should be more pronounced in the peripheral region of a Pt nanoparticle than in the inner area. New empty surface sites are created in the perimeter of the Pt nanoparticle after oxidized CO adspecies are removed, and can be reoccupied by CO or OH adspecies migrating on the nanoparticle, allowing progressive CO oxidation through the particle surface via the L-H mechanism. The L-H model scenario is more applicable to Pt nanoparticles of smaller size. On a smaller particle, OH and CO adspecies can migrate over the particle in a shorter time, resulting in a higher collision rate between CO and OH adspecies, and thus a more efficient CO electro-oxidation reaction.

Although Spendelow et al. [128] has proposed that CO electro-oxidation via the L-H mechanism predominates on the Pt(111) surface in alkaline electrolyte , we cannot rule out the participation of the E-R mechanism in the CO electro-oxidation reaction on the Ni-supported electrodes. Because Pt nanoparticles on the electrodes must comprise defects and surface planes other than the Pt(111) plane, it is likely that these surface sites may provide an adsorption environment for CO adspecies allowing oxidation by OH anions from the alkaline electrolyte via the E-R mechanism. If the E-R reaction takes place, like the CO oxidation reaction via the L-H mechanism, the catalyst particle size can influence the eletroactivity of the CO oxidation reaction via the E-R mechanism as well. When CO adspecies have an adsorption structure kinetically favoring the CO electro-oxidation reaction via the E-R mechanism, collision of the CO adspecies with OH^- ions diffusing from the bulk electrolyte (as shown by reaction 2 in Fig. 6-8) will lead to a high electro-oxidation activity. If the electronic modification results in a CO adsorption
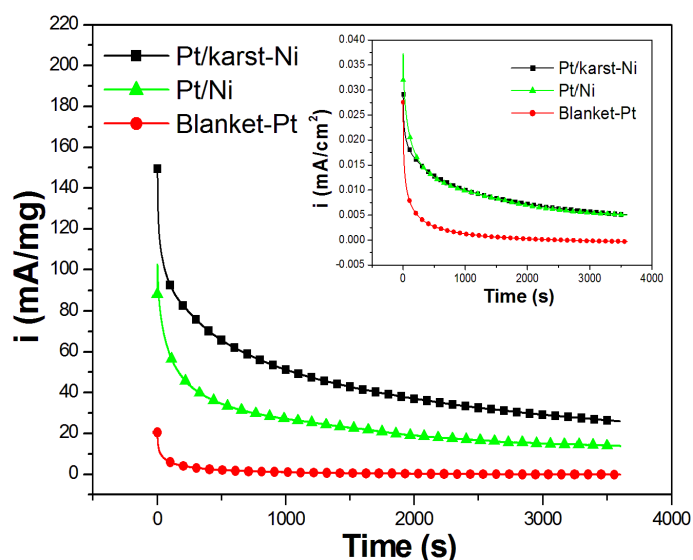
Figure 6-10 Chronoamperometry curves of the Pt/karst-Ni, the Pt/Ni and the blanket-Pt electrodes in the aqueous solution of 1 M CH$_3$OH + 1 M KOH at room temperature (~25 ^{o}C) for 1 h.   The oxidation potential was kept at -0.3 vs. SCE.   The inset shows the same chronoamperometric results but the y-axis label "mass activity" is replaced by the current density normalized to the electrochemical surface area.

structure that can enhance CO electro-oxidation via the E-R mechanism, a smaller Pt particle will have a higher electrocatalytic activity toward CO electro-oxidation than a larger one.

Figure 6-10 shows chronoamperograms of the Pt/karst-Ni, the Pt/Ni and the blanket-Pt electrodes at the oxidation potential of -0.3 V vs. SCE in the aqueous solution of 1 M CH$_3$OH + 1 M KOH.   All the three electrodes demonstrate a gradual decrease in the mass activity with the polarization time.   In addition to the possible carbonaceous residue left on the Pt catalyst due to incomplete methanol electrooxidation, Pt catalyst loss and/or agglomeration may take place and thun reduce the ESA.   Moreover, the reaction between the alkaline electrolyte and CO$_2$, which is the product of CO electrooxidation, can produce carbonates [17, 29, 135].   Formation of insoluble carbonates may consume the electrolyte and/or block active sites on the anode, thereby degrading the electrocatalytic performance of the electrode.   For the blanket-Pt electrode, the mass activity rapidly drops to ~3.1 mA/mg within the first 300 s and becomes nearly zero mA/mg after one hour of the test.

For the Pt/Ni electrode, the drop of the mass activity is less severe compared with the blanket-Pt electrode, and the mass activity decreases to ~13.7 mA/mg after one hour of the methanol electro-oxidation. On the other hand, the Pt/karst-Ni electrode maintains a high mass activity through the electrochemical test and has a mass activity of ~27.1 mA/mg at the end of the 1-hr measurement. The inset of Fig. 10 presents the same chronoamperometric results but with the labeled current density normalized to the electrochemical surface area. The inset shows that the two Ni-based electrodes have similar chronoamperometric properties. The better electrocatalytic performance of the two Ni-based electrodes for MOR in the alkaline solution can be ascribed to better CO tolerance, which is a result of the synergistic effect of the bi-functional mechanism and the strong electronic interaction between the Pt catalyst and the Ni support. The steady and high mass activity of the Pt/karst-Ni electrode also infers that Pt nanoparticles pulse-electrodeposited on the rugged karst-Ni support are electrochemically stable in the alkaline solution. The Pt/Ni-karst electrode has a higher mass activity than the Pt/Ni electrode, and is thus a better electrode for methanol oxidation in respect to the utilization of the precious Pt catalyst.

6.4 Summary

The study prepared rugged Ni thin films on the Si substrate by HNO_3 wet etch, and the etched Ni thin films were used as Pt catalyst supports for the study on electrocatalytic MOR in the aqueous KOH solution. Pt nanoparticles of ~5 nm in size were successfully pulse-electrodeposited on the Ni support. The rugged Ni thin film has a karst-like surface morphology, and comprises irregular nanostructures featuring a metallic Ni core capped by Ni oxides. XPS analysis shows that $Ni(OH)_2$ is formed on the Ni support during the potential scan in the alkaline solution. The hydroxide may enhance CO tolerance of the Pt

catalyst via the bi-functional mechanism and thus improve the electrocatalytic activity toward MOR. The L-H and the E-R mechanisms are used to elucidate the role of OH surface groups on the Ni support and OH⁻ ions in the KOH solution, respectively, in the enhancement of CO tolerance in the alkaline electrolyte. The negative shift in the Pt(4f) binding energies suggests that negative charge transfer takes place from the Ni support to the Pt catalyst. The electronic interaction may modify adsorption properties of CO adspecies on the Pt catalyst, and the modification on a Pt nanoparticle allows easy CO electro-oxidation by OH species surrounding the nanoparticles, either from the Ni support or from the alkaline solution. The synergistic effect of the bi-functional mechanism and the electronic interaction enhance CO tolerance of Pt nanoparticles, and thus the electrocatalytic activity toward MOR in the KOH solution. Because of the large electrochemical area and the nanometer-size of Pt particles, the Pt/karst-Ni electrode exhibits better electrocatalytic performance for MOR in the alkaline solution than the Pt/Ni and the blanket-Pt electrodes.
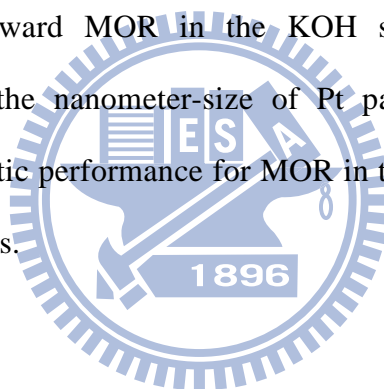
Chapter 7   Conclusions and Future Works

7.1 Conclusions

In this study, we prepared metal oxides of three different kinds for the use of the Pt catalyst support for MOR electroactivity study.   Porous TiO_2 thin film was prepared on the Si substrate by hydrothermal method. The porous TiO_2 support was mainly composed of anatase phase after vacuum annealing at 600^oC and showed an electrical conductivity good for Pt electroplating and electrochemical measurement.   The Pt/TiO_2-3h electrode had a much larger ESA because of the porous structure of the TiO_2 support and well dispersed Pt nanoparticles.   MOR CV and CO stripping measurements indicated that the Pt/TiO_2-3h electrode had a high electrocatalytic activity toward MOR and a very good CO tolerance. The good CO tolerance is ascribed to the synergistic effect of Pt nanoparticles and the porous TiO_2 support.   The nanosized scale of the Pt catalyst allows easy access of CO adspecies by hydroxyl surface groups on the TiO_2 surface, thereby CO electro-oxidation prevails around the peripheral area of Pt nanoparticles via bifunctional mechanism.   The strong electronic interaction between the Pt nanoparticle and the TiO_2 substrate might weaken the chemisorption strength of CO adspecies on the Pt catalyst, and thus enhance CO electro-oxidation activity.

PdO nanoflake thin films were prepared on carbon cloths by reactive sputtering deposition, and pulse-electrodeposited Pt nanoparticles on the PdO thin films.   The nanoflake morphology of the PdO support provides a large surface area for Pt nanoparticle loading, resulting in a large ESA. The PdO nanoflake thin film has a cyclic voltamperometric behavior similar to a metallic Pd electrode.   A thin metallic Pd surface layer is produced on the PdO nanoflake thin film after the first cycle of the CV test. Methanol electro-oxidation on the PdO nanoflake thin film exhibits a CV feature that is closely related to the Pd/PdO redox reaction.   We proposed a reaction mechanism scheme

to explain the observed CV features for the methanol electro-oxidation on the PdO nanoflake electrode in the acidic solution. The nanoflake morphology on the PdO electrode is seriously damaged after CV test because of the anodic dissolution of metal Pd in acidic media. However, the anodic dissolution is greatly alleviated when Pt nanoparticles are electrodeposited on the PdO nanoflake thin film. The XPS study shows that negative charge transfer occurs from the PdO support to the Pt nanoparticles. The electronic interaction may modify adsorption properties of adspecies on the Pt nanoparticles, and thus affect electrochemical properties of the Pt/PdO electrode. We ascribe the much better electrocatalytic performance of the Pt/PdO electrode to a high CO tolerance and the large ESA. The high CO tolerance of the Pt-PdO electrode is a result of the synergism of the bi-functional mechanism and the electronic effect operating on the electrode.

Rugged Ni thin films were prepared on the Si substrate by HNO_3 wet etch, and the etched Ni thin films were used as Pt catalyst supports for the study on electrocatalytic MOR in the aqueous KOH solution. The rugged Ni thin film has a karst-like surface morphology, and comprises irregular nanostructures featuring a metallic Ni core capped by Ni oxides. XPS analysis shows that $Ni(OH)_2$ is formed on the Ni support during the potential scan in the alkaline solution. The hydroxide may enhance CO tolerance of the Pt catalyst via the bi-functional mechanism and thus improve the electrocatalytic activity toward MOR. The L-H and the E-R mechanisms are used to elucidate the role of OH surface groups on the Ni support and OH^- ions in the KOH solution, respectively. The negative shift in the Pt(4f) binding energies suggests that negative charge transfer takes place from the Ni support to the Pt catalyst. The electronic interaction may modify adsorption properties of CO adspecies on the Pt catalyst, and the modification on a Pt nanoparticle allows easy CO electro-oxidation by OH species surrounding the nanoparticles, either from the Ni support or from the alkaline solution. The synergistic effect of the bi-functional mechanism and the electronic interaction enhance CO tolerance of Pt

nanoparticles, and thus the electrocatalytic activity toward MOR in the KOH solution.

7.2 Future works

In this study, we have shown that metal oxides of three different kinds used as Pt catalyst supports can greatly enhance CO tolerance of Pt nanoparticles, and thus the electrocatalytic activity toward MOR. However, some subjects may be further studied:

(A) TiO_2 has intriguing photo-catalytic properties and has long been used as a catalyst or support in photo-electrochemical systems. Seger et al. constructed a polymer membrane electrode assembly (MEA), consisting of a TiO_2 photoanode, a Pt cathode, and a proton exchange membrane, to generate hydrogen continuously under UV excitation with no applied bias, and the operation principle of photoelectrolysis cell based was shown in figure 7-1[1]. The use of methanol as sacrificial electron donor in the anode significantly decreases the overvoltage for electrode reactions and thus enables the production without any external bias. Besides, the influence of Pt/TiO_2 photocatalysts on H_2 production is also extensively investigated [136]. In our study,
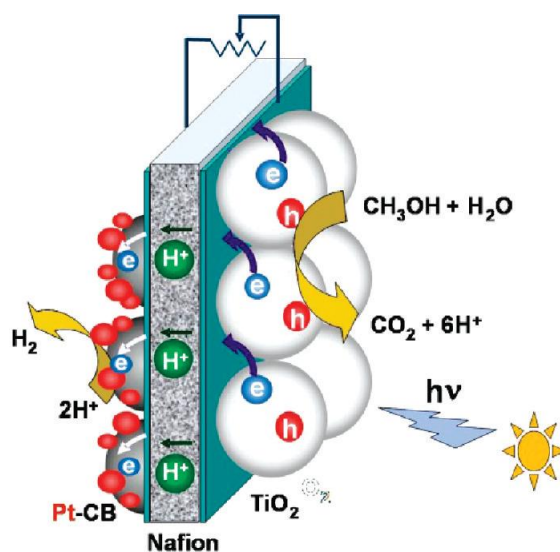
Figure 7-1 Operation principle of photoelectrolysis cell based on TiO_2/Nafion/Pt-CB assembly[1].

Pt/porous TiO$_2$ electrode was prepared by hydrothermal method and has an excellent electrocatalytic activity toward methanol electro-oxidation. It may be used as an electrode of photo-catalysts for the application of photocatalytic hydrogen production.

(B) Previous study shows that palladium has an electrocatalytic hehavior similar to Pt for electro-oxidation of methanol, ethanol and formic acid [104-106]. However, Pd is liable to anodic dissolution in acidic electrolytes and is considered an unsuitable electrocatalyst in DMFCs. Although, in our study, the anodic dissolution is greatly alleviated when Pt nanoparticles are electrodeposited on the PdO nanoflake thin film, Pd is still more stable in alkaline solution compared with in acidic solution. Many metallic Pd nanostructures of high surface, such as nanowires, nanoflowers and clusters, are investigated for electrochemical study [82, 86, 137]. In our study, the nanoflake-like morphology of the as deposited PdO thin film results in a large surface area, providing enormous electrochemical active sites. Metallic Pd nanoflakes can be found by hydrogen reduction or CV tests of PdO nanoflakes. The metallic Pd nanoflake electrode of high surface area may be utilized as an electrocatalyst not only for methanol electro-oxidation reaction but also ethanol or formic acid electrooxidation in alkaline systems.

References

[1] B. Seger, P.V. Kamat, The Journal of Physical Chemistry C, 113 (2009) 18946-18952.

[2] R. O'Hayre, S.W. Cha, W. Colella, F.B. Prinz, Fuel cell fundamentals, John Wiley&Sons, New Jersey, (2005).

[3] T. Frelink, W. Visscher, J.A.R. van Veen, Surface Science, 335 (1995) 353-360.

[4] C. Lu, C. Rice, R.I. Masel, P.K. Babu, P. Waszczuk, H.S. Kim, E. Oldfield, A. Wieckowski, The Journal of Physical Chemistry B, 106 (2002) 9581-9589.

[5] J.M. Léger, S. Rousseau, C. Coutanceau, F. Hahn, C. Lamy, Electrochimica Acta, 50 (2005) 5118-5125.

[6] P. Waszczuk, G.Q. Lu, A. Wieckowski, C. Lu, C. Rice, R.I. Masel, Electrochimica Acta, 47 (2002) 3637-3652.

[7] F. Maillard, G.Q. Lu, A. Wieckowski, U. Stimming, The Journal of Physical Chemistry B, 109 (2005) 16230-16243.

[8] G.Y. Zhao, C.L. Xu, D.J. Guo, H. Li, H.L. Li, Journal of Power Sources, 162 (2006) 492-496.

[9] M.C. Tsai, T.K. Yeh, C.H. Tsai, Electrochemistry Communications, 8 (2006) 1445-1452.

[10] E. Antolini, Applied Catalysis B: Environmental, 74 (2007) 337-350.

[11] J.N. Tiwari, T.M. Chen, F.M. Pan, K.L. Lin, Journal of Power Sources, 182 (2008) 510-514.

[12] T. Maiyalagan, Applied Catalysis B: Environmental, 80 (2008) 286-295.

[13] C. Xu, Z. Tian, P. Shen, S.P. Jiang, Electrochimica Acta, 53 (2008) 2610-2618.

[14] X. Wang, R. Kumar, D.J. Myers, Electrochem. Solid-State Letters, 9 (2006) A225.

[15] Y.J. Gu, W.T. Wong, Journal of The Electrochemical Society, 153 (2006) A1714-A1718.

[16] E.E. Switzer, T.S. Olson, A.K. Datye, P. Atanassov, M.R. Hibbs, C.J. Cornelius, Electrochimica Acta, 54 (2009) 989-995.

[17] J. Bagchi, S.K. Bhattacharya, Journal of Power Sources, 163 (2007) 661-670.

[18] F.C. Simões, D.M. dos Anjos, F. Vigier, J.M. Léger, F. Hahn, C. Coutanceau, E.R. Gonzalez, G. Tremiliosi-Filho, A.R. de Andrade, P. Olivi, K.B. Kokoh, Journal of Power Sources, 167 (2007) 1-10.

[19] S.T. Nguyen, H.M. Law, H.T. Nguyen, N. Kristian, S. Wang, S.H. Chan, X. Wang, Applied Catalysis B: Environmental, 91 (2009) 507-515.

[20] C.S. Chen, F.M. Pan, Applied Catalysis B: Environmental, 91 (2009) 663-669.

[21] L.X. Yang, C. Bock, B. MacDougall, J. Park, Journal of Applied Electrochemistry, 34 (2004) 427-438.

[22] M.S. Saha, R. Li, M. Cai, X. Sun, Electrochemical and Solid-State Letters, 10 (2007) B130-B133.

[23] C.S. Chen, F.M. Pan, H.J. Yu, Applied Catalysis B: Environmental, 104 (2011) 382-389.

[24] M.L. Anderson, R.M. Stroud, D.R. Rolison, Nano Letters, 2 (2002) 235-240.

[25] G. Che, B.B. Lakshmi, E.R. Fisher, C.R. Martin, Nature, 393 (1998) 346-349.

[26] S.H. Joo, S.J. Choi, I. Oh, J. Kwak, Z. Liu, O. Terasaki, R. Ryoo, Nature, 412 (2001) 169-172.

[27] B. Rajesh, K.R. Thampi, J.M. Bonard, A.J. McEvoy, N. Xanthopoulos, H.J. Mathieu, B. Viswanathan, Journal of Power Sources, 133 (2004) 155-161.

[28] W. Li, X. Wang, Z. Chen, M. Waje, Y. Yan, The Journal of Physical Chemistry B, 110 (2006) 15353-15358.

[29] L. Carrette, K.A. Friedrich, U. Stimming, Fuel Cells, 1 (2001) 5-39.

[30] M.P. Hogarth, G.A. Hards, Platinum Matels Review, 40 (1996) 150-159.

[31] E. Antolini, J.R.C. Salgado, E.R. Gonzalez, Applied Catalysis B: Environmental, 63 (2006) 137-149.

[32] K.W. Park, J.H. Choi, B.K. Kwon, S.A. Lee, Y.E. Sung, H.Y. Ha, S.A. Hong, H. Kim, A. Wieckowski, The Journal of Physical Chemistry B, 106 (2002) 1869-1877.

[33] A.V. Tripkovic, K.D. Popovic, B.N. Grgur, B. Blizanac, P.N. Ross, N.M. Markovic, Electrochimica Acta, 47 (2002) 3707-3714.

[34] J. Prabhuram, R. Manoharan, Journal of Power Sources, 74 (1998) 54-61.

[35] N.M. Markovic, C.A. Lucas, A. Rodes, V. Stamenkovic, P.N. Ross, Surface Science, 499 (2002) L149-L158.

[36] R.S. Ferreira Jr, V.R. Oliveira, R.G.C.S. Reis, G. Maia, G.A. Camara, Journal of Power Sources, 185 (2008) 853-856.

[37] G.F. McLean, T. Niet, S. Prince-Richard, N. Djilali, International Journal of Hydrogen Energy, 27 (2002) 507-526.

[38] K. Scott, E. Yu, G. Vlachogiannopoulos, M. Shivare, N. Duteanu, Journal of Power Sources, 175 (2008) 452-457.

[39] M.A. Scibioh, S.K. Kim, E.A. Cho, T.H. Lim, S.A. Hong, H.Y. Ha, Applied Catalysis B: Environmental, 84 (2008) 773-782.

[40] D.J. Guo, X.P. Qiu, W.T. Zhu, L.Q. Chen, Applied Catalysis B: Environmental, 89 (2009) 597-601.

[41] J. Wang, S. Yu, J. Xi, L. Chen, W. Zhu, X. Qiu, Electrochemical and Solid-State Letters, 10 (2007) B114-B118.

[42] U. Koponen, T. Peltonen, M. Bergelin, T. Mennola, M. Valkiainen, J. Kaskimies, M. Wasberg, Journal of Power Sources, 86 (2000) 261-268.

[43] M. Grden, M. Lukaszewski, G. Jerkiewicz, A. Czerwinski, Electrochimica Acta, 53 (2008) 7583-7598.

[44] H. Song, P. Xiao, X. Qiu, W. Zhu, Journal of Power Sources, 195 (2010) 1610-1614.

[45] N.M. Marković, B.N. Grgur, C.A. Lucas, P.N. Ross, The Journal of Physical Chemistry B, 103 (1999) 487-495.

[46] M. Bergelin, J.M. Feliu, M. Wasberg, Electrochimica Acta, 44 (1998) 1069-1075.

[47] J. Croy, S. Mostafa, J. Liu, Y. Sohn, H. Heinrich, B. Cuenya, Catalysis Letters, 119 (2007) 209-216.

[48] C.J. Huang, F.M. Pan, H.Y. Chen, C. Li, Journal of Applied Physics, 108 (2010) 053105-053106.

[49] H. Song, X. Qiu, D. Guo, F. Li, Journal of Power Sources, 178 (2008) 97-102.

[50] M. Gustavsson, H. Ekström, P. Hanarp, L. Eurenius, G. Lindbergh, E. Olsson, B. Kasemo, Journal of Power Sources, 163 (2007) 671-678.

[51] B.E. Hayden, D.V. Malevich, D. Pletcher, Electrochemistry Communications, 3 (2001) 390-394.

[52] B.E. Hayden, D. Pletcher, J.P. Suchsland, L.J. Williams, Physical Chemistry Chemical Physics, 11 (2009) 1564-1570.

[53] Q.Z. Jiang, X. Wu, M. Shen, Z.F. Ma, X.Y. Zhu, Catalysis Letters, 124 (2008) 434-438.

[54] T. Ying, H. Qiang, T. Cheng, C. Yue, A. Sufen, L. Junbai, Journal of Nanoscience and Nanotechnology, 6 (2006) 2072-2076.

[55] S.G. Neophytides, K. Murase, S. Zafeiratos, G. Papakonstantinou, F.E. Paloukis, N.V. Krstajic, M.M. Jaksic, The Journal of Physical Chemistry B, 110 (2006) 3030-3042.

[56] B. Huber, H. Gnaser, C. Ziegler, Surface Science, 566-568 (2004) 419-424.

[57] S. Guerin, B.E. Hayden, D. Pletcher, M.E. Rendall, J.-P. Suchsland, L.J. Williams, Journal of Combinatorial Chemistry, 8 (2006) 791-798.

[58] A. Rothschild, Y. Komem, A. Levakov, N. Ashkenasy, Y. Shapira, Applied Physics Letters, 82 (2003) 574-576.

[59] Z. Liu, X.Y. Ling, X. Su, J.Y. Lee, The Journal of Physical Chemistry B, 108 (2004) 8234-8240.

[60] B.E. Hayden, A.J. Murray, R. Parsons, D.J. Pegg, Journal of Electroanalytical Chemistry, 409 (1996) 51-63.

[61] J. Chen, B. Lim, E.P. Lee, Y. Xia, Nano Today, 4 (2009) 81-95.

[62] N.M. Markovic, P.N. Ross, Surface Science Reports, 45 (2002) 117-229.

[63] G. Ertl, M. Neumann, K.M. Streit, Surface Science, 64 (1977) 393-410.

[64] K.J.J. Mayrhofer, B.B. Blizanac, M. Arenz, V.R. Stamenkovic, P.N. Ross, N.M. Markovic, The Journal of Physical Chemistry B, 109 (2005) 14433.

[65] M. Watanabe, S. Motoo, Journal of Electroanalytical Chemistry, 60 (1975) 275.

[66] H.A. Gasteiger, N. Markovic, J.P.N. Ross, E.J. Cairns, Journal of The Electrochemical Society, 141 (1994) 1795-1803.

[67] G. Tremiliosi-Filho, H. Kim, W. Chrzanowski, A. Wieckowski, B. Grzybowska, P.

Kulesza, Journal of Electroanalytical Chemistry, 467 (1999) 143-156.

[68] J.C. Davies, B.E. Hayden, D.J. Pegg, Surface Science, 467 (2000) 118-130.

[69] J.B. Goodenough, A. Hamnett, B.J. Kennedy, R. Manoharan, S.A. Weeks, Journal of Electroanalytical Chemistry, 240 (1988) 133-145.

[70] M. Krausa, W. Vielstich, Journal of Electroanalytical Chemistry, 379 (1994) 307-314.

[71] T. Frelink, W. Visscher, J.A.R. van Veen, Langmuir, 12 (1996) 3702-3708.

[72] M. Lazzeri, A. Vittadini, A. Selloni, Physical Review B, 63 (2001) 155409.

[73] A. Vittadini, A. Selloni, F.P. Rotzinger, Gr, auml, M. tzel, Physical Review Letters, 81 (1998) 2954.

[74] C. Arrouvel, M. Digne, M. Breysse, H. Toulhoat, P. Raybaud, Journal of Catalysis, 222 (2004) 152-166.

[75] S.J. Tauster, S.C. Fung, R.L. Garten, Journal of the American Chemical Society, 100 (1978) 170-175.

[76] H. Song, X. Qiu, F. Li, Electrochimica Acta, 53 (2008) 3708-3713.

[77] M. Hepel, I. Dela, T. Hepel, J. Luo, C.J. Zhong, Electrochimica Acta, 52 (2007) 5529-5547.

[78] T.C. Wen, C.C. Hu, Journal of The Electrochemical Society, 140 (1993) 988-995.

[79] A.E. Bolzán, Journal of Electroanalytical Chemistry, 437 (1997) 199-208.

[80] M. Wang, D.j. Guo, H.l. Li, Journal of Solid State Chemistry, 178 (2005) 1996-2000.

[81] P.K. Shen, C. Xu, Electrochemistry Communications, 8 (2006) 184-188.

[82] C.W. Xu, H. Wang, P.K. Shen, S.P. Jiang, Advanced Materials, 19 (2007) 4256-4259.

[83] Y. Zhu, Y. Kang, Z. Zou, Q. Zhou, J. Zheng, B. Xia, H. Yang, Electrochemistry Communications, 10 (2008) 802-805.

[84] F. Jia, K.w. Wong, R. Du, Electrochemistry Communications, 11 (2009) 519-521.

[85] R.K. Pandey, V. Lakshminarayanan, The Journal of Physical Chemistry C, 113 (2009) 21596-21603.

[86] Z. Yin, H. Zheng, D. Ma, X. Bao, The Journal of Physical Chemistry C, 113 (2008) 1001-1005.

[87] C. Bianchini, P.K. Shen, Chemical Reviews, 109 (2009) 4183-4206.

[88] X. Wang, W. Wang, Z. Qi, C. Zhao, H. Ji, Z. Zhang, Journal of Power Sources, 195 (2010) 6740-6747.

[89] F. Miao, B. Tao, L. Sun, T. Liu, J. You, L. Wang, P.K. Chu, Journal of Power Sources, 195 (2010) 146-150.

[90] D.A.J. Rand, R. Woods, Journal of Electroanalytical Chemistry and Interfacial Electrochemistry, 35 (1972) 209-218.

[91] S.H. Cadle, Journal of The Electrochemical Society, 121 (1974) 645-648.

[92] L.H. Dall'Antonia, G. Tremiliosi-Filho, G. Jerkiewicz, Journal of Electroanalytical Chemistry, 502 (2001) 72-81.

[93] K. Juodkazis, J. Juodkazytė, B. Šebeka, G. Stalnionis, A. Lukinskas, Russian Journal of Electrochemistry, 39 (2003) 954-959.

[94] Y. Du, K. Lv, B. Su, N. Zhang, C. Wang, Journal of Applied Electrochemistry, 39 (2009) 2409-2414.

[95] O. Yepez, P.G. Pickup, Electrochemical and Solid-State Letters, 8 (2005) E35-E38.

[96] L.S. Kibis, A.I. Titkov, A.I. Stadnichenko, S.V. Koscheev, A.I. Boronin, Applied Surface Science, 255 (2009) 9248-9254.

[97] T. Pillo, et al., Journal of Physics: Condensed Matter, 9 (1997) 3987.

[98] K.S. Kim, A.F. Gossmann, N. Winograd, Analytical Chemistry, 46 (1974) 197-200.

[99] Y.N. Wu, S.J. Liao, Y.L. Su, J.H. Zeng, D. Dang, Journal of Power Sources, 195 (2010) 6459-6462.

[100] C. Gabrielli, P.P. Grand, A. Lasia, H. Perrot, Journal of The Electrochemical Society, 151 (2004) A1937-A1942.

[101] A. Czerwinski, R. Marassi, S. Zamponi, Journal of Electroanalytical Chemistry and Interfacial Electrochemistry, 316 (1991) 211-221.

[102] M.S. Rau, P.M. Quaino, M.R. Gennero de Chialvo, A.C. Chialvo, Electrochemistry Communications, 10 (2008) 208-212.

[103] A.J. Zhang, M. Gaur, V.I. Birss, Journal of Electroanalytical Chemistry, 389 (1995) 149-159.

[104] Y.N. Wu, S.J. Liao, Z.X. Liang, L.J. Yang, R.F. Wang, Journal of Power Sources, 194 (2009) 805-810.

[105] Z. Liu, L. Hong, M.P. Tham, T.H. Lim, H. Jiang, Journal of Power Sources, 161 (2006) 831-835.

[106] Y. Wang, T.S. Nguyen, X. Liu, X. Wang, Journal of Power Sources, 195 (2010) 2619-2622.

[107] R. Manoharan, J.B. Goodenough, ChemInform, 23 (1992).

[108] Q. He, W. Chen, S. Mukerjee, S. Chen, F. Laufek, Journal of Power Sources, 187 (2009) 298-304.

[109] M. Sevilla, C. Sanchís, T. Valdés-Solís, E. Morallón, A.B. Fuertes, Electrochimica Acta, 54 (2009) 2234-2238.

[110] A. Czerwinski, Journal of Electroanalytical Chemistry, 379 (1994) 487-493.

[111] L. Pedocchi, M.R. Ji, S. Lizzit, G. Comelli, G. Rovida, Journal of Electron Spectroscopy and Related Phenomena, 76 (1995) 383-387.

[112] K. Zorn, S. Giorgio, E. Halwax, C.R. Henry, H. Grönbeck, G.n. Rupprechter, The Journal of Physical Chemistry C, 115 (2010) 1103-1111.

[113] R. Mancharan, J.B. Goodenough, Journal of Materials Chemistry, 2 (1992) 875-887.

[114] Z.Q. Li, C.J. Lu, Z.P. Xia, Y. Zhou, Z. Luo, Carbon, 45 (2007) 1686-1695.

[115] A. Pozio, M. De Francesco, A. Cemmi, F. Cardellini, L. Giorgi, Journal of Power

Sources, 105 (2002) 13-19.

[116] S. Garbarino, A. Pereira, C. Hamel, E. Irissou, M. Chaker, D. Guay, The Journal of Physical Chemistry C, 114 (2010) 2980-2988.

[117] A. Howard, D.N.S. Clark, C.E.J. Mitchell, R.G. Egdell, V.R. Dhanak, Surface Science, 518 (2002) 210-224.

[118] P. Marcus, C. Hinnen, Surface Science, 392 (1997) 134-142.

[119] J.L. Rousset, A.J. Renouprez, A.M. Cadrot, Physical Review B, 58 (1998) 2150.

[120] B.C. Khanra, J.C. Bertolini, J.L. Rousset, Journal of Molecular Catalysis A: Chemica,l 129 (1998) 233-240.

[121] A. Kowal, S.N. Port, R.J. Nichols, Catalysis Today, 38 (1997) 483-492.

[122] M.A. Abdel Rahim, R.M. Abdel Hameed, M.W. Khalil, Journal of Power Sources, 134 (2004) 160-169.

[123] E. Herrero, K. Franaszczuk, A. Wieckowski, The Journal of Physical Chemistry, 98 (1994) 5074-5083.

[124] Z. Liu, X.Y. Ling, X. Su, J.Y. Lee, L.M. Gan, Journal of Power Sources, 149 (2005) 1-7.

[125] U. Koponen, T. Peltonen, M. Bergelin, T. Mennola, M. Valkiainen, J. Kaskimies, M. Wasberg, Journal of Power Sources, 86 (2000) 261-268.

[126] J.N. Tiwari, F.M. Pan, T.M. Chen, R.N. Tiwari, K.L. Lin, Journal of Power Sources, 195 (2010) 729-735.

[127] F. Cinquini, L. Giordano, G. Pacchioni, Theoretical Chemistry Accounts: Theory, Computation, and Modeling (Theoretica Chimica Acta), 120 (2008) 575-582.

[128] J.S. Spendelow, J.D. Goodpaster, P.J.A. Kenis, A. Wieckowski, The Journal of Physical Chemistry B, 110 (2006) 9545-9555.

[129] A.V. Tripković, K.D. Popović, J.D. Momčilović, D.M. Dražić, Journal of Electroanalytical Chemistry, 418 (1996) 9-20.

[130] M. Vuković, Journal of Applied Electrochemistry, 24 (1994) 878-882.

[131] H. Li, H. Li, W.-L. Dai, W. Wang, Z. Fang, J.-F. Deng, Applied Surface Science, 152 (1999) 25-34.

[132] G.B. Hoflund, W.S. Epling, Chemistry of Materials, 10 (1998) 50-58.

[133] N.S. McIntyre, M.G. Cook, Analytical Chemistry, 47 (1975) 2208-2213.

[134] A.P. Grosvenor, M.C. Biesinger, R.S.C. Smart, N.S. McIntyre, Surface Science, 600 (2006) 1771-1779.

[135] A. Verma, S. Basu, Journal of Power Sources, 174 (2007) 180-185.

[136] B.S. Huang, F.Y. Chang, M.Y. Wey, International Journal of Hydrogen Energy, 35 (2010) 7699-7705.

[137] H. Meng, C. Wang, P.K. Shen, G. Wu, Energy & Environmental Science, 4 (2011) 1522-1526.

Vita

基本資料

姓名：陳重守 (Chung-Shou Chen)
出生年月日：民國 70 年 8 月 21 日
地址：台北市中山區建國北路三段 78 號八樓
電子信箱：hockeyplayer0821@hotmail.com

學歷

國立交通大學　材料科學與工程研究所博士班（2006.9 – 2011.7）
國立台北科技大學　化學工程研究所碩士班（2004.9 – 2006.7）
私立中國文化大學　化學工程學系（2000.9 – 2004.7）

經歷

國立交通大學　貴重儀器中心　歐傑微探能譜儀助教（2007.9 – 2010.9）
國立交通大學　材料科學與工程學系　材料力學助教（2010.9 – 2011.1）
國立台北科技大學　化學工程學系　輸送現象與單元操作助教（2004.2 – 2005.6）

List of Publications

Journal Paper

[1] **Chung-Shou Chen**, Fu-Ming Pan, "Electrocatalytic activity of Pt nanoparticles deposited on porous TiO$_2$ supports toward methanol oxidation", Applied Catalysis B: Environmental, 91 (2009) 663-669.

[2] **Chung-Shou Chen**, Fu-Ming Pan, Hsin-Jung Yu, "Electrocatalytic activity of Ni stalactite supported Pt nanoparticles toward methanol oxidation in alkaline medium", Applied Catalysis B: Environmental, 104 (2011) 988-995.

[3] **Chung-Shou Chen**, Fu-Ming Pan, Tzu-Chung Wang, "Electrocatalytic Oxidation of Methanol in Acidic Solutions on PdO Nanoflake Thin Films loaded with Pt Nanoparticles", Applied Catalysis B: Environmental, under review.

Conference Paper

[1] **Chung-Shou Chen**, Fu-Ming Pan, "Electrocatalytic activity of Pt Nanoparticles deposited on Porous TiO$_2$ Supports toward methanol oxidation", 215th Meeting of the Electrochemical Society, San Francisco, USA, May (2008). [Oral]

[2] **Chung-Shou Chen**, Fu-Ming Pan and Hisn-Jung Yu, "Electrocatalytic activity of Pt nanoparticles on karst-rock shaped Ni thin films toward methanol and ethanol oxidation in alkaline solutions", 218th Meeting of the Electrochemical Society, Las Vegas, USA, Oct (2010). [Oral]

[3] "鉑奈米金屬披覆孔洞性二氧化鈦應用於甲醇氧化之研究", **陳重守**, 許善存, 潘扶民, 中華民國材料年會 (2008)。

[4] "以鎳鐘乳石結構作為鉑奈米顆粒之擔體—直接甲醇燃料電池電催化研究", **陳重守**, 余欣蓉, 潘扶民, 中華民國材料年會 (2009)。

[5] "氧化鈀奈米薄片擔體對鉑奈米顆粒之甲醇氧化反應電催化效能之影響", **陳重守**, 潘扶民, 戴均晏, 黃建融, 王子中, 中華民國材料年會 (2010)。

Thesis

以結晶技術系統化篩選藥物的多晶型研究, Systematic screening of drug substances for polymorphs using crystallization techniques, 國立台北科技大學化學工程研究所 (2005)。